

Loading Rate Effects on the Hydrogen Enhanced Cracking Behavior of Ni- and Co-based
Superalloys for Marine Applications

A Thesis

Presented to
the faculty of the School of Engineering and Applied Science
University of Virginia

in partial fulfillment
of the requirements for the degree

Master of Science

by

Allison S. Popernack

May

2017

APPROVAL SHEET

The thesis
is submitted in partial fulfillment of the requirements
for the degree of
Master of Science


AUTHOR

The thesis has been read and approved by the examining committee:

James T. Burns

Advisor

James M. Fitz-Gerald

Sean R. Agnew

Accepted for the School of Engineering and Applied Science:



Craig H. Benson, Dean, School of Engineering and Applied Science

May
2017

Abstract

Marine fastener alloys can be susceptible to hydrogen environmentally assisted cracking (HEAC) in cathodically polarized seawater environments [1]–[3]. Understanding the controlling mechanisms of HEAC is critical to developing accurate predictive models for structural management of these material systems. Prior work has demonstrated that there is a potentially strong influence of loading rate on the HEAC susceptibility in environments pertinent to engineering applications [4]. The current work uses linear elastic fracture mechanics (LEFM) based testing to characterize the stress intensity rate (dK/dt) dependence of HEAC behavior for Monel K-500 (Ni-based superalloy) and MP98t (Co-based superalloy) in cathodically polarized solutions. This work has been divided into three tasks to rigorously analyze the material behavior.

Task 1 addresses laboratory testing challenges and develops a functional protocol for characterizing the HEAC resistance of high toughness, relatively low strength materials in mildly aggressive environments using LEFM based techniques. In this paradigm, direct current potential difference (dcPD) uniquely enables high fidelity detection of crack advance but was found to be adversely influenced by specimen plasticity and non-HEAC based crack advance (e.g. crack tip blunting, ductile tearing, etc.). A mitigation protocol was developed to truncate data prior to the remaining ligament reaching the proportional limit and to decouple the effect of crack tip plasticity from real crack growth. Task 2 utilized the protocol above to quantify the effect of the stress intensity rate, dK/dt , on standard susceptibility metrics: the threshold stress intensity, K_{TH} , and the stage II crack growth rate, da/dt_{II} , for Monel K-500 and MP98t [4]. MP98t was found to be much less susceptible to HEAC than Monel K-500. For both materials, the K_{TH} did not exhibit a strong dependence on dK/dt , whereas the da/dt_{II} increased as a power law function of dK/dt .

Task 3 explored the mechanistic underpinnings that govern the effect of loading rate on the SCC behavior of each alloy. Traditional loading rate dependent arguments such as H diffusion limitation and crack tip film rupture were not found to be consistent with the data and the materials/environment/loading conditions. The dK/dt dependence was analyzed in the context of prominent H-enhanced damage mechanisms: hydrogen enhanced local plasticity (HELP) and hydrogen enhanced decohesion (HEDE) [5]. The observed increase in da/dt with increasing dK/dt is considered to be due to one or both of the following two failure criteria, provided a dK/dt

independent of H concentration at the crack tip. In the first, failure requires a critical crack tip strain to be exceeded for crack advance; and in the second, accelerated work-hardening increases the crack tip stresses which enable decohesion. In both cases, elevated dK/dt would cause elevated da/dt due to exceedance of the critical value in a shorter time increment. These arguments do not influence K_{TH} because crack growth does not occur below this value.

Table of Contents

Abstract.....	1
List of Figures	5
1. Introduction	8
1.1 Materials	9
1.1.1 Monel K-500	9
1.1.2 MP98t.....	9
1.2 EAC Characterization Methods	10
1.2.1 Background	10
1.2.2 LEFM-Based Characterization of EAC Properties of Monel K-500	13
1.3 HEAC Mechanisms	14
1.3.1 HEAC Mechanism in Monel K-500	15
1.3.2 Loading Rate Effects.....	18
1.4 Knowledge gaps, Objectives, and Tasks.....	21
2. Experimental procedure	22
2.1 Basic Material Characterization	22
2.1.1 Monel K-500.....	22
2.1.2 MP98t.....	22
2.2 Mechanical Testing	23
2.2.1 Fracture Mechanics Testing	23
2.2.1.1 Sample description.....	23
2.2.1.2 Sample Preparation.....	24
2.2.1.3 Load Application.....	24
2.2.1.4 Direct Current Potential Difference (dcPD).....	25
2.2.1.5 Fatigue precrack.....	26
2.2.1.6 Environmental Control.....	27
2.2.1.7 K Test Protocol	28
2.2.1.8 Post-test Fatigue	29
2.2.1.9 End of Test Procedure	29
2.2.1.10 Post-Test Analysis	30
2.2.1.10.1 Elastic-Plastic Analysis.....	30
2.2.1.10.2 Post-test Correction Procedures.....	31
2.2.1.11 Metrics of Interest	32

2.2.2 Electrical Resistance Measurements of Smooth Tensile Bars.....	32
3. Results and Discussion	33
3.1 Initial Data and Experimental Findings	33
3.1.1 dcPD Sensitivity.....	33
3.1.2 Initial Characterization of Growth Rate versus Stress Intensity	35
3.2 Task 1: Identify the challenges associated with dcPD testing techniques to quantify IG-SCC resistant materials using LEFM based techniques.....	40
3.2.1 Inert Environment Testing Data.....	40
3.2.2 Broad Analysis of Inert Testing Data	42
3.2.3 Identify the phenomena responsible for of the da/dt vs K curve regions.....	43
3.2.3.1 Bulk Analysis.....	43
3.2.3.1.1 Plane Strain Limit Load Analysis.....	43
3.2.3.1.2: Bulk Plasticity Analysis	44
3.2.3.1.3 da/dt vs K curve comparison to fractography	50
3.2.3.1.4 Fractography below the yield strength.....	51
3.2.3.1.5 Fractography above the yield strength.....	52
3.2.3.1.6 Comparison to environmental data	52
3.2.3.1.7 Error Mitigation Procedure.....	55
3.2.3.2 Localized Crack Tip Plasticity.....	55
3.2.4 Corrections applied to MP98t environmental data	59
3.3 Task 2: Quantify the effect of dK/dt on the standard LEFM metrics K_{TH} and da/dt_{II} for Monel K-500 at relevant electrochemical polarization	63
3.3.1 IG-SCC Susceptibility Metrics	63
3.3.2 Fractography	65
3.3.3 Analysis of MP98t	67
3.3.3.1 dK/dt trends in MP98t	67
3.3.4 Comparison between Monel K-500 and MP98t.....	70
3.4 Task 3: Explore the mechanistic underpinnings that govern the effect of loading rate on the IG-SCC behavior of each alloy.....	72
3.4.1 Loading Rate dependence of da/dt.....	73
3.4.1.1 Diffusion Limitation.....	73
3.4.1.2 Defecting of a Crack Tip Protective Film	73
3.4.1.3 Concurrent Plasticity and H Uptake	75
3.4.2 Effects on K_{TH}	77

4. Conclusions	79
References	82

List of Figures

Figure 1: Local potential vs normalized position, x , along the artificial crevice with aged Monel K-500 as a function of external applied potential and exposure time in bulk 0.6 M NaCl solution. The crevice gap (G) was 1mm. [4]	16
Figure 2: C_{H-diff} vs E_A for a given crack length in Monel K-500 submersed in 0.6M NaCl [4]	17
Figure 3: The micromechanical models for K_{TH} and da/dt_{II} associated with their respective experimental data for Monel K-500 with varying applied potential.....	18
Figure 4: K_{TH} for rising displacement experiments on compact tension (CT) and double cantilever bending (DCB) specimens of Al 2024 T351 in the S-L orientation, performed at various displacement rates. [41] 20	
Figure 5: da/dt vs. dK/dt for Ti-6Al-4V plate in 3.5% NaCl, $-0.500V_{SCE}$ and moist air for various loading rate and K_I levels. [63].....	20
Figure 6: Side view of SENT sample test section.....	24
Figure 7: Assembled environmental cell with sample for immersive testing in polarized environments. 27	
Figure 8: The size of the plastic zone in front of the crack tip is related to the force concentrating behavior. The plastic zone exists where the local stress exceeds σ_{YS} . Figure from Anderson [27]	34
Figure 9: da/dt vs K_I data from all Monel K-500 experiments in 0.6 M NaCl with $E_A = -0.950 V_{SCE}$. Only the historic correction for crack tip shorting has been made to this data set.....	36
Figure 10: Fracture surfaces of Monel K-500 in 0.6 M NaCl with $E_A = -0.950 V_{SCE}$, corresponding to the data in Figure 9. The crack propagates form left to right in all micrographs except $dK/dt = 4.0 MPa\sqrt{m}/hr$ in which the crack propagated from bottom to top. The lines indicate transition points on the fracture surface: continuous white = end of precrack, dashed white = start of post-test fatigue, black = start of final failure.	37
Figure 11: The three main fracture mechanisms displayed in this work: (a) transgranular (TG) fatigue, (b) intergranular stress corrosion cracking (IG-SCC), (c) microvoid coalescence, ductile failure.	38
Figure 12: The percent difference in crack length between the apparent dcPD value and the end of IGC behavior compared to the apparent interrupted K_I for all tests in 0.6M NaCl, $E_A = -0.950 V_{SCE}$	39
Figure 13: The apparent da/dt vs K_I of Monel K-500 at fixed dK/dt in dry N_2 . I, II, and III correspond to regions of near constant slope, indicating different controlling behaviors on the dcPD signal.....	41

Figure 14: Fracture surfaces of Monel K-500 in Dry N₂, corresponding to the data in Figure 13. The crack propagates from left to right in all micrographs except dK/dt = 4.0 MPa√m/hr in which the crack propagated from bottom to top. The lines indicate transition points on the fracture surface: continuous white = end of precrack, dashed white = start of post-test fatigue, black = start of final failure. If two lines occupy the same space, the later occurring event is shown..... 42

Figure 15: Comparison of the limit load, P_o, and the applied load with apparent crack length of dK/dt = 4.0 MPa√m/hr in dry N₂. 44

Figure 16: Compression stress-strain curve for Monel K-500. 45

Figure 17: A curve showing the derivative of the slope between incremented points on the compressive stress-strain curve. Deviation from zero was used to define the proportional limit. 45

Figure 18: The change in measured dcPD voltage and actuator displacement with applied load of a Monel K-500 smooth dog bone tensile test. The proportional limit (a) and the yield stress (b) are labeled. 46

Figure 19: Experimentally recorded ΔV compared to the ΔV calculated based on elastic dimension change with stress for the Monel K-500 dog bone tensile bar..... 47

Figure 20: The K_J of the proportional limit (PL) and yield strength (YS) are labeled for each dK/dt, Monel K-500 dry N₂ test. 50

Figure 21: The fracture surface of Monel K-500 dK/dt = 3.0 MPa√m/hr focusing on the region that occurred during the test. 51

Figure 22: Apparent crack growth data for dK/dt = 1.0 MPa√m/hr in 0.6M NaCl EA = -0.950V_{SCE} and dry N₂..... 53

Figure 23: The full fracture surface for Monel K-500 in 0.6M NaCl, -0.950V_{SCE}, dK/dt = 3.0 MPa√m/hr. Crack growth occurred from left to right. (a) is TG fatigue, (b) is IG-SCC, (c) is the stretch zone, (d) is TG post-test fatigue, and (e) is ductile failure..... 55

Figure 24: The data for Monel K-500 at fixed dK/dt tested in dry N₂, cropped at the proportional limit, each with the exponential fit at a fixed z value. 56

Figure 25: The resolution limit coefficient fit value (C) for each dK/dt in dry N₂. The data has a linear fit. 57

Figure 26: Graphically displaying the effect of removing the resolution limit from the environmental crack growth data for Monel K-500 at dK/dt = 0.15 MPa√m/hr, -0.950V_{SCE} 58

Figure 27: Full environmental data set for Monel K-500 with corrections for shorting, truncation at the proportional limit, and with localized crack tip plasticity removed. 59

Figure 28: Dry N2 curve for MP98t, $dK/dt = 1.0 \text{ MPavm/hr}$, dry N2. The equation for the resolution limit (RL) is shown in the legend. 60

Figure 29: The Mode I environmental fracture surfaces of MP98t. The crack propagated from bottom to top..... 61

Figure 30: Crack growth rate vs K data for MP98t with corrections made for shorting, localized crack tip plasticity, crack deflection, and truncation at the proportional limit..... 62

Figure 31: Corrected data set for $dK/dt = 0.15 \text{ MPavm/hr}$ with the illustrated locations of da/dt_{II} and K_{TH} 63

Figure 32: The K_{TH} compared to dK/dt for Monel K-500 at 0.6M NaCl with $-0.950V_{SCE}$ 64

Figure 33: da/dt_{end} compared to dK/dt for Monel K-500 at 0.6M NaCl with $-0.950V_{SCE}$ 64

Figure 34: IG-SCC fracture surfaces of Monel K-500 in 0.6 M NaCl with $E_A = -0.950 V_{SCE}$, at 1000x..... 66

Figure 35: K_{TH} for MP98t for a range of dK/dt tested at $-1.3 V_{SCE}$, 0.6M NaCl 68

Figure 36: da/dt_{end} for MP98t for a range of dK/dt tested at $-1.3 V_{SCE}$, 0.6M NaCl 68

Figure 37: 1000x images of the Mode 1 environmental fracture of MP98t..... 69

Figure 38: K_{TH} for the environmental data sets of Monel K-500 and MP98t..... 70

Figure 39: da/dt_{end} for the environmental data sets of Monel K-500 and MP98t..... 71

Figure 40: Representative Pourbaix diagram for Monel K-500 based on its two main components, Ni and Cu. OLI generated 75

1. Introduction

Electrochemical degradation is a primary failure mode for many structural metal materials that operate in marine environments, as such corrosion resistant materials and corrosion preventive methods are critical for the longevity and safety of such engineering components. Co- and Ni-based superalloys are used in submerged marine applications such as fasteners on ocean vessels and North Sea offshore platforms due to their moderate strength, high toughness, and corrosion resistance in submerged aqueous chloride environments [1]. However, these alloys are typically coupled with low alloy steels that are highly susceptible to degradation in these environments and thus require the use of cathodic protection (CP) systems; specifically, sacrificial anodes (typically Zn or Al-based) galvanically coupled with the steel. The anode preferentially corrodes and protects the steel by creating a cathodically polarized local environment [2], [6]. Typically the surrounding environment maintains a potential of $\approx -1.05 V_{SCE}$, which effectively prevents corrosion of the steel in chloride environments [2]. The anodes extend the life of the steel but have been shown to adversely affect Ni-superalloy fasteners, causing unexpected failures during use [1]. Critically, the local cathodic environment will generate atomic hydrogen (H) in sufficient quantities to enable embrittlement of the superalloy. This uptake of H coupled with in-service loading can lead to intergranular (IG) failures [1]. Such in-service failures justify the need for mechanistic understanding, screening protocols, and predictive models of this environmentally assisted cracking (EAC) degradation mode.

Accelerated testing methods are used to characterize fastener material susceptibility and improve material selection for structural management. These techniques scale from smooth bar testing to pre-cracked fracture mechanics tests using quasi-static or dynamic loading. This wide range of testing methods produces a correspondingly diverse range of metrics to quantify the EAC behavior. Critically, the loading rate has been observed to strongly influence the EAC susceptibility regardless of the testing method or metrics used to quantify the behavior [5-10]. Fracture mechanics testing is preferred as it most rigorously ensures similitude between the testing technique and the relevant in-service part geometry and working conditions. As such, the overarching aim of this work will be to investigate the effects of loading rate on the EAC behavior that is quantified via high fidelity fracture mechanics based testing. This effort will be conducted

on two alloys that are commonly used in marine fastener applications (Monel K-500 and MP98t) submerged in a cathodically polarized aqueous chloride environment.

1.1 Materials

1.1.1 Monel K-500

Procurement of Monel K-500, also designated as UNS N05500, is governed by the US Federal Specification QQ-N-286; of note, but there is no standardized heat treatment procedure [7]. Monel K-500 is an austenitic Ni-Cu solid solution that is precipitation-hardened by homogeneously distributed γ' ($\text{Ni}_3(\text{Al}, \text{Ti})$) intermetallic particles [8]. The γ' phase has an ordered L_{12} crystal structure with a very low misfit strain (<0.1% misfit strain) to the surrounding matrix. Given this low misfit, γ' forms as spherical particles and maintains this morphology even after prolonged aging [9]. Carbide inclusions are also found in this material, but do not contribute significantly to strengthening [9]. Monel K-500 demonstrates a K_{IC} ranging from 198 to 340 MPa $\sqrt{\text{m}}$ due to lot-to-lot variation [4].

Monel K-500 has been commonly used in offshore platform fasteners [1]–[3], [10]–[12] and submarine components [13], [14], but has experienced in-service failures attributed to a H-based EAC failure mode. This is consistent with the known susceptibility of Ni to IG cracking when exposed to cathodically polarized acidic and gaseous low pressure H_2 environments [15], [16]. Specimens of Ni and Ni-Cu superalloys pre-charged with H showed IG cracking due to internal H assisted cracking (IHAC) [17]–[21]. This susceptibility is acutely pertinent to marine applications where cathodic polarization can induce H charging in Monel K-500. The basic metallurgy of Monel K-500 underwent heat treatment renovations to reduce its susceptibility to hydrogen embrittlement by annealing out the hardening effects of machining [1], but its susceptibility still remains an issue [2], [3], [10]–[14].

1.1.2 MP98t

After in-service failures of Monel K-500, MP98t was specifically designed as a replacement. MP98t is derived from MP159, a MULTIPHASE (MP) alloy developed by Dupont and used as an aerospace fastener [22]. The base metallurgy is a γ' precipitation hardened solid solution Co-Ni-Cr alloy with excellent corrosion resistance in chloride electrolytes and resistance

to stress corrosion cracking [22]. Despite its favorable electrochemical qualities, MP159 has a yield strength of 1800 MPa paired with a comparably insufficient fracture toughness for marine fastener application [22]. MP159 properties were altered by adjusting aging time and amount of cold work. Several combinations of additional processing were determined to lower the yield strength to 1035 MPa and increase the fracture toughness to make it suitable for fastener application [22]. The exact procedure is not disclosed and the final product is designated as MP98t. Due to being cold worked in production, MP98t has an elongated grain structure producing anisotropic mechanical properties. After the initial property criteria were met, MP98t was evaluated for application as a fastener.

MP98t underwent the Fracture Toughness Review Process (FTRP) and the fastener structural elements test (FSET) to prove its viability as a fastener material [22][23]. The FSET used a minimum flaw size on a threaded shape, similar to bolt threads, and then a rapid impact load [23]. MP98t yielded and exhibited ductile failure, a high energy fracture process as opposed to low energy brittle failure [22]. The K_{IC} of that MP98t lot was found to be 280 MPa \sqrt{m} [23]. The physical properties of MP98t showed promise for its intended application; however, very little EAC evaluation has been published for MP98t. Due to the similarities of their general make ups, solid solution with strengthening precipitates, the trends that have been shown for Monel K-500 are expected to hold for MP98t.

1.2 EAC Characterization Methods

1.2.1 Background

Historically, the material selection process and management of EAC for alloys in strained marine environments is often dictated by a “go/no-go” approach based on the results of accelerated testing. Specifically, if testing indicates that the service environment and loading conditions are below a threshold level of severity, then it is assumed that cracking will not occur over the lifetime of the component. This highlights the critical importance of ensuring that the testing techniques conservatively and rigorously capture the pertinent failure mechanisms in a time-frame that is conducive to laboratory testing. Non-fracture mechanics testing has progressed from rudimentary empirically-based legacy approaches (e.g. ASTM G39 [24], G30

[25]) to a more controlled slow strain rate tensile testing (ASTM G129 [26]), where changes in the time to failure, ductility, and strength are monitored as a function of environment.

During ASTM G129 slow strain rate testing (SSRT), a constant strain rate is applied to a tensile-loaded sample [26]. This method traditionally utilizes smooth or notched tensile sample geometries to quantify environmental susceptibility. The sample geometry determines the derivable metrics. Smooth cylindrical tensile specimens use change in ductility and time to failure as metrics while notched samples use notch tensile strength to quantify changes due to the applied environment. The notched specimens exhibit a relatively blunt machined notch; sharp cracks are rarely associated with this method, but are briefly mentioned in the ASTM standard. ASTM G129 states that its protocols are not intended to represent the service performance of a material due to its accelerated timetable, only to act as a screening process to expose detrimental behavior [26]. It has been reported that materials which experience failure in the laboratory setting did not fail during service life and, notably for the smooth specimens, in-service failures were not always replicated experimentally [26]. Marine fasteners do not fail via net-section yielding like smooth SSRTs, rather typically by cracks initiating at some susceptible point on a thread [1]. The smooth sample geometry does not consider the stress intensity of the fastener threads, creating an inaccurate estimate of susceptibility. The metrics associated with the smooth and notched sample geometries do not lend themselves to quantitative fracture analysis, but can still be useful for identifying general mechanisms. As documented in the ASTM standard, there is no method to measure crack initiation or growth in SSRTs, limiting the information from this failure analysis [26]. In toto, while such simple tests enable an efficient and inexpensive means to screen materials, quantitatively relating the data to in-service susceptibility is not fully rigorous.

The fracture mechanics concept of similitude establishes that, independent of the component geometry, for a constant crack tip driving force and environmental condition that the material response will be constant [27]. The fracture driving force around the crack tip is characterized by geometry-independent stress intensity (K) and generates a volume of plastic deformation at the crack tip due to stress concentration, termed the plastic zone. The basic

function for K is shown in Equation 1, where K_I is the Mode I stress intensity, σ is the applied far-field stress, Y is a geometry factor that is a function of crack length (a) and the sample width (W).

$$K_I = \sigma \sqrt{\pi a} Y \left(\frac{a}{W} \right) \quad \text{Equation 1}$$

As such, controlled laboratory specimens can be used to generate data that will be directly applicable to in-service components, so long as the geometry specific stress intensity solution is known. Standardized protocols have been established to determine the relevant fracture mechanics metrics using multiple samples (ASTM E1681 [28]) and a single sample (ASTM F1624 [29]). While these tests primarily focus on establishing the minimum threshold K necessary for cracking in a given environment, a sub-critical crack growth rate (da/dt) can also be obtained. The ASTM F1624 testing is commonly referred to as the “Rising Step Loading Technique (RSL)” and is popular due to its testing efficiency. The protocol consists of subjecting a precracked specimen to a constant load hold and monitoring for load drops that would indicate the occurrence of crack advance. If no crack advance is observed after a given amount of time, then the load is rapidly increased to a higher loading level. Such incremented steps in loading are repeated until cracking is observed at which point the threshold stress intensity, K_{TH} , can be calculated. This protocol is performed at various overall loading rates to ensure that the loading is sufficiently slow to prevent diffusion limitation.

While such fracture mechanics approaches represent a critical advance in quantitative characterization of the EAC susceptibility, important limitations remain with regards to rigorously quantifying crack growth kinetics, capturing the effects of dynamic loading, and the fidelity of the crack monitoring techniques. Modern fracture mechanics testing approaches address these shortcomings to enable a more conservative and rigorous characterization of the EAC behavior by quantifying the crack growth rate, da/dt , and stress intensity, K , relationship of a wide range of stress intensity values. Such efforts were pioneered by Dietzel and Clark-Landes and initial attempts to codify such testing are reported in ISO/DIS7539-9 and in an augmented version of ASTM G129 [26], [30]. Recent efforts extend these approaches by using high fidelity direct current potential difference (dcPD) techniques to monitor the crack extension in real-time and feed these data into a software controlled loading system [4]. This set-up enables quantification of the crack growth kinetics at high fidelity and application of a wide range of fracture mechanics

informed loading conditions (e.g. different loading rates, holds, etc.). This set-up has been successfully applied to characterize the environmental cracking susceptibility of steel [31]; Al- [32]–[34]; Ti- [35], [36]; and Ni-based [4], [37], [38] alloys for a wide range of mechanical and environmental conditions. Such data is critical to inform LEFM-based component life management tools (e.g. SCCrack [39]) that enable probabilistic management of the environmental cracking behavior of engineering components for a given material, starting crack size, environment, and applied load [39]. Furthermore, these techniques enable targeted testing and mechanistic insights that can lead to material development, informed material selection, and more rigorous structural integrity management. While these state of the art testing techniques offer unprecedented opportunities to characterize EAC susceptibility, challenges remain, particularly for high toughness-moderate strength materials (e.g. Monel K-500) in mildly aggressive environments. Specifically, decoupling the crack tip/bulk plasticity from true IG crack growth, the onset of ductile crack advance below the fracture toughness [4], and plastic contributions to the crack tip driving force. Such issues will be considered in detail in this work.

1.2.2 LEFM-Based Characterization of EAC Properties of Monel K-500

Using the aforementioned dcPD techniques, fracture mechanics testing with constant-rising loading rates (and in some cases constant dK/dt) were applied to Monel K-500 to quantitatively establish the effect of electrochemical polarization [4] and varying metallurgy [38] on the EAC susceptibility and H-metal interactions [40]. Specifically, da/dt vs. K relationships were generated from which the traditional EAC metrics of threshold stress intensity, K_{TH} , and stage II crack growth rate, da/dt_{II} , were established. Such data was then used as inputs for probabilistic LEFM based modeling of crack progression for an idealized component [39]. Critically; for identical environmental conditions ($-0.800 V_{SCE}$ and 0.6 M NaCl) and on the same lot of material, testing performed using the RSL technique indicated immunity from IG-EAC, whereas the slow rising loading, $dK/dt = 0.33 \text{ MPa}\sqrt{\text{m/hr}}$, showed the material to be susceptible [4]. This behavior suggests a strong role of loading rate on the EAC susceptibility of the Monel K-500. Specifically, the RSL technique has a dK/dt of zero during the load hold, as such these experiments suggest that increasing the dK/dt increased the EAC susceptibility. [4] Similar results showing the non-conservative nature of the RSL testing technique were reported for Al-alloys

[41]. This behavior is significant from an engineering perspective in that it is necessary to ensure that the loading rate used to characterize the EAC susceptibility is pertinent (or at least conservative) for the loading conditions that the engineering component will encounter. However, this finding is also interesting from a mechanistic perspective as it suggests that active crack tip plasticity synergistically interacts with the crack tip environmental process to enhance EAC susceptibility.

Prior efforts have convincingly argued for an H-embrittlement based mechanism that is controlling the EAC behavior in Monel K-500 under cathodic polarization in aqueous chloride environments. The subsequent section will outline the H-environment assisted cracking (HEAC) findings relevant to Monel K-500 to provide the basis for the evaluation and understanding of the observed loading rate effect.

1.3 HEAC Mechanisms

The mechanisms of hydrogen embrittlement are still controversial. The most popular explanations are hydriding, Adsorption Induced Dislocation Emission (AIDE), Hydrogen Enhanced Localized Plasticity (HELP), and Hydrogen Enhanced Decohesion (HEDE). Only EAC is considered in this work, H generation at the crack tip surface is dominant. Some materials are prone to the formation of a hydride ahead of the crack tip in the presence of a sufficiently high H concentration [42]; the hydride cleaves for the crack to propagate. AIDE is explained as enhanced dislocation emission from the surface due to adsorption of H at the crack tip. AIDE argues that the adsorption of H at the surface facilitates the enhanced creation of dislocations that allow for increased plastic deformation [43]–[45]. In the HELP model, H is hypothesized to decrease the dislocation-dislocation interaction energy, thus enabling enhanced dislocation motion leading to increased localized plasticity. Elevated dislocation densities occur in H-rich areas causing increased material strength within the grains near the crack tip and creating slip steps on the grain surfaces that behave as minute force concentrators [46]–[50]. Through HEDE, the cohesive forces within the matrix or along the grain boundaries are reduced by the local H concentration, which facilitates decohesion. Models propose that HEDE requires a critical concentration of H in the fracture process zone, sufficient to degrade the Griffith toughness, k_{IG} , of grain boundary cohesion, and a

local tensile stress to drive crack propagation [51]–[54]. Predictive micromechanical models have been developed based on decohesion theory [55]–[57]. A combined HELP-HEDE mechanism has recently gain support; specifically arguing that H induced reduction in fracture toughness is due to the local hardening associated with HELP, that enables higher local stresses that enables decohesion (HEDE) through an H degraded structure (e.g. matrix or grain boundary) [58]. The total effect of each mechanism is a remarkable reduction in fracture toughness.

Prior work has evaluated the IG-EAC susceptibility of Monel K-500 using fracture mechanics approaches. It is useful review these results in the context of the above mechanisms to provide a baseline mechanistic framework in which the current study of loading rate effects can be interpreted.

1.3.1 HEAC Mechanism in Monel K-500

The EAC behavior of Monel K-500 was previously characterized via fracture mechanics testing of single edge notch tension (SENT) specimens loaded in 0.6 M NaCl at various applied electrochemical potentials [4]. These data demonstrated that the EAC susceptibility vastly increased with decreasing potential. While literature suggests a strong role of H for Ni-based alloys in chloride environments and under cathodic polarization, recent work explicitly linked the variation in the EAC behavior with changes in the expected crack tip diffusible H content, C_{H-diff} [4]. This was done by recognizing that HEAC is made possible by the generation of H at the crack tip. The amount of H produced at a metal surface will be governed by the crack tip overpotential for H production which can be calculated from the local crack tip pH and potential [4].

The subsurface diffusible H concentration at the crack tip as a function of applied potential, E_A , and crack depth parameter, x^2/G , used to capture the geometric dependence for equal-local potential within a crack. The concentration was calculated for Monel K-500 using experimentally determined relationships between E_A ; local H overpotential, η_H ; C_{H-diff} , and x^2/G . All variables were found in relation to E_A . The crack tip electrochemical behavior of Monel K-500 was simulated using an artificial crevice set-up. The profile of the potential drop, E , across the surface of the crack with time at a constant E_A is shown in Figure 1. A more positive potential than the bulk applied E_A occurs at the crack opening and continues to increase with crack depth.

The local potential of the crack decreases with time, nearing the applied potential with little change after 1 hour, 3600s.

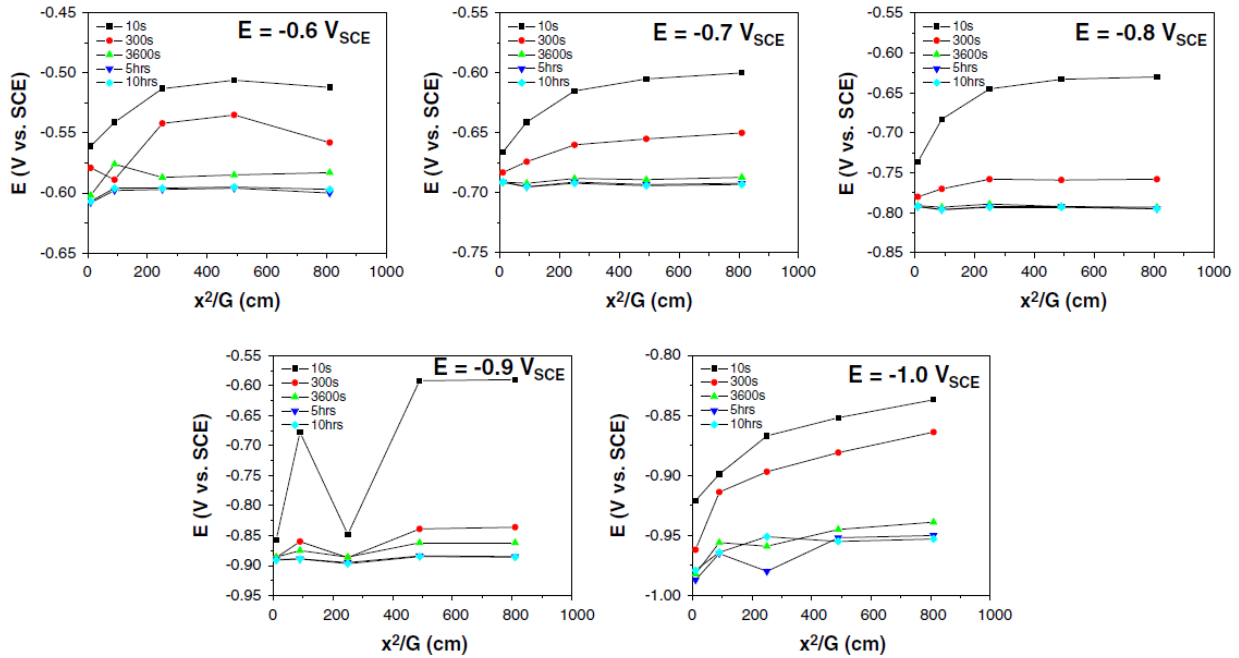


Figure 1: Local potential vs normalized position, x , along the artificial crevice with aged Monel K-500 as a function of external applied potential and exposure time in bulk 0.6 M NaCl solution. The crevice gap (G) was 1mm. [4]

The dependence of η_H on E_A was calculated using local pH and the localized potential from Figure 1. Negative η_H supports net H production, creating an abundance of available H for adsorption. Potentials below $-0.90V_{SCE}$ maintained negative η_H . The relationship of E_A with η_H and C_{H-diff} was determined by thermal desorption spectroscopy (TDS) and barnacle cell analysis on bulk samples. C_{H-diff} was shown to increase with decreasing potential. By these relationships, C_{H-diff} as a function of E_A and x^2/G was found and is displayed in Figure 2. The dashed line is the C_{H-diff} vs E_A for $10 \text{ cm} < x^2/G < 60 \text{ cm}$, equivalent to a K range of 20 to 80 MPa $\sqrt{\text{m}}$ for the standard SENT crack lengths and loading used in this work [4].

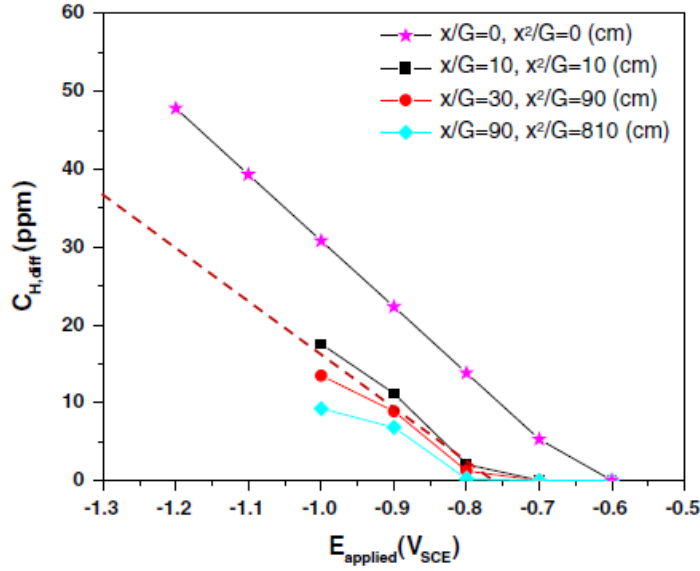


Figure 2: $C_{H,diff}$ vs E_A for a given crack length in Monel K-500 submersed in 0.6M NaCl [4]

$C_{H,diff}$ is required to determine the crack tip stress-enhanced diffusible H concentration, $C_{H\sigma}$, for H decohesion based models of the susceptibility metrics K_{TH} and da/dt_{II} ; Equation 2 and 3, respectively [35], [55]–[57]. K_{TH} represents the value below which there is either insufficient stress to enable decohesion and/or C_H is below some critical value. The da/dt_{II} plateau is where the crack growth rate values are limited by the ability of the H to diffuse ahead of the crack tip. These models fit the Monel K-500 environmental cracking behavior across all E_A , as shown in Figure 3. The K_{TH} decreased and the da/dt_{II} increased with increasing levels of cathodic polarization [4].

$$K_{TH} = \frac{1}{\beta'} \exp \frac{(k_{IG} - \alpha C_{H\sigma})^2}{\alpha'' \sigma_{YS}} \quad \text{Equation 2}$$

$$\left(\frac{da}{dt}\right)_{II} = \frac{4D_H}{x_{crit}} \left\{ \text{erf}^{-1} \left(1 - \frac{C_{H\sigma-crit}}{C_{H\sigma}} \right) \right\}^2 \quad \text{Equation 3}$$

For Equation 2, β' ((MPa \sqrt{m})⁻¹) and α'' (MPa m) are constants in a dislocation-shielding model of crack tip elastic stress, and α (MPa \sqrt{m} per atom fraction H) is a weighting factor which defines lowering of the Griffith toughness (k_{IG} , MPa \sqrt{m}) per unit H concentration. For Equation 3, D_H is the reversible-trap affected diffusivity of H, x_{crit} is the critical distance ahead of the crack tip

where H cracking nucleates for a discontinuous crack advance increment, and $C_{H0-crit}$ is the critical local concentration of H necessary for H cracking by decohesion at x_{crit} .

The H concentration is dynamically involved with active crack propagation. The H overpotential is associated with the crack tip environment. H will redistribute to align with the hydrostatic stress due to the crack tip stress field such that a crack will nucleate internally at the maximum hydrostatic stress location and propagate back to the free surface [59]. The process will systematically repeat, continuously attracting subsurface H to the fracture process zone.

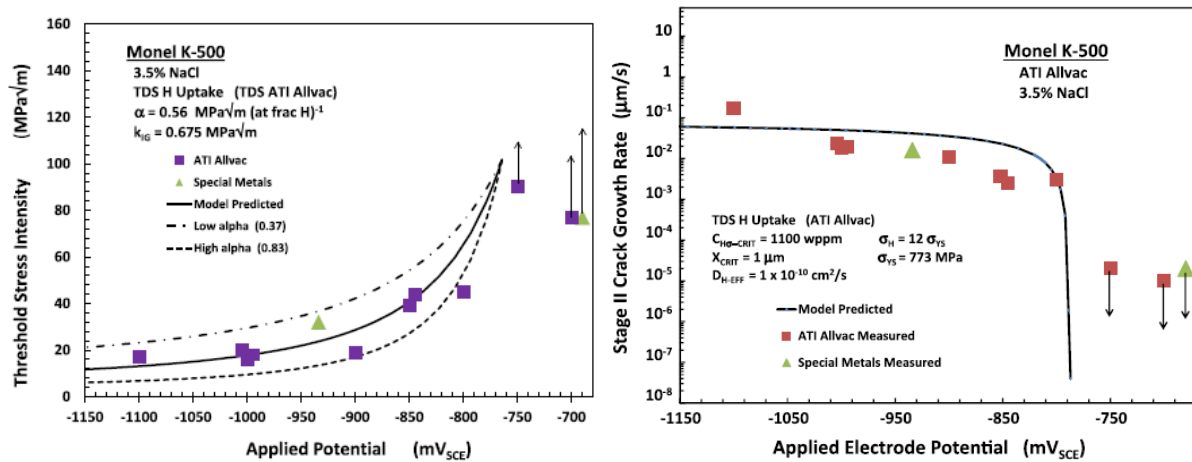


Figure 3: The micromechanical models for K_{TH} and da/dt_{II} associated with their respective experimental data for Monel K-500 with varying applied potential.

There is no comparable documentation for MP98t, though similar trends should exist with crack depth and time but with adjustments for potential due to the compositional and microstructural differences of MP98t.

1.3.2 Loading Rate Effects

The effects of bulk scale loading rate on the hydrogen embrittlement behavior of materials has been thoroughly studied in an effort to identify the controlling mechanisms for multiple material systems. The degrading effects have been analyzed with and without the crack tip context through SSRTs and LFM-based testing, respectively.

SSRTs have identified the dependence of bulk HE on concurrent plasticity and H diffusion time. Scully and Moran showed dramatic decreases in % reduction of area in HE aggressive environments for AISI 4340 steel by focusing on these phenomena [60]. Sufficiently rapid strain

rates defect the protective oxide on the sample surface, creating a pathway for H into the material when simultaneously immersed in an H-producing environment. Unstrained samples in H charged environments with ample time for diffusion did not exhibit embrittling effects when subsequently strained, proving the important role of defecting the oxide film. One mechanism of oxide destabilization is hypothesized to be dislocations arriving to the surface with a frequency that reduces the oxide integrity [61]. The deleterious behavior becomes negligible above a diffusion limiting strain rate that prevents time for an effective H concentration to form via diffusion. These testing methods concluded that H absorption was the rate limiting factor while H diffusion is necessary, but secondary for this alloy system [60]. The diffusion limiting nature of hydrogen embrittlement was reiterated in work by Toribio using constant displacement rate loading on notched cylindrical specimens of high strength steel [62]. A ratio of failure load in environment to failure load in air versus bulk displacement rate was used to assess susceptibility. The failure load plateaued at low displacement rate and increased with increasing rate, thus losing the embrittling effect.

As outlined previously, SSRTs lack the crack tip sensitivity of LFM techniques. The same effects observed in SSRTs, protective films and concurrent plasticity, have strong influences on individual crack growth behavior. The H uptake at a crack tip is a higher severity event than on a smooth surface. The crack tip hydrostatic stresses cause a dilation of the lattice around a crack tip which facilitates an elevated H concentration, causing a more rapid embrittlement effect. Once inside the material, H actively diffuses from the crack tip toward the high stress fracture process zone at the forefront of the crack tip [59]. The concentrated H effect changes the scope of the behavior. The stress state and environmental considerations are different for a sharp crack geometry as opposed to a smooth or notched specimen. These considerations are necessary for accurate failure analysis.

LEFM based testing uses K_{TH} and da/dt_{II} to identify trends in susceptibility. The work by Dietzel et al., shown in Figure 4, shows a strong dependence of K_{TH} on displacement rate, dq/dt , in Al 2024 [41]. The fixed K_{ISCC} at slow dq/dt supports the decohesion based mechanism put forth by Gerberich. A minimum threshold stress is necessary to exceed the Griffith toughness after an adequate H concentration is achieved, the lower plateau indicates sufficient time for H diffusion

to reduce the cohesive strength. The distinct step-wise increase in K_{TH} indicates that the failure process is limited by H diffusion at the higher loading rates. The same trend of decreasing EAC susceptibility with increasing loading rate was noted in STA Beta-21S Ti in work by Somerday [36]. However, the opposite trend was observed for work on Ti-6Al-4V by Richey et al., shown in Figure 5, displays a power law trend of increasing EAC susceptibility (e.g. increasing da/dt_{II}) with increasing dK/dt [63]. Coupled with the differences between the EAC susceptibility of Monel K-500 characterized using the RSL and constant dK/dt testing, these literature findings motivate the current study of the effect of dK/dt on the HEAC susceptibility of Monel K-500 and MP98t.

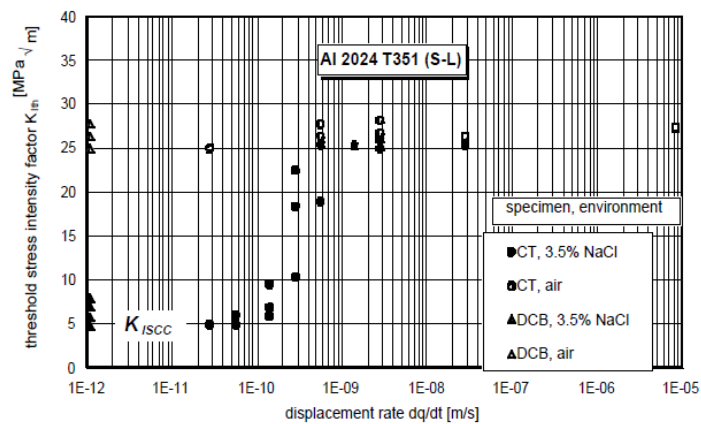


Figure 4: K_{TH} for rising displacement experiments on compact tension (CT) and double cantilever bending (DCB) specimens of Al 2024 T351 in the S-L orientation, performed at various displacement rates. [41]

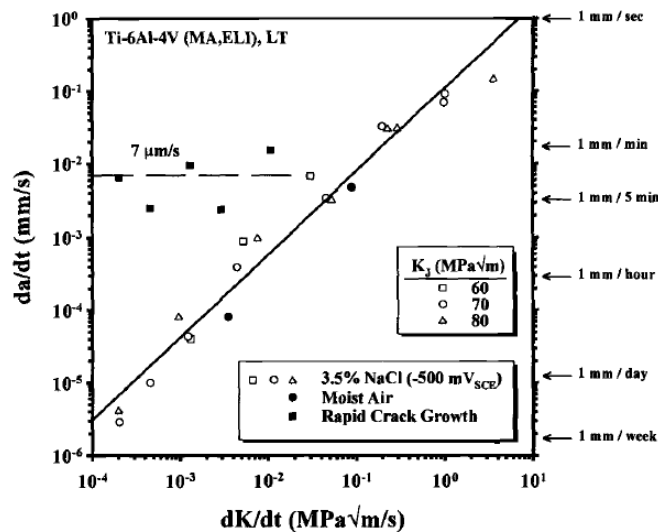


Figure 5: da/dt vs. dK/dt for Ti-6Al-4V plate in 3.5% NaCl, $-0.500V_{SCE}$ and moist air for various loading rate and K_I levels. [63]

1.4 Knowledge gaps, Objectives, and Tasks

The effects of dynamic loading in a H-rich environment have been explored in Al and Ti systems [41], [63], but there is no work available Ni- or Co- based alloys over a significant range of loading rates. LEFM-based approaches provide the most detailed results regarding crack EAC crack growth kinetics of the test methods available. The measurement method will be additionally analyzed and verified for application to high toughness, relatively low yield strength alloys in low EAC susceptibility environments. The extent to which dK/dt affects the onset (K_{TH}) and rate of crack growth (da/dt) in addition to the controlling mechanism of these metrics for Ni- and Co-based superalloys is unknown.

This study will quantitatively characterize and enhance the understanding of the effect of dK/dt on the mechanism controlling HEAC in Ni- and Co-based superalloys. This information will inform the future testing protocol for characterizing such alloys; specifically addressing what dK/dt are appropriate/conservative for future accelerated testing procedures. The work to complete this objective is divided into three tasks:

Task 1: Consider a range of dK/dt and identify and address the challenges associated with data collection techniques to quantify the stress corrosion cracking (SCC) resistance using LEFM based techniques

Task 2: Quantify the effect of dK/dt on the standard LEFM metrics K_{TH} and da/dt_{II} for two different marine alloys at relevant electrochemical polarization(s)

Task 3: Explore the mechanistic underpinnings that govern the effect of loading rate on the SCC behavior of each alloy.

2. Experimental procedure

2.1 Basic Material Characterization

2.1.1 Monel K-500

The Monel K-500 alloy considered in this study was received from the U.S. Naval Research Laboratory (NRL) and underwent a multi-step heat treatment to maximize the strength limits given in material specification QQ-N-286 [7]. The stock used in this study was procured from Special Metals as a 114 mm diameter bar that had been direct-aged at 866 K for 16 hr, furnace cooled at 14 K/hr to 811 K, held for 1 hr, furnace cooled at 14 K/hr to 755 K, held for 1 hr, then air cooled to ambient temperature [38]. This material lot is designated as Monel K-500 NRL High Strength.

The characteristics of this alloy which influence the fracture behavior have been analyzed previously. Using ASTM 112-13, the grains were found to be equiaxed and the mean planar grain diameter was found to be 11.2 μm [38], [64]. Room temperature compression testing was performed on a cylinder cut parallel to the length of the bar to obtain the strain hardening coefficients α and n using the Ramberg-Osgood analysis, the yield strength (σ_{ys}), and the elastic modulus (E) shown in Table 1 [27], [38]. The composition of the alloy used in this study was determined by inductively coupled plasma optical emission spectrometry (ICP-OES) and glow discharge mass spectrometry (GDMS) is given in the Table 1 [38].

2.1.2 MP98t

The material for this study was received as a 3.2 by 3.2 cm square bar with an elongated grain structure parallel to the length of the bar, termed the elongated direction. The exact compositions of the alloy used in this study are given in weight percent in the Table 2. Previous microstructural analysis was not available for MP98t.

Table 1: Test material properties

Material	α	n	σ_{ys} (MPa)	E (GPa)
Monel K-500	0.405	18.04	910	188
MP98t (Elongated Direction)	0.24	19.13	1480	224
MP98t (Normal Direction)	0.28	15.96	1130	199

Table 2: Wt% compositions of Monel K-500 [46] and MP98t, with P, S, and B in wppm (weight parts per million)

Material	Ni	Co	Cu	Cr	Al	Fe	Mo	Mn	Si	Ti	C	P	S	B
Monel K-500	63.44	0.02	30.74	-	3.2	0.91	-	0.85	0.1	0.57	0.14	40	17	2
MP98t	26.61	34.95	-	18.87	0.18	8.58	7.38	0.001	0.09	2.85	0.015	60	20	17

2.2 Mechanical Testing

The HEAC behavior of Monel K-500 and MP98T were quantitatively established in aqueous chloride and inert environments via fracture mechanics based testing. Each sample evaluated in this study underwent a fatigue precrack and a rising K, constant K-rate (dK/dt) test in a controlled environment. Real-time direct current potential difference (dcPD) monitoring of crack extension coupled with software controlled servo-hydraulic frames enables evaluation of the effect of different rising K-rate (dK/dt) on HEAC behavior. This style of experimental set up has been used to test the SCC susceptibility of several materials including other heat treatments of Monel K-500 [38]. All analysis was handled post-test, including computational analysis of experimental data and microscopic inspection of the samples.

2.2.1 Fracture Mechanics Testing

2.2.1.1 Sample description

Single edge notched tension specimens (SENT) with a rectangular gauged cross-section were used. The geometry factor, $Y(a/W)$, used in Equation 1 is defined for this sample geometry in Equation 4 [65]. The gauged section of the MP98t samples had a thickness (B) of 2.66 ± 0.02 mm and width (W) of 10.2 ± 0.02 mm. Monel K-500 samples had thickness of 2.68 ± 0.05 mm and widths that varied between specimens (ranging from 10.67-12.51 mm). An electrical discharge machined (EDM) notch was cut across the thickness to a depth of 0.20 ± 0.02 mm. The loading axis was perpendicular to the notch with Mode 1 crack growth occurring in the radial direction. In the case of MP98t, also parallel to the elongated direction, as such, the mechanical properties associated with the elongated direction are used for analysis.

$$Y\left(\frac{a}{W}\right) = \sqrt{\frac{2W}{\pi a} \tan \frac{\pi a}{2W}} * \frac{0.752 + 2.02\left(\frac{a}{W}\right) + 0.37\left(1 - \sin \frac{\pi a}{2W}\right)^3}{\cos \frac{\pi a}{2W}} \quad \text{Equation 4}$$

2.2.1.2 Sample Preparation

Prior to each test, specimens were sonicated in acetone, methanol, and deionized water for 15 minutes each to remove debris on the surface and inside the notch, then blown dry with compressed air to prevent residue. The side view of an SENT test section prepared for a submerged environment is shown in Figure 6. For electrochemical environments, the majority of the surface was covered with 3M Electroplating Tape 470 and a butyl rubber-based lacquer, Tolber Micro XP-2000 Stop-off Lacquer (orange). A 1 mm width window of the test section about the Mode I crack path was left exposed, this window was centered around the EDM notch and extends to a ratio of exposed width to full sample width of 0.7. The masking lacquer and tape limited the area that the applied environment could affect, protecting the sample from side cracking and dcPD wires from electrochemical degradation during the HEAC test [37]. The sample surface was left bare in inert environments.

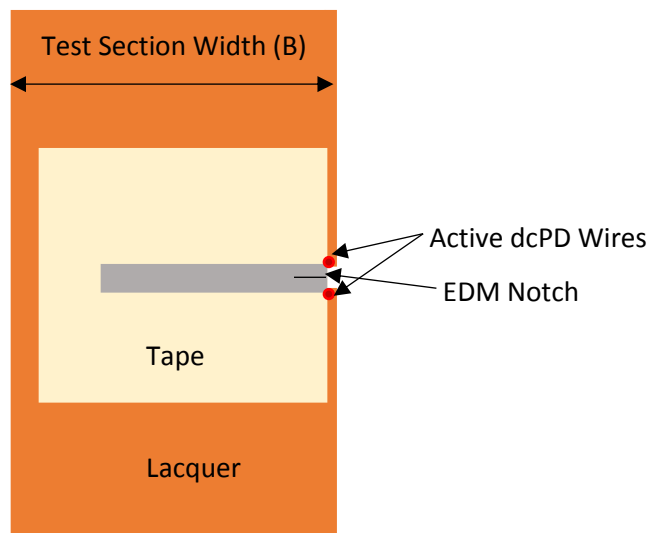


Figure 6: Side view of SENT sample test section.

2.2.1.3 Load Application

An active feedback loop connecting the dcPD crack length measuring system and the servo-hydraulic actuator controlling software from Fracture Technology Associates (FTA) was established to accurately apply appropriate load and displacement during the sample precrack and dK/dt controlled experiment. Crack length accuracy was of critical importance to actively applying the necessary K . All testing was done in clevis grips that allowed for free rotation of the sample in compliance with K-solution boundary conditions [65].

2.2.1.4 Direct Current Potential Difference (dcPD)

The dcPD system correlates a change in electrical resistance to a crack length by the Johnson's Equation (Equation 5), allowing for active measurement of the crack growth rate [66]. This system has been rigorously utilized to analyze a wide range of cracking situations. The dcPD system has been heavily used and is exceptionally accurate for materials testing that: (1) does not approach the yield stress, proportional limit, or limit load of the material, such as fatigue testing, (2) high strength materials with relatively low toughness, and (3) in environments that promote cracking at low applied loads. These criteria are not met in by the conditions of interest in this study. Monel K-500 exhibits a relatively high toughness with low strength and is examined in a low HEAC susceptibility environment with a rising load. This unique combination of properties requires a rigorous investigation of the method and development of a protocol to ensure unambiguous characterization of HEAC, which will be explored in Task 1.

For both Monel K-500 and MP98t tests, a constant current of 4.000 ± 0.001 A was applied to the sample and the voltage between pairs of Alumel active wires spot welded 0.5 ± 0.1 mm above and below the notch and reference wires welded at the far edges of the gauge section was collected. The signal from the active wires was amplified by 2000 times to distinguish the minute changes in resistance due to plasticity and crack growth. The voltage change was interpreted using Johnson's Equation, Equation 5, in which V is the measured voltage, V_0 is the initial voltage value averaged during a 1 hour hold prior to test initiation, y is the distance between active wires, W is the specimen width, a is the calculated crack length, and a_0 is the crack length at which V_0 was obtained. Johnson's Equation was used to generate non-destructive instantaneous crack length measurements [66], [67]. This method and current have been shown to resolve 0.1 μ V differences as 0.5 μ m changes in crack growth [68].

$$\frac{V}{V_0} = \frac{\cosh^{-1} \left[\frac{\cosh\left(\frac{\pi y}{2W}\right)}{\cos\left(\frac{\pi a}{2W}\right)} \right]}{\cosh^{-1} \left[\frac{\cosh\left(\frac{\pi y}{2W}\right)}{\cos\left(\frac{\pi a_0}{2W}\right)} \right]} \quad \text{Equation 5}$$

The measured voltage could be influenced by temperature, sample plasticity, electrical shorting, and crack growth. Crack growth was the only factor of interest so the other influences are accounted for or removed during data collection and post-test analysis. Temperature effects on the voltage were removed by applying a polarity reversal and the readings were averaged

over 50 data points [68]. Additional corrections made to dcPD measurements will be discussed in the Post-test Corrections and Task 1 of the Results and Discussion section.

2.2.1.5 Fatigue precrack

Monel K-500 and MP98t samples underwent similar precrack procedures in preparation for the dK/dt testing. Precrack growth was monitored using the dcPD system and controlled using FTA Fatigue Crack Growth software (FCGR). Prior to precracking, samples were placed under a cycling 1 kN maximum load with a $R=0.1$ for 1 hour to determine initial dcPD voltages associated with the EDM notch length, V_o of Johnson's equation [68].

MP98t samples underwent one of two precrack procedures. Samples tested at a dK/dt of 0.2 and 2 $\text{MPa}\sqrt{\text{m}}/\text{hr}$ were fatigue cracked at $R=0.1$ and a constant $K_{\text{max}} = 12.9 \text{ MPa}\sqrt{\text{m}}$ until a crack length of 0.33 mm, followed by a K-shed from 15.6 to 15.0 $\text{MPa}\sqrt{\text{m}}$, ending at a crack length of 1.00 mm. All other samples were fatigued at a constant maximum load equal to 10.253 kN until a crack length of 0.40 mm, followed by a K-shed from 15.5 to 11 $\text{MPa}\sqrt{\text{m}}$, ending at a final crack length of 1.00 mm.

Monel K-500 samples were fatigue cracked with a constant maximum load of 11.54 kN to a crack length of 0.80 mm, followed by further cracking to 0.90 mm at $R=0.1$ and a constant $K_{\text{max}} = 20 \text{ MPa}\sqrt{\text{m}}$, before finally conducting a K-shed to 10 $\text{MPa}\sqrt{\text{m}}$ to achieve a crack length of 1.00 mm. During the K-shed, crack growth would occasionally stop prior to 1.00 mm due to ΔK falling below the crack growth threshold. For some specimens, a short loading sequence, where R values included 0.1, 0.5, and 0.7 with a constant K_{max} up to a crack length of 0.9mm, was imparted in an attempt to mark the fracture surface and provide a visual crack length validation on the fracture surface. Though this marker banding method is shown to be useful on some materials [69], it was found to be ineffective in the current application, with no obviously observable differences in the fracture surface. All fatigue procedures resided in frequency range of 1 and 25 Hz in laboratory air, depending on the capabilities of the individual test frame. The final precrack length calculated by dcPD, usually 1mm, was used as the initial value of the slow rising K test.

2.2.1.6 Environmental Control

All HEAC experiments were run in a 270 mL Plexiglas® cell with ports for 2L of 0.6 M NaCl solution to be circulated through the cell at a rate of approximately 20 mL/min. The initial pH was approximately 5.6 and typically rose to ≈ 6.6 at the conclusion of the test, with longer experiments experiencing a larger rise in pH. A constant applied potential referenced to a standard calomel electrode (SCE) was applied by a potentiostat operating in floating mode to avoid a ground loop. A platinum coated Nb mesh counter electrode encircled the sample inside the cell and the stripped end of copper wire was coiled around the bottom of the sample, outside the cell and insulated from the metallic grip, to act as the working electrode. The constructed environmental cell is shown in Figure 7.

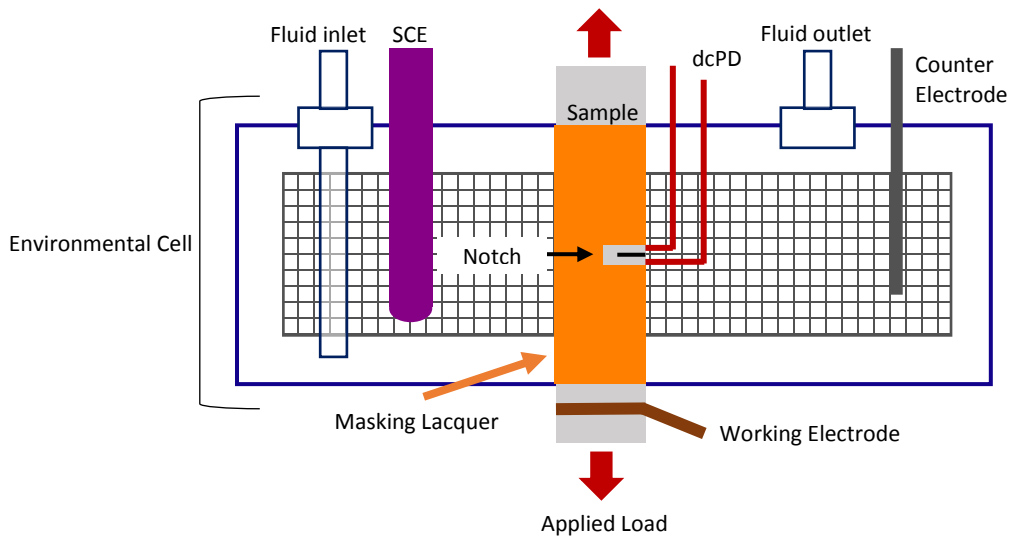


Figure 7: Assembled environmental cell with sample for immersive testing in polarized environments.

The experimental matrix designed to capture the effect of dK/dt on the HEAC behavior was established at electrochemical conditions that are considered aggressive, mild, and inert for both materials is shown in Tables 3 and 4. Extensive prior testing of Monel K-500 at a dK/dt of 0.33-1 MPa \sqrt{m}/h has established the effect of different electrochemical conditions on the HEAC susceptibility [4]. Specifically for a 0.6M NaCl electrolyte, polarization at $-0.950 V_{SCE}$ results in HEAC, $-0.850 V_{SCE}$ produces lot-dependent mild HEAC, and no HEAC was observed in dry N_2 environments [38]. A similar extensive fracture mechanics based characterization of the HEAC behavior of MP98T was not available in the literature.

Table 3: Constant dK/dt and environmental experiment parameters for Monel K-500

Environment\ dK/dt (MPa√m/hr)	0.075	0.1	0.15	0.2	0.33	1.0	2.0	3.0	4.0
-0.950 V _{SCE}	X	X	X	X	X	X	X	X	X
Dry N ₂		X			X	X	X	X	X

Table 4: Constant dK/dt and environmental experiment parameters for MP98t

Environment\ dK/dt (MPa√m/hr)	0.2	0.33	1.0	2.0
-1.30 V _{SCE}	X	X	X	X
Dry N ₂			X	

2.2.1.7 K Test Protocol

In order to achieve the desired dK/dt in Tables 3 and 4, the real-time dcPD-based crack length data was coupled with software (Fracture Toughness Associates Non-Linear Fracture Toughness (FTA NLFT)) which performs fracture mechanics calculations to command the servo-hydraulic frame operation. This software assumes cracking in the LEFM regime, as such small scale plasticity corrections are made post-test. In preparation for the slow rising K HEAC testing, the SENT sample was placed into the empty environmental chamber and a 1 kN hold was performed for 1 hour to collect initial dcPD value, V_o , associated with the precrack length. The cell was then filled with prepared 0.6M NaCl solution and the open circuit potential (OCP) was monitored for 1 hour, followed by polarization to the test potential and a 1 hour hold before initiating the K-rise. Over the first hour of the K-rise, the K is raised at a linear rate to 10 MPa√m, as a start point for the dK/dt test. For the Monel K-500 test with dK/dt = 4.0 MPa√m/hr, this value was reduced to 6 MPa√m to accurately capture K_{TH} . The dK/dt was then set at the rate of interest for increasing K above 10 MPa√m. Tests were concluded when bulk section yielding or side cracking occurred.

The procedure for testing in the inert dry N₂ environment was very similar to the electrochemical environment set up. The sample was placed in the environmental cell and all openings are blocked with tape except for the fluid inlet and outlet. The inlet was attached to a compressed gas cylinder containing dry N₂ and the end outlet tube was submerged in a beaker of water to prevent back flow. A Relative Humidity (RH) meter was added to the cell though one

of the otherwise sealed ports. The cell was purged with N_2 and the humidity was monitored. After the RH reached 1.0%, the 1 hour 1kN load hold was initiated to determine the initial dcPD values. The K-rate test began immediately at the conclusion of the 1 hour hold with the same ramp up to 10 MPa \sqrt{m} and test rate continuation as the electrochemical tests. Inert testing was used to inform on plastic zone behavior and bulk scale yielding. For $dK/dt < 0.33$ MPa \sqrt{m}/hr , testing was halted when substantial information for a resolution limit (e.g. the amount of electrical resistance attributed to the plastic zone) was established. The resolution limit protocol is expanded upon in section 3.2.3.2. Tests at higher inert dK/dt were concluded when bulk section yielding occurred.

2.2.1.8 Post-test Fatigue

Some samples, after experiencing the dK/dt test, were removed from their environment and subjected to fatigue in order to physically mark the end of the test on the fracture surface. Due to large end of test loads, the post-test fatigue was started at $K_{max} = 35$ MPa \sqrt{m} and $R=0.3$ to surpass the crack tip retardation experienced at lower K_{max} while preventing damage to the preexisting fracture surface. Once stable crack growth was established, the K_{max} would be decreased to 25 MPa \sqrt{m} . In the Monel K-500 the post-test fatigue protocol produces a transgranular crack morphology that is discernable from the intergranular stress corrosion cracking (IG-SCC) and the ductile microvoid final failure.

2.2.1.9 End of Test Procedure

At the conclusion of the K-rate testing the specimen was removed from the environment and loaded in tension until failure. The fractured specimen was then sonicated in acetone, methanol, and deionized water for 15 minutes each to remove surface debris. After each step, the surfaces were blown dry with compressed air to prevent residue. Fracture surfaces were cut from the sample stubs and viewed in a scanning electron microscope (SEM) using secondary mode (SE). Pre-crack and final crack lengths were determined by averaging seven or more equally spaced measurements across the SEM fracture surface. These values could then be compared with dcPD calculations for the pre-crack and final crack length. True crack length values for the pre-crack and SCC, based on SEM measurements of fractographic markers, were used in the post process analysis to develop the da/dt vs. K_I data.

2.2.1.10 Post-Test Analysis

2.2.1.10.1 Elastic-Plastic Analysis

To increase the accuracy of the analysis, the localized ligament plasticity was considered by incorporating plastic J-analysis for Monel K-500. While the instantaneous elastic K was used to control the test in the FTA NLFT software, the post-test analysis uses a Matlab script to analyze the raw data (specimen dimensions, dcPD voltage, applied load, and time) and to calculate the da/dt versus elastic-plastic stress intensity (K_J) relationships. Due to the high toughness relative to the yield strength of Monel K-500, it was important to consider plasticity contributions to the crack tip driving force. Specifically, K_J is comprised of elastic contributions calculated using the well-established solution for SENT samples and the plastic contributions was derived from an elastoplastic J-integral correction for stationary crack in a material that deforms by the Ramberg-Osgood flow rules was applied to the data [27], [70]. The bulk ligament, not including the plastic zone affected region, must remain LEFM in character for the J-analysis to be applied. These calculations were done in accordance with Equation 6, assuming plane strain conditions ($E' = E/(1 - \nu^2)$), where E is the elastic modulus and ν is Poisson's ratio).

$$K_J = \sqrt{(J_{Elastic} + J_{Plastic})E'} = \sqrt{\left(\frac{K_I^2}{E'} + J_{Plastic}\right)E'} \quad \text{Equation 6}$$

K_I is calculated using the effective crack length, a_{eff} , Equation 7, which accounts for the real crack length, a , and the plastic zone. P is the applied load, P_o is the limit load, and σ_{YS} is the yield strength.

$$a_{eff} = a + \frac{1}{6\pi\left(1 + \left(\frac{P}{P_o}\right)^2\right)} \left(\frac{n-1}{n+1}\right) \left(\frac{K_I}{\sigma_{YS}}\right)^2 \quad \text{Equation 7}$$

The plastic contribution in Equation 6 is described below in Equation 8. α and n are Ramberg-Osgood constants, W is the sample width, and h_1 is a constant dependent on the crack length to width ratio (a/W) and n determined by interpolation of values from the EPRI tables [27]. The material specific Ramberg-Osgood constants, yield strength, and elastic modulus determined via compression testing are given in Table 1.

$$J_{Plastic} = \frac{\alpha\sigma_{YS}^2}{E} a \frac{(W-a)}{W} h_1(n, a/W) \left(\frac{P}{P_o}\right)^{n+1} \quad \text{Equation 8}$$

The limit load (P_0) used in the J-analysis is described in Equation 9. β is 1.455 for plane strain in an SEN(T) type sample and B is the thickness [70].

$$P_o = \beta \left(\sqrt{1 + \left(\frac{a}{W-a}\right)^2} - \left(\frac{a}{W-a}\right) \right) (W - a) B \sigma_{YS} \quad \text{Equation 9}$$

The procedure above enables calculation of the elastic-plastic crack tip driving force values for the applied load and crack size of interest; however, it is still necessary to pair these values with the relevant crack growth rate. To do so, and reduce noise, the data were then binned such that at least 80 data points are included for each data set. The instantaneous crack growth rate (da/dt) was then calculated using a seven point polynomial from ASTM E647-13 Appendix XI [71]. The da/dt vs K_J (or K for MP98t) data is used for behavioral analysis.

2.2.1.10.2 Post-test Correction Procedures

Due to the sensitivity of the dcPD system, the voltage induced by the change in electrical resistance associated with electrical shorting, crack tip plasticity, and bulk ligament yielding indicated false crack behavior. Electrical shorting in the crack wake due to the degradation of the surface oxide film within a cathodically polarized environment caused the dcPD system to report a crack length decrease after the initial polarization. Clearly such behavior is not realistic and must be accounted for in post-processing. This shorting quickly disappeared as the crack mouth opened and is considered false crack growth. Shorting is accounted for in the post-processing of the data in accordance with the procedure described by Gangloff et. al [4].

The electrical resistance due to crack tip plasticity has previously been identified and has traditionally been accounted for using a resolution limit [4], [38]. The level of crack tip plasticity scales with increasing K [4] and establishes a functional resolution limit on growth rate below which it is not possible to delineate real crack advance from plasticity effects. The resolution limit was set by running a constant dK/dt test of a precracked SENT sample in an inert environment where no real crack growth occurs below the K_{IC} of the material. Any changes in the dcPD readings would result from either crack tip plasticity, the plastic zone, or crack tip blunting, extension of the crack front. Prior efforts have found that the expected blunting is minimal for the applied K ranges of interest [4]. Initially, this behavior was hypothesized to be

associated with loading rate dependent enhanced plasticity in the precipitate free zones proximate to impurity carbide particles [4]. However, a more detailed investigation will be presented in the current study which suggests an alternate hypothesis.

2.2.1.11 Metrics of Interest

The threshold stress intensity (K_{TH}) and the stage II crack growth rate (da/dt_{II}) are common metrics for analyzing HEAC susceptibility [4]. K_{TH} is functionally defined as the K_I at which the resolution limit is surpassed. This is consistent with the contention that dcPD readings above the resolution limit during the slow rising K test are considered real crack growth. da/dt_{II} is defined as the K-independent crack growth rate, this interpretation was not used in the final analysis. The reasoning for this and the substitute metric used are outlined in Task 1.

2.2.2 Electrical Resistance Measurements of Smooth Tensile Bars

To help decouple the role of plasticity on the dcPD signal it was necessary to quantify the bulk change in electrical resistance with increasing load in Monel K-500. A smooth dog bone style tensile specimen with test section length of 34mm, width of 12.7mm, and thickness of 3.15mm was used. A pair of dcPD wires, were welded 1.05 mm apart in the center of the thin side to simulate an SENT without a crack. The test frame used hydraulic grips to grasp the enlarged portion of the dog bone sample outside the test region. The test was run at a constant displacement rate of 0.60 mm/hr and the dcPD data were recorded in the same manner as the LEFM tests, though the collected data was not actively used to influence the loading protocol, distinct from the LEFM testing. The test was allowed to run to final failure in lab air. The applied load, actuator displacement, and dcPD voltage were recorded during the test.

3. Results and Discussion

A strong loading rate effect has been demonstrated for several material systems in aggressive environments [35], [41], [63]. The dcPD crack monitoring protocols have been shown to provide high fidelity crack extension data however due to this high level of sensitivity it is necessary to decouple the true crack growth from other plasticity based readings. As such, identifying the physical phenomena corresponding to dcPD measurements is pertinent for accurate data analysis. To ensure the rigor of the experimental data, the measurement methods used in this work were investigated in relation to the material behavior of interest. This work has been organized into three tasks to justify the advancements made to the analysis techniques in addition to identifying the effects of loading rate on the environmental crack growth of Monel K-500 and extends them to a similar material system, MP98t. After describing the initial data, Task 1 focuses on rigorously identifying the mechanical behavior that contributes to the crack growth rate perceived by the dcPD system for the initial data set, Task 2 quantifies the loading rate dependence of the HEAC susceptibility, and Task 3 explores the mechanisms responsible for the trends identified in Task 2.

3.1 Initial Data and Experimental Findings

3.1.1 dcPD Sensitivity

The dcPD technique has been shown to have micro-volt level sensitivity, translating into sub-micron level fidelity in monitoring crack extension. Informed interpretation of the dcPD signal based on physical phenomena is necessary for accurate analysis. Johnson's Equation (Equation 5 in the Experimental Methods) used for analyzing the voltage measured around the crack tip assumes that the changes in the electrical resistance is due to crack growth based on a reduction in cross-sectional area [66]. Equation 10 is the general equation for the electrical resistance of a material; where R is the electrical resistance, ρ is the material resistivity, l is the length of interest, and A is the cross-sectional area.

$$R = \rho \frac{l}{A} \quad \text{Equation 10}$$

This assumption is accurate so long as other electrical resistance generating phenomena remain comparatively minute. In addition to crack growth, material loading can cause plastic deformation which has been shown to generate electrical resistance [72]. The formation and

accumulation of dislocations changes the resistivity of a material by distorting the lattice to reduce the electron mean free path [73].

Plastic deformation can be formed in a localized region in front of a crack tip due to stress concentration [27]. The constrained region around the crack tip experiences an elevated stress beyond the yield stress, enabling dislocation formation and motion. The size of the plastic zone, r_p , is depicted in Figure 8 and traditionally defined by Equation 11; where K_I is the stress intensity and σ_{YS} is the yield strength [27]. The plastic zone forms independently of fracture. Electrical resistance due to the growth of the plastic zone prior to fracture has been detected using the dcPD system. The “apparent” crack growth rate is quantified as the lower bound of crack growth resolution for the dcPD system. In prior efforts, quantifiable crack growth was only considered, after the dcPD signal surpasses this resolution limit [4].

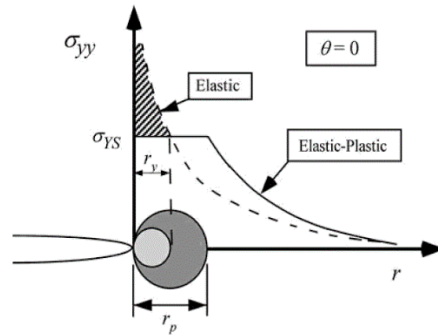


Figure 8: The size of the plastic zone in front of the crack tip is related to the force concentrating behavior. The plastic zone exists where the local stress exceeds σ_{YS} . Figure from Anderson [27]

$$r_p = \frac{1}{\pi} \left(\frac{K_I}{\sigma_{YS}} \right)^2 \quad \text{Equation 11}$$

It was hypothesized that the magnitude of the resolution limit scales linearly with dK/dt . As shown in Equation 11 the radius of the crack tip plastic zone is directly proportional to K^2 such that as dK/dt increases, dr/dt and therefore the apparent da/dt , when dependent only on the plastic zone, should scale directly. This hypothesis has not yet been rigorously tested

experimentally, but its evaluation is necessary for quantifying the localized plasticity contribution of each experimental dK/dt .

3.1.2 Initial Characterization of Growth Rate versus Stress Intensity

The environmental crack growth data for all tested dK/dt of Monel K-500 in 0.6M NaCl solution polarized to $-0.950 V_{SCE}$ is displayed below in Figure 9 with the only historical correction for shorting, described previously, taken into account. For each dK/dt the da/dt increases monotonically. A low magnification view of the fracture surface for each test is examined in secondary mode in the SEM in Figure 10. Each surfaces displays three principle fracture morphologies representative of distinct behavior. The regions are highlighted in Figure 11 and correspond to the regions in Figure 10: transgranular (2a), intergranular (2b), and microvoid coalescence, or ductile failure (2c). The transgranular (TG) region corresponds to fatigue crack growth, the intergranular region is the standard HEAC morphology for Monel K-500 [4], and the microvoid region is consistent with final failure. While the fractography is useful in informing the fracture mechanism, the crack growth rate interpreted by the dcPD system should quantitatively correspond to these observed changes in morphology.

To evaluate the fidelity of the dcPD system, environmental tests of SENT samples at $-0.950V_{SCE}$ at various dK/dt were interrupted at incremental K_I values and the total crack length from the fractography (including the notch, precrack, and intergranular SCC growth) was compared to the end-of-test dcPD measured crack length. The fracture surface measurements were done at low magnification in secondary mode using an SEM. The K_I at which the test was interrupted, the final SCC crack length, the final dcPD measured crack length, and the percent difference between the two crack lengths for each dK/dt are listed in Table 5.

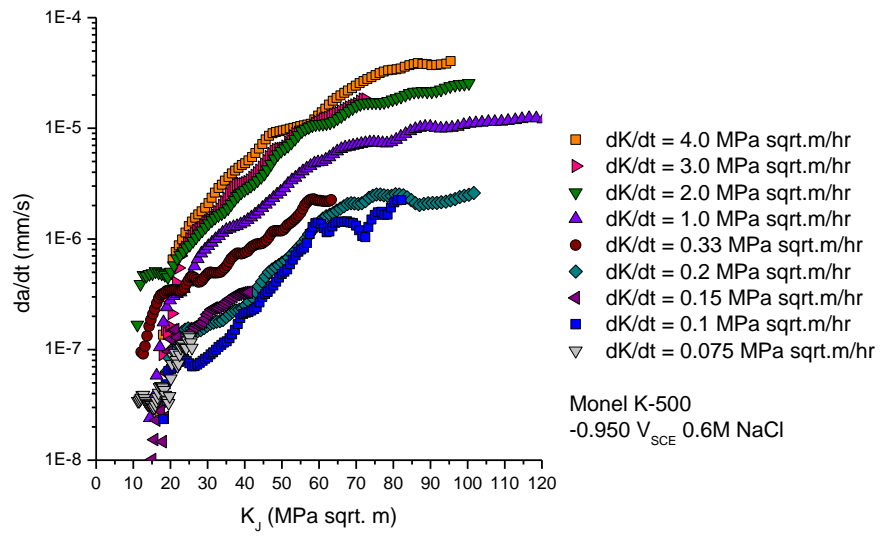
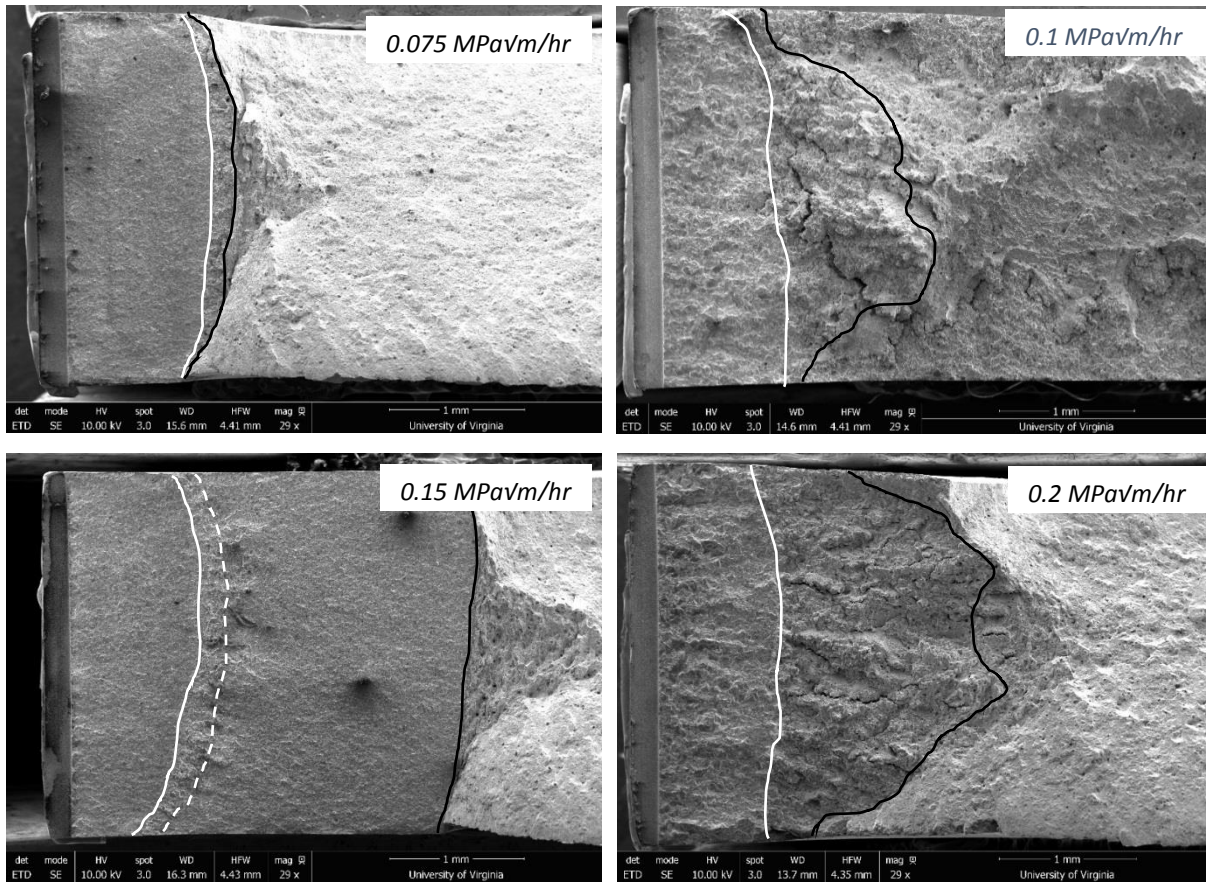


Figure 9: da/dt vs K_j data from all Monel K-500 experiments in 0.6 M NaCl with $E_A = -0.950 V_{SCE}$. Only the historic correction for crack tip shorting has been made to this data set.



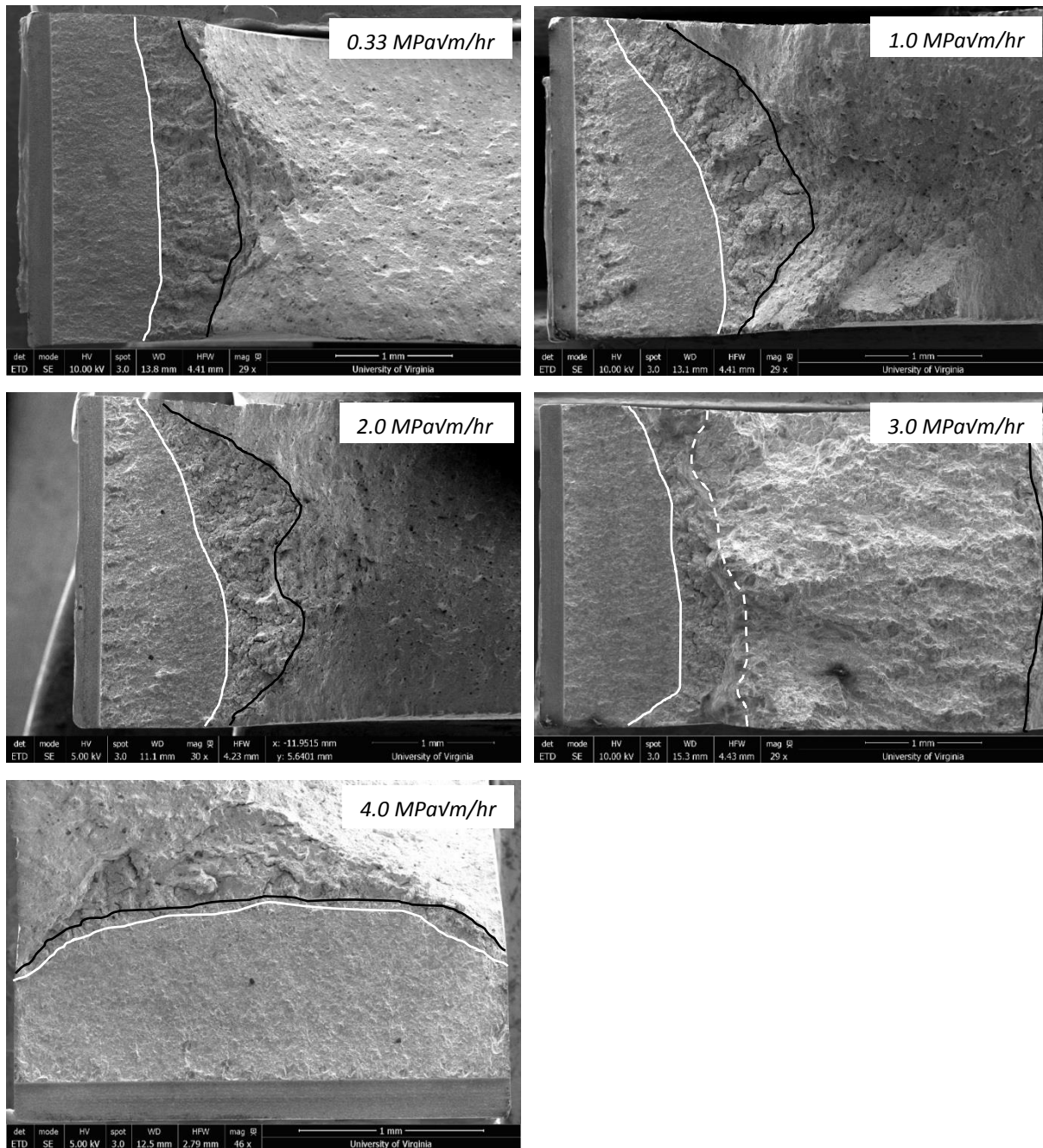


Figure 10: Fracture surfaces of Monel K-505 in 0.6 M NaCl with $E_A = -0.950 V_{SCE}$, corresponding to the data in Figure 9. The crack propagates from left to right in all micrographs except $dK/dt = 4.0$ MPavm/hr in which the crack propagated from bottom to top. The lines indicate transition points on the fracture surface: continuous white = end of precrack, dashed white = start of post-test fatigue, black = start of final failure.

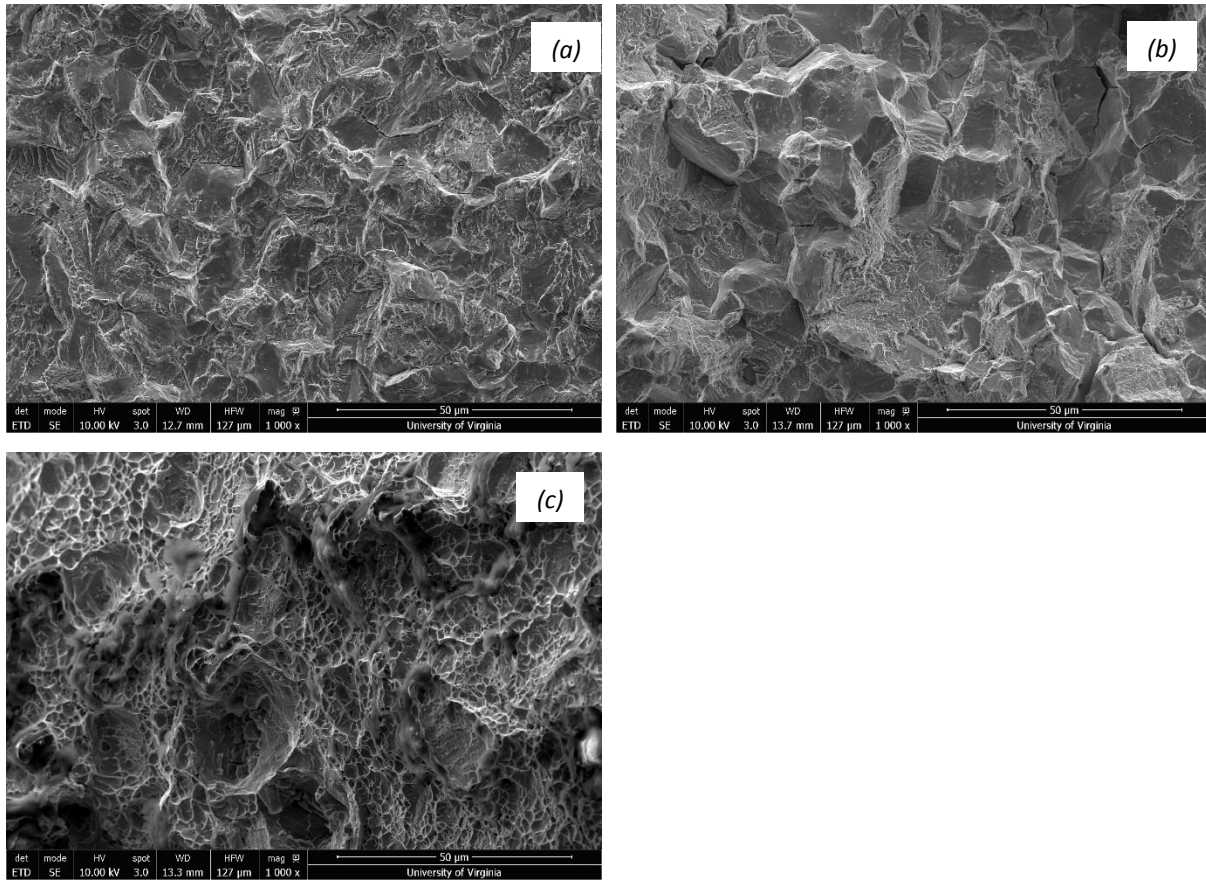


Figure 11: The three main fracture mechanisms displayed in this work: (a) transgranular (TG) fatigue, (b) intergranular stress corrosion cracking (IG-SCC), (c) microvoid coalescence, ductile failure.

Table 5: Crack growth information for the Monel K-500 fixed dK/dt tests in 0.6 M NaCl, $E_A = -0.950 V_{SCE}$

dK/dt (MPavm/hr)	Pre-crack a (mm)	End K_I (MPavm)	Final a (mm, SEM)	Final a (mm, dcPD)	Percent Difference
0.075	1.22	27	1.36	1.35	0.5
0.1	1.05	82	1.66	2.54	34.8
0.15	1.11	41.5	1.28	1.25	2.2
0.2	1.05	101	1.80	2.57	30.0
0.33	1.08	63	1.63	1.58	3.2
1	1.19	120	1.83	2.80	34.6
2	1.01	100	1.48	2.30	35.6
3	1.12	74	1.39	1.51	8.0
4	1.09	95	1.16	2.03	42.8

The percent difference in the final crack lengths ranges far larger than the acceptable error of 5%. The percent difference in correlation with ending K_I is depicted in Figure 12. The percent difference sharply increases with increasing K by a large stepwise shift from <5% to >30%

error occurring around $K = 70 \text{ MPa}\sqrt{\text{m}}$. The rapid increase in error with $K_{J,\text{end}}$ suggests an error causing phenomenon that is isolated to high K_J values. It is critical for the interpretation of the dcPD data that the source of this error is understood. As such, identifying other contributions to electrical resistance will be critically evaluated in Task 1.

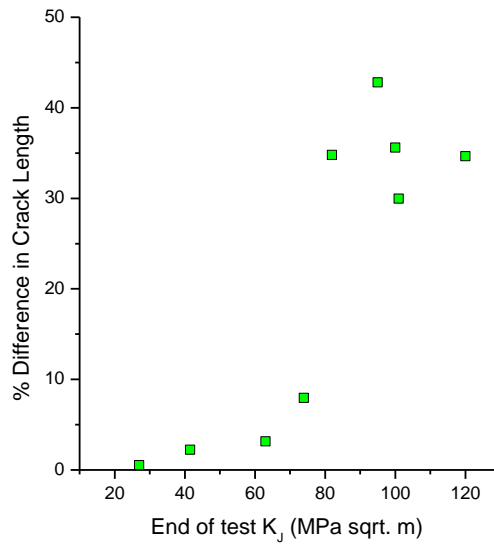


Figure 12: The percent difference in crack length between the apparent dcPD value and the end of IGC behavior compared to the apparent interrupted K_J for all tests in 0.6M NaCl, $E_A = -0.950 \text{ V}_{\text{SCE}}$.

3.2 Task 1: Identify the challenges associated with dcPD testing techniques to quantify IG-SCC resistant materials using LEFM based techniques

The large error in final crack length for experiments ending at high K_I , shown in Figure 12, suggests that the causal error occurs only in the high K_I regime. Additional electrical resistance generating phenomena beyond intergranular crack growth must be considered in order to understand the error. The error causing phenomena can be concurrent with the high K_I crack growth (plastic behavior) or a transition from IG-SCC to a different failure mechanism (ductile tearing). By the current testing protocol, these effects are undetectable on the fracture surface. Ductile tearing likely exhibits the same fracture morphology as the post-test failure behavior and is therefore indistinguishable without a change in testing protocol. The hypothesized phenomena are not environmentally dependent, and as such, can be more clearly analyzed in an inert environment. Inert testing of SENTs has been previously used to quantify localized plasticity; this work will expand the analysis to higher K_I to identify the pertinent behavior and its loading rate dependence.

3.2.1 Inert Environment Testing Data

Precracked SENT samples of Monel K-500 were tested at a range of dK/dt , the same loading protocols as the environmental tests, but in a dry N_2 environment ($RH < 5\%$). The dcPD calculated crack growth for all SENT tests in inert environments; $dK/dt = 0.1, 0.33, 1.0, 2.0, 3.0,$ and 4.0 MPa \sqrt{m}/hr ; are shown in Figure 13. The fracture surfaces corresponding to each test are displayed in Figure 14. The crack propagates from left to right in all micrographs, except $dK/dt = 4.0$ MPa \sqrt{m}/hr in which the crack propagated from bottom to top. Transition points in testing protocol are indicated by lines on the fracture surface: continuous white equals end of precrack, dashed white equals start of post-test fatigue, black equals start of final failure. $dK/dt = 0.1, 1.0, 2.0,$ and 3.0 MPa \sqrt{m}/hr each underwent a post-test fatigue protocol, the remaining tests did not. $dK/dt = 0.33$ and 4.0 MPa \sqrt{m}/hr were loaded to failure immediately after the dK/dt test protocol concluded. The fracture surface for $dK/dt = 0.1$ MPa \sqrt{m}/hr will not be considered in the proceeding analysis due to a rapid rise in load after the dK/dt test, but prior to the post test fatigue. The K_I at which each test was ended, the precrack length, crack length at which the TG post-test fatigue begins (for indicated dK/dt), and the dcPD final calculated crack length for each dK/dt are included in Table 6.

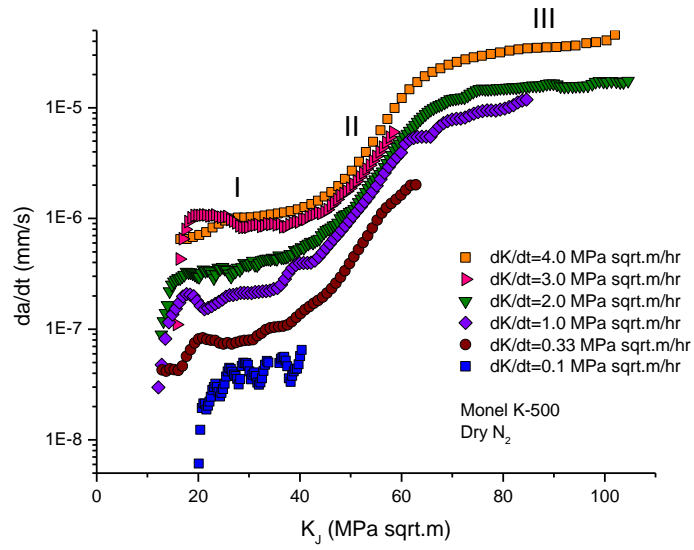
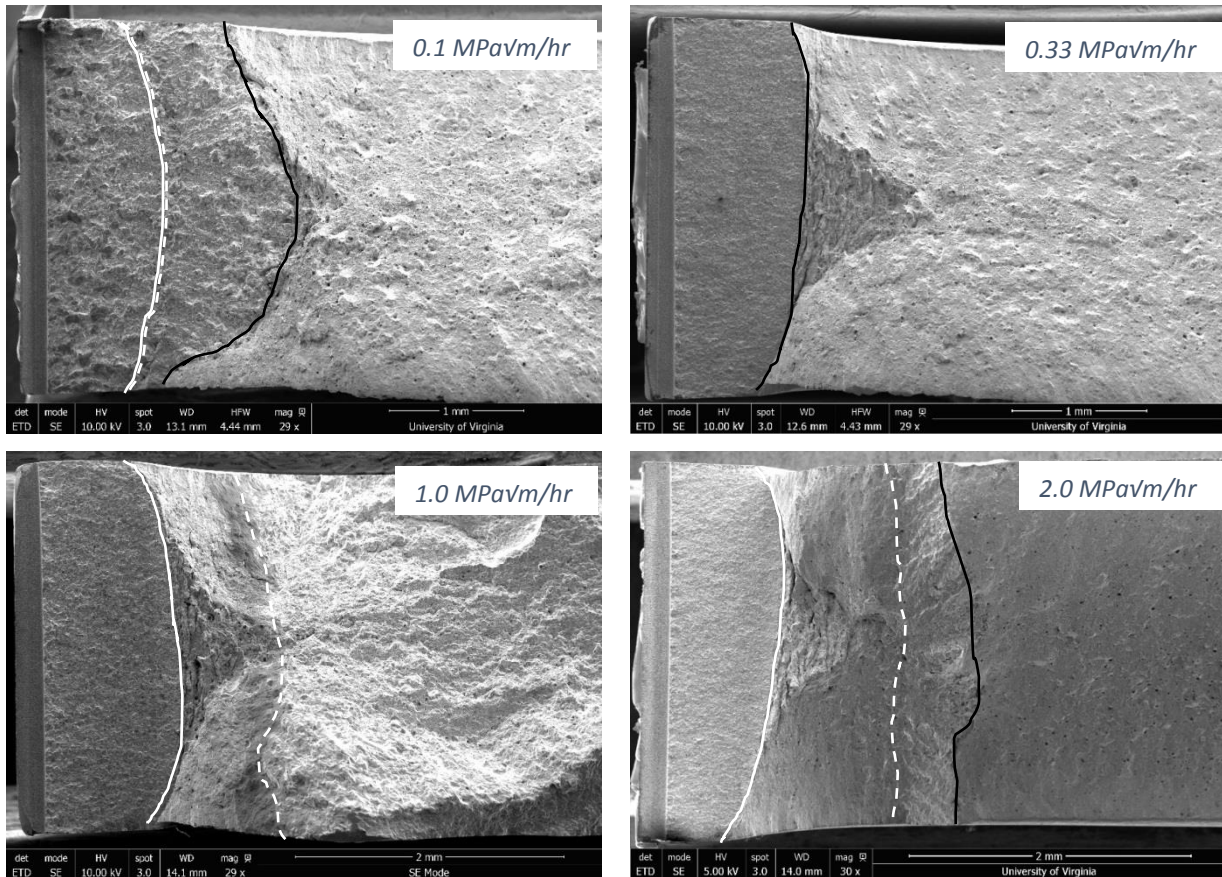


Figure 13: The apparent da/dt vs K_I of Monel K-500 at fixed dK/dt in dry N_2 . I, II, and III correspond to regions of near constant slope, indicating different controlling behaviors on the dcPD signal.



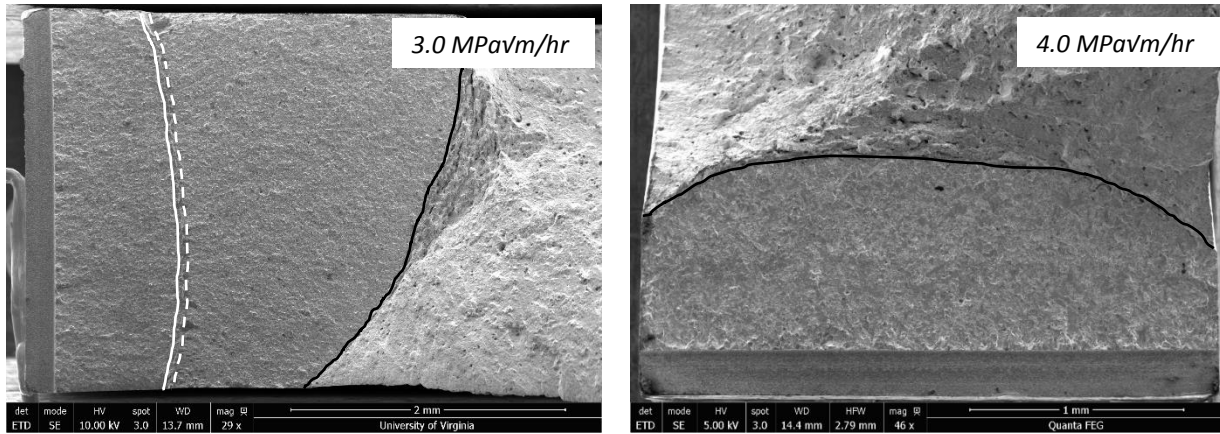


Figure 14: Fracture surfaces of Monel K-500 in Dry N₂, corresponding to the data in Figure 13. The crack propagates from left to right in all micrographs except $dK/dt = 4.0$ MPaVm/hr in which the crack propagated from bottom to top. The lines indicate transition points on the fracture surface: continuous white = end of precrack, dashed white = start of post-test fatigue, black = start of final failure. If two lines occupy the same space, the later occurring event is shown.

Table 6: The ductile crack length comparison between the SEM measured value and the apparent dcPD value for dry N₂ samples.

dK/dt (MPaVm/hr)	K_j end (MPaVm)	Precrack a (mm)	$a_{end\ dK/dt}$ (mm)	a_{dcPD} (mm)
0.1	41	1.02	-----	1.05
0.33	65	1.08	-----	1.17
1.0	98	1.15	1.90	2.01
2.0	115	0.90	1.86	2.16
3.0	61	1.07	1.12	1.15
4.0	107	1.02	-----	2.08

3.2.2 Broad Analysis of Inert Testing Data

The da/dt vs K_j in Figure 13 show that even though no crack growth should be occurring below the K_{1C} there is evidence of changing electrical resistance behavior in the dry N₂ environment. There are two important observations (1) all plots demonstrate the same changes of slope at roughly the same K_j , 45 and 65 MPaVm, and (2) the apparent da/dt for a given K increases with increasing dK/dt . The curves were divided into three regimes based on the slope of the da/dt curve. Regime I is the low K_j , Regime II is the intermediate K_j , and Regime III is high K_j . The cause of each regime must be identified to determine the exact nature of the induced

error. The nature of this error is proposed to be either due to local crack tip plasticity, bulk plastic behavior, ductile tearing, or a combination of these mechanisms. For this material, Regime I behavior has been previously connected with localized crack tip plasticity [4], which will be expanded upon later in the analysis. The initial change in slope at $K_I \approx 45 \text{ MPa}\sqrt{\text{m}}$ is not a newly noted phenomenon. Inert testing by Gangloff et al. noted a similar change in slope and speculated that the effect was due to subcritical crack growth [4]. Prior analysis does not sufficiently describe the observed behavior.

This work seeks to identify the behavior measured by the dcPD system in an inert environment and the responsible physical phenomena, such that they can be quantifiably removed or accounted for in the environmental data. The material behavior was evaluated using elastic-plastic fracture mechanics analysis and non-fracture mechanics based bulk ligament plasticity analysis, then compared to the features on the fracture surface and recorded experimental data.

3.2.3 Identify the phenomena responsible for of the da/dt vs K curve regions

The goal is to correlate the inert SENT behavior with established phenomena that have historically been used as thresholds for mechanical behavior.

3.2.3.1 Bulk Analysis

3.2.3.1.1 Plane Strain Limit Load Analysis

The fracture mechanics behavior of Monel K-500 is first evaluated using an elastic-plastic analysis. The importance of the J integral for plastic contributions in the applied stress intensity has been previously discussed in the Experimental Methods. The limit load, P_0 , is a metric that can be used to quantify the stress at which the bulk ligament is strongly influenced by plastic behavior due to the expansion of the plastic zone in a cracked sample. The plane strain criteria accounts for the constraint assumed by the sample geometry [70]. Equation 9 defines P_0 for plane strain in an SEN(T) type sample [70]. P_0 was compared to the apparent crack length and applied load for all dK/dt . Figure 15 depicts the technique used to determine if P_0 was a factor in the material behavior. As shown by $dK/dt = 4.0 \text{ MPa}\sqrt{\text{m}}/\text{hr}$, the applied loads are in all cases below the P_0 during the test; this holds true for all dK/dt tested. As such, it is not expected that

the crack tip plasticity will drastically influence the remaining ligament plastic behavior. This elastic-plastic criteria does not adequately describe the changes in electrical resistance.

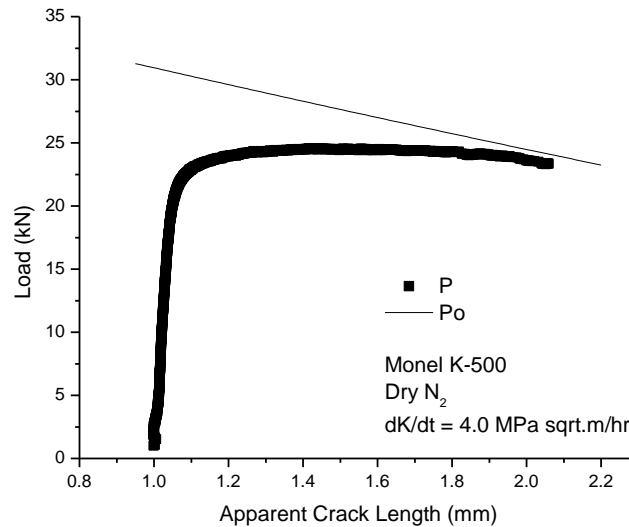


Figure 15: Comparison of the limit load, P_o , and the applied load with apparent crack length of $dK/dt = 4.0 \text{ MPa}\sqrt{\text{m/hr}}$ in dry N_2 .

3.2.3.1.2: Bulk Plasticity Analysis

The plastic behavior of the bulk ligament is now considered without crack tip effects. Quantifying the stresses pertinent to the plastic behavior of Monel K-500 are essential for interpreting the apparent da/dt curves. The compressive mechanical behavior of Monel K-500 is shown in Figure 16. Bulk isotropy can be assumed for Monel K-500, because this material lot is polycrystalline, no texture, equiaxed grains, and an average grain size of $11.2 \mu\text{m}$ which is significantly smaller than the SENT cross-section [38].

Monel K-500 displays a standard stress-strain curve for alloys. The yield stress and the proportional limit are considered for analysis. The proportional limit is the stress at which the stress-strain curve first deviates from purely elastic linearity, indicating the initiation of plasticity [74]. To quantify the stress of the proportional limit the compression stress-strain curve the slope, E , was recorded between increment data points. Then the change in that slope with relation to stress ($dE = \Delta E / \Delta \sigma$) was calculated and displayed in Figure 17. During purely linear-elastic behavior dE is near zero, deviation from linear-elastic behavior is identifiable by deviation from zero. The proportional limit was quantified as the stress at which dE falls and remains below -5 . The yield stress was calculated using the traditional 0.2% offset method is used to determine

the start of bulk plastic deformation. Using these techniques the yield strength and proportional limit were found to be 910 MPa and 620 MPa, respectively.

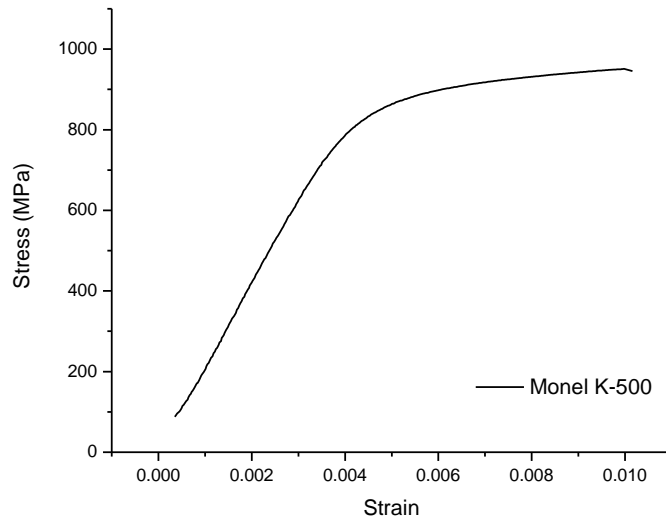


Figure 16: Compression stress-strain curve for Monel K-500.

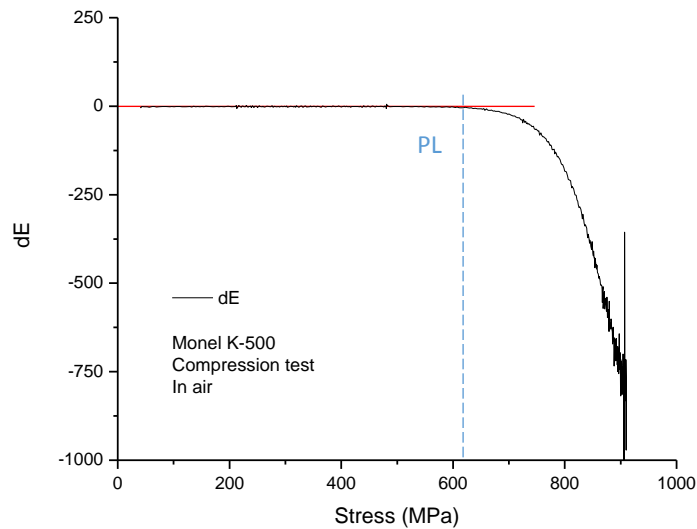


Figure 17: A curve showing the derivative of the slope between incremented points on the compressive stress-strain curve. Deviation from zero was used to define the proportional limit.

Bulk scale plasticity generates electrical resistance; however, it has not been rigorously analyzed over the full span of elastic-plastic behavior. To quantify the relationship between electrical resistance and load for Monel K-500, a dog bone tensile sample was outfitted with dcPD

monitoring system and loaded at a constant displacement rate until failure. Proportional limit and the yield strength, as determined by the compression test, were compared to the tensile test data to identify pertinent correlations. The load-displacement and load-voltage data from the tensile test are shown in Figure 18. In Figure 18 load (a) corresponds to the proportional limit and load (b) is the yield stress.

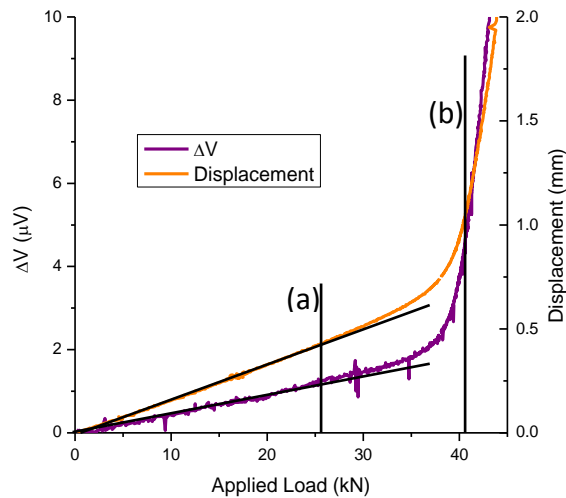


Figure 18: The change in measured dcPD voltage and actuator displacement with applied load of a Monel K-500 smooth dog bone tensile test. The proportional limit (a) and the yield stress (b) are labeled.

The linear region in ΔV and displacement prior to the proportional limit is hypothesized to be due to the elastic deformation of the sample due to tensile loading because no plastic behavior is expected to occur below this stress. Electrical resistance can change either through materials or by change in the dimensions of the examined volume (Equation 10). Plastic effects dominate by increasing the resistivity. An elastic strain effect on resistivity has been noted in some alloy systems, but prior work shows the effect to be negligible for Monel K-500 [75]. Thus, elastic influences are limited to the change in dimension of the examined area. ΔV was calculated by incorporating the elastic change in dimensions due to stress through Poisson's ratio in Equation 10. The calculated ΔV and the experimentally measured ΔV are compared in Figure 19.

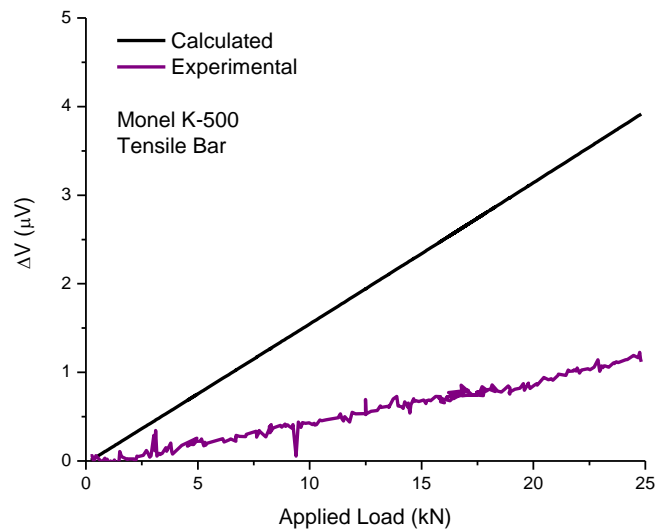


Figure 19: Experimentally recorded ΔV compared to the ΔV calculated based on elastic dimension change with stress for the Monel K-500 dog bone tensile bar

There is a large discrepancy between the calculated ΔV and the experimental value over the full range of applied load prior to the proportional limit. This suggests that there is an additional effect occurring that is not adequately described by the incorporation of the standard elastic stress-strain response to Equation 10.

When normalized by the volume of the examined area, the experimental voltage change of the tensile bar was significantly less than the SENT type samples at the proportional limit. The values are listed in Table 7. This suggests that the elastic contractions are not governing the voltage change in the SENT samples. Rather the elevated electrical resistance effect is expected in the SENT samples due to the increasing size of the crack tip plastic zone. This supports the hypothesized mechanism of the resolution limit.

Table 7: The experimentally recorded ΔV for all dry N2 SENT tests compared to the tensile bar of Monel K-500

Test Description	ΔV at the proportional limit (μV)	ΔV normalized by volume ($\mu V/mm^3$)
Tensile Bar	1.18	0.029
dK/dt (MPa \sqrt{m} /hr)		
0.1	3.97	0.150
0.33	3.71	0.117

1	3.28	0.122
2	2.35	0.077
3	3.99	0.139
4	4.79	0.132

At the proportional limit, deviation from elastic linearity occurs in the load-displacement and the load-voltage curves. By the yield load linearity is re-established, though at a steeper slope. The slope for both curves changes dramatically between the proportional limit and the yield stress. With no other changing stimuli, the electrical resistance is shown to be directly dependent on the mechanical stress in the remaining ligament.

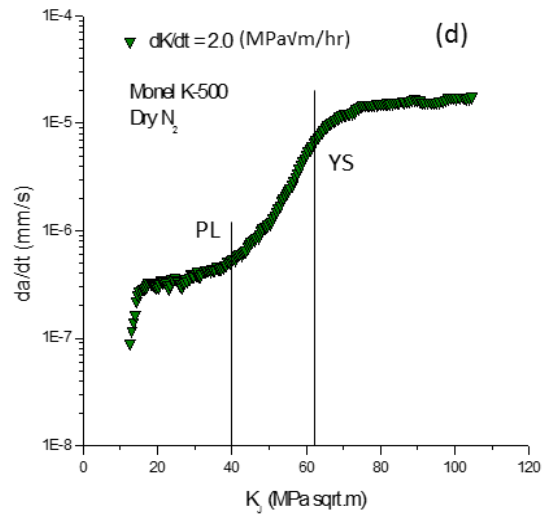
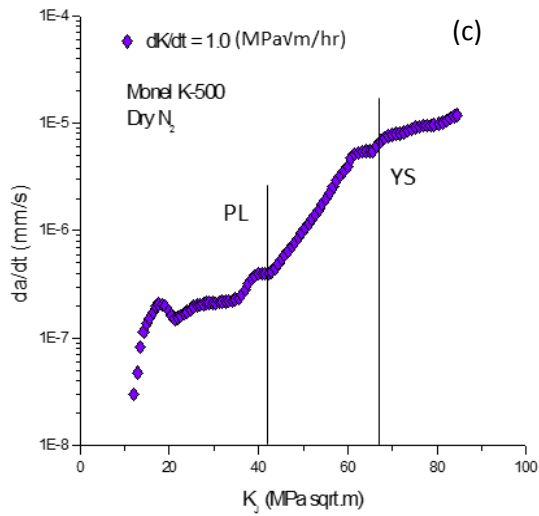
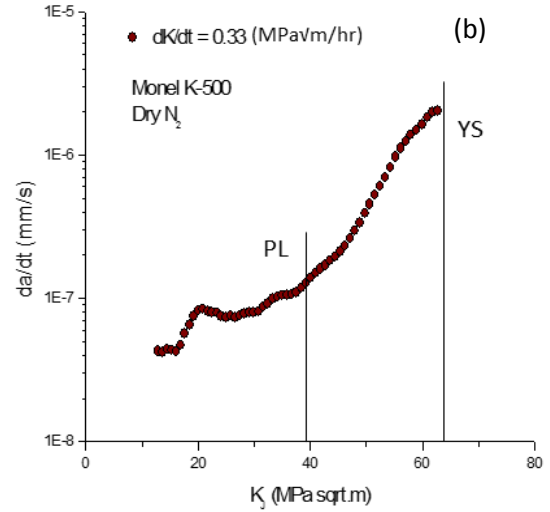
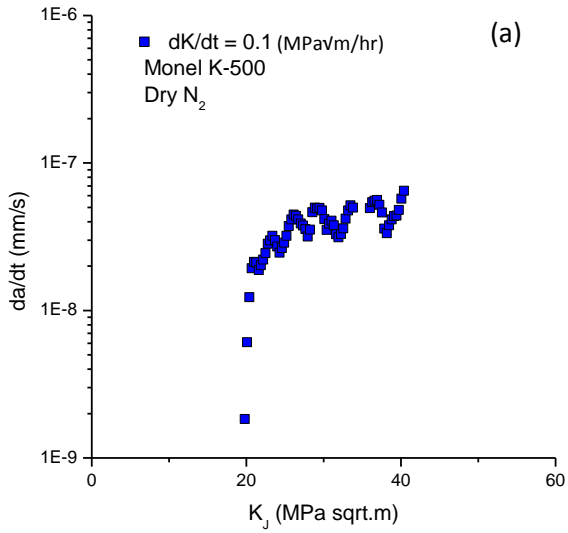
To correlate the bulk ligament behavior observed in the tensile bar to the SENT samples the K_I associated with the original crack length and the proportional limit and the yield strength were determined for each environmental dK/dt and are displayed in Table 8. The stresses were calculated using the applied load data and the remaining ligament area, assuming no crack growth had occurred. This assumption was used to calculate a conservatively large K_I value. The maximum possible crack growth calculated by the dcPD system up to the yield strength is <100 μm , a maximum of 1% of the remaining ligament after the precrack. The difference in K_I between the stresses using the assumption of no crack growth and using the dcPD calculated crack length is 1%. This value is sufficiently small as to not change the data interpretation.

The $dK/dt = 0.1 \text{ MPa}\sqrt{\text{m/hr}}$ test did not exceed the proportional limit and the $dK/dt = 0.33$ and $3.0 \text{ MPa}\sqrt{\text{m/hr}}$ test did not exceed the yield strength. The apparent da/dt vs K_I for all inert tests are plotted individually in Figure 20 with lines corresponding to the K_I metrics, with PL and YS designating the proportional limit and yield strength, respectively.

Table 8: The K_I associated with the proportional limit and yield strength for each dK/dt dry N_2 test.

dK/dt (MPa$\sqrt{\text{m/hr}}$)	$K_{\text{Proportional Limit}}$ (MPa$\sqrt{\text{m}}$)	$K_{\text{Yield Strength}}$ (MPa$\sqrt{\text{m}}$)
0.1	_____	_____
0.33	39.5	65.1
1.0	42.1	67.2
2.0	39.5	62.3

3.0	40.6	_____
4.0	40.1	65.8



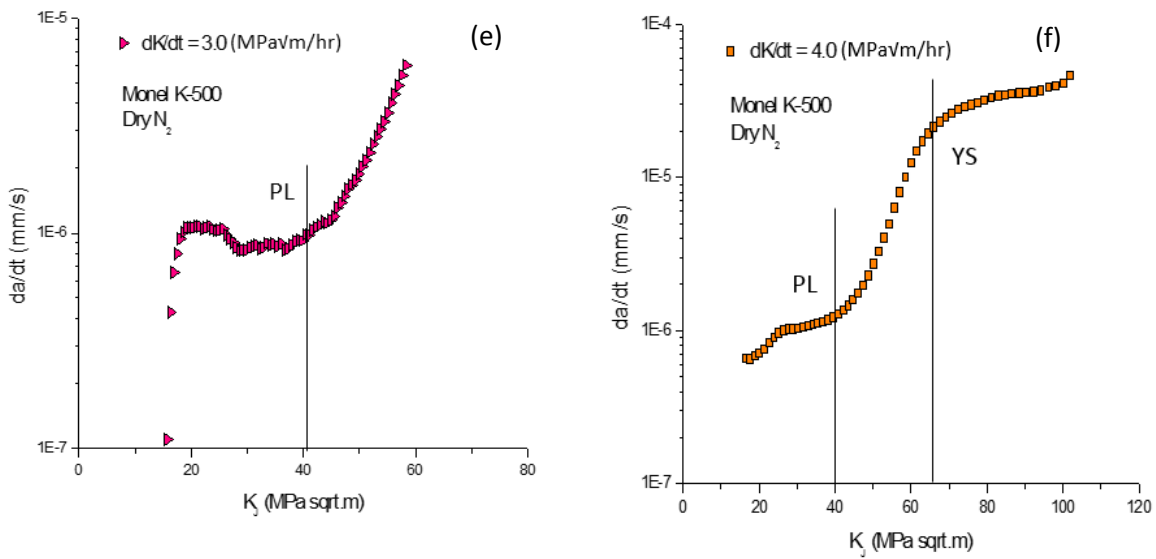


Figure 20: The K_I of the proportional limit (PL) and yield strength (YS) are labeled for each dK/dt , Monel K-500 dry N_2 test.

In each case the calculated proportional limit and yield strength are well aligned with the changes in slope on the da/dt vs K_I for all dK/dt . It appears that the bulk plastic behavior incites the changes in slope observed in the dcPD data. However, the dcPD signal must be correlated to the fracture surface to determine the nature of the electrical resistance change. If no crack growth is evident then the electrical resistance is due solely to an increase in resistivity by increasing dislocation density. If there is a notable change in the fractographic behavior then this real crack extension (whether IG or ductile) must be considered as a source of electrical resistance.

3.2.3.1.3 da/dt vs K curve comparison to fractography

The changes in slope in da/dt vs K_I have been related to bulk plastic behavior which has been shown to generate a quantifiable change in electrical resistance. Previous work has hypothesized that the change in slope, now correlated with the proportional limit, correlated with a region of ductile crack extension at the high-constraint center of the specimen [4]. In light of the correlations observed in Figure 20, additional investigation of this hypothesis is required. Though crack growth is not expected to occur below the K_{Ic} , the fracture behavior for several of the inert SENT tests was recorded. Tests were interrupted at incremental K and post-test fatigue

was employed to encapsulate the test fractography between two transgranular morphology regions. Their fracture surfaces were examined using the secondary mode in the SEM.

3.2.3.1.4 Fractography below the yield strength

A test at a $dK/dt = 3.0 \text{ MPa}\sqrt{\text{m/hr}}$ in dry N_2 , was interrupted at $K_I = 61 \text{ MPa}\sqrt{\text{m}}$, after the proportional limit, but prior to the yield strength. A macroscopic view of the fracture surface is shown in Figure 14, and a higher magnification micrograph of the test area is shown in Figure 21. Fracture occurs from bottom to top in Figure 21, progressing from a TG fatigue precrack to a $42 \mu\text{m}$ wide TG ductile fracture region and finally TG post-test fatigue.

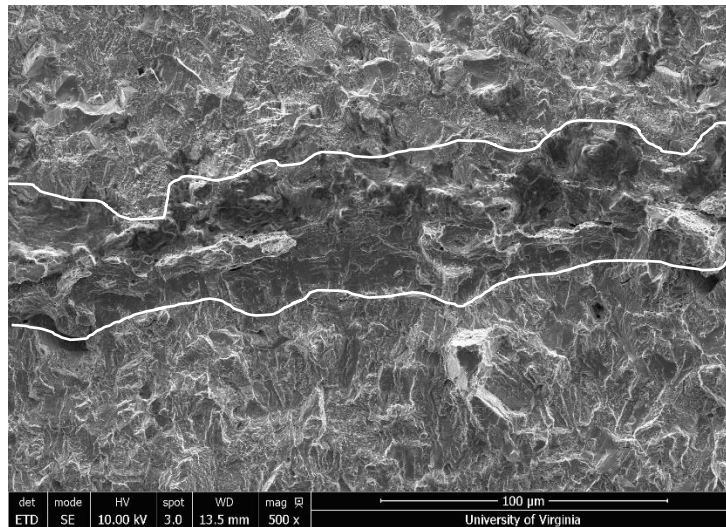


Figure 21: The fracture surface of Monel K-500 $dK/dt = 3.0 \text{ MPa}\sqrt{\text{m/hr}}$ focusing on the region that occurred during the test.

The ductile TG region on the fracture surface indicates that the dcPD signal increase after the proportional limit is not purely plastic, but that there is some crack extension involved. However this behavior is distinct from the crack advance observed in prior work in that it is much smaller and scale homogeneously distributed along the crack front rather than focused at the center of the specimen. Critically, this advance can likely be attributed to crack tip blunting; the advance of which can be estimated by the crack mouth opening displacement (CTOD), shown in Equation 12. Where a $K_I = 61 \text{ MPa}\sqrt{\text{m}}$, yield strength (σ_{YS}) of 910 MPa , and modulus (E) of 188 GPa the LFM calculate CTOD is $27 \mu\text{m}$ which is reasonably well aligned with the observed region on the

fracture surface. The dcPD calculated crack length (72 μm) is 30 μm larger than the measured crack length, suggesting that this blunting is likely augmented by a role of crack tip/bulk plasticity.

$$CTOD = \frac{4K^2}{\pi E \sigma_{YS}} \quad \text{Equation 12}$$

3.2.3.1.5 Fractography above the yield strength

Two inert tests, $dK/dt = 1.0$ and $2.0 \text{ MPa}\sqrt{\text{m/hr}}$, were interrupted at high K_I , 98 and 115 $\text{MPa}\sqrt{\text{m}}$, respectively, that surpassed the yield stress. The fracture surfaces are displayed in Figure 14. The slip-band transgranular nature of the fatigue precrack and the post-test fatigue are separated by a band of ductile transgranular failure. These fractographic features are distinctive such that transitions are easily identifiable. This is indicative of a reduction in remaining ligament area during the test, increasing electrical resistance. The ductile tearing behavior is not limited to the triangular region noted in prior work, it extends across the sample thickness, as can be seen on the fracture surfaces [4]. The ductile regions are measured to be 0.75 and 0.95 mm across for $dK/dt = 1.0$ and $2.0 \text{ MPa}\sqrt{\text{m/hr}}$, respectively.

The reduction in cross-sectional area due to net-section yield and ductile tearing is a large contribution to the da/dt vs K behavior in Regime III. While this is an interesting topic, the ductile tearing mechanism for this material system is beyond the scope of this work. The percent difference in crack length is still shown to increase with increasing end K_I , from 5.2% at $K_{I,\text{end}} = 98 \text{ MPa}\sqrt{\text{m}}$ ($dK/dt = 1.0 \text{ MPa}\sqrt{\text{m/hr}}$) to 13.9% at $K_{I,\text{end}} = 115 \text{ MPa}\sqrt{\text{m}}$ ($dK/dt = 2.0 \text{ MPa}\sqrt{\text{m/hr}}$). The 300 μm difference between the dcPD calculated crack length and the area observed suggests that in addition to the ductile crack advance that the bulk plasticity contributes significantly to the total electrical resistance of the sample. This analysis shows that after the yield strength, the change in electrical resistance is due to a combined effect of reduction in cross-sectional area, ductile crack advance, and bulk ligament plasticity. It should be noted that the ductile tearing is only noticeable because post-test fatigue was employed; however, most environmental tests were not subjected to this additional technique.

3.2.3.1.6 Comparison to environmental data

Now that mechanisms for dcPD error have been established in inert testing, the environmental testing must be evaluated to determine if it suffers from the same phenomena.

The da/dt vs K_I data for the inert and environmental $dK/dt = 1.0$ MPa \sqrt{m}/hr test are shown in Figure 22. The data sets coincide at both low and high K_I , $K_I = 20$ and 60 MPa \sqrt{m} , respectively. The coincidence at low K is used to determine the start of cracking by using the inert test as a lower crack growth resolution limit. The high K_I coincidence has not been previously noted and further suggest that the high K_I behavior is not environmentally dependent and/or is obfuscated by the complications (e.g. blunting, tearing, and plasticity) detailed in the previous sections.

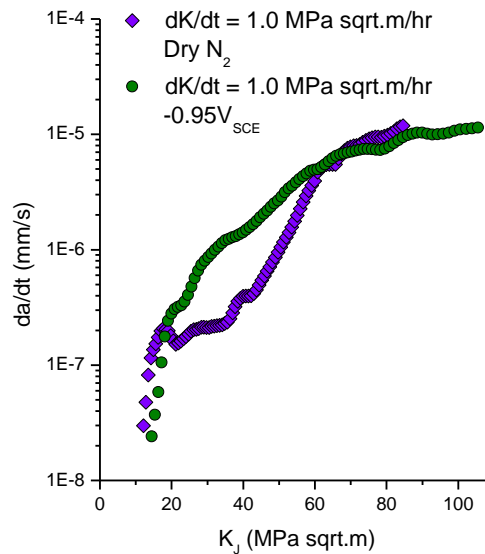


Figure 22: Apparent crack growth data for $dK/dt = 1.0$ MPa \sqrt{m}/hr in 0.6M NaCl EA = $-0.950V_{SCE}$ and dry N_2 .

The coincidence of both plots at high K_I suggests that both tests are experiencing the same electrical resistance phenomenon in Regime III. It has been established that ductile tearing occurs during inert tests at high K_I by bounding the fracture surface with post-test fatigue. The ductile tearing fractography is indistinguishable from the final failure morphology that occurs on all samples. It is plausible that ductile tearing could occur during the environmental tests and not be measurable on the fracture surface. The post-test fatigue protocol, that clearly delineates the experimental regions, was not routinely applied to environmental tests. It was assumed that all fracture that occurred in environment was intergranular and therefore, easily measured. Quantifying an incorrect amount of crack extension would contribute to the error between the

dcPD calculation and the true crack length. It is likely that environmental tests are experiencing a combination of ductile tearing and bulk scale plasticity at high K_I , akin to the inert tests.

One environmental test, $dK/dt = 3.0 \text{ MPa}\sqrt{\text{m/hr}}$, was interrupted at $K_I = 74 \text{ MPa}\sqrt{\text{m}}$ and post-test fatigue was performed on the sample. The remaining ligament, assuming the dcPD interpretation of crack growth was correct as a conservative estimate, did surpass the yield strength. The fracture surface of the $dK/dt = 3.0 \text{ MPa}\sqrt{\text{m/hr}}$ environmental test is displayed in Figure 23. Region (a) is the TG precrack, (b) is the IG-SCC, (c) is a ductile morphology indicative of a stretch zone, (d) is the TG post-test fatigue, and (e) is the final failure of the sample. The test was halted soon after the yield load was reached so a complete ductile failure region adjacent to the IG-SCC was not formed. The dcPD interpreted SCC final crack length of 1.51 mm lies between the end of IG-SCC, 1.39 mm, and the stretch zone crack length, 1.67 mm. This length inconsistency suggests that the length of the stretch zone on the fracture surface does not accurately describe the crack length at the end of the test.

The preceding sections have clearly demonstrated that for high K_I values that ductile tearing, and bulk plasticity can compromise the accuracy of the dcPD signal. While the exact origin of these phenomenon are alluded to here, a full mechanistic description of this behavior is outside of the scope of the current study (but continuing in companion research). Critically, the current efforts serve to identify the bounds outside of which the dcPD data begin to show inaccuracies, thus establish a functional protocol for accurate data generation.

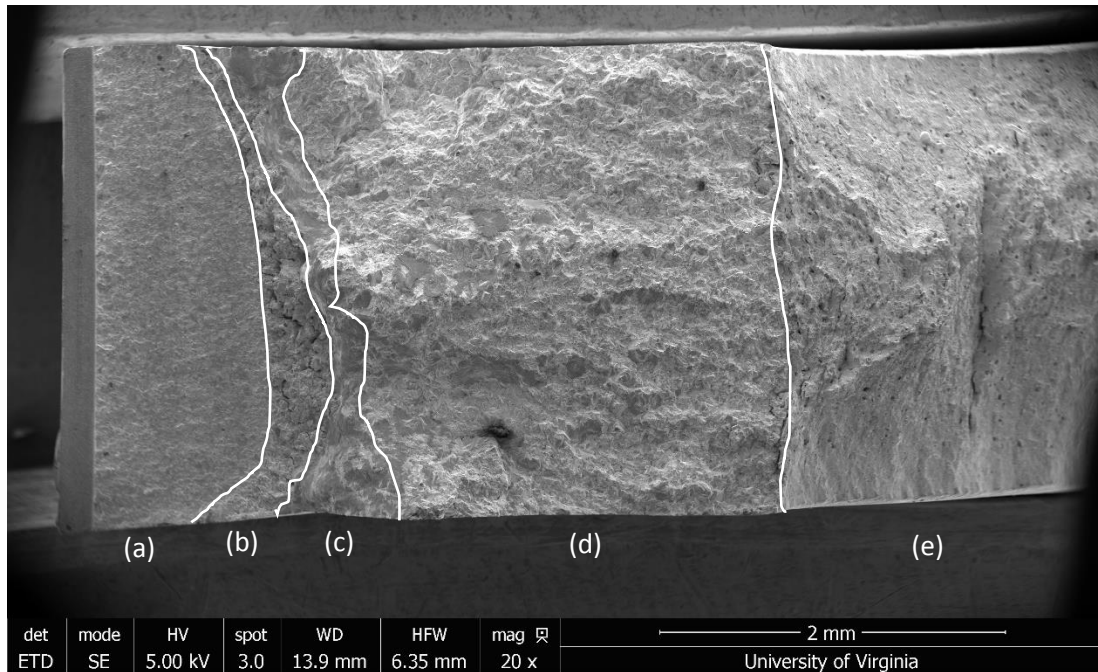


Figure 23: The full fracture surface for Monel K-500 in 0.6M NaCl, $-0.950V_{SCE}$, $dK/dt = 3.0 \text{ MPam/hr}$. Crack growth occurred from left to right. (a) is TG fatigue, (b) is IG-SCC, (c) is the stretch zone, (d) is TG post-test fatigue, and (e) is ductile failure.

3.2.3.1.7 Error Mitigation Procedure

Ductile tearing is not considered to be representative of the environmental cracking behavior of Monel K-500, and as such is not considered useful to the goals of this dK/dt dependent analysis. The large error in the environmental cracking data occurs only at high K_I and is predominately a combination of ductile tearing and bulk scale plasticity. After the proportional limit, the material can no longer be considered to be operating in the bulk LEFM regime. To avoid including these erroneous effects the crack growth data is truncated at the proportional limit, prior to which no bulk scale plasticity occurs. This data limitation will be considered for future specimen design. Increasing the precrack length or adjusting the sample cross-section can increase the K_I at which the proportional limit occurs.

3.2.3.2 Localized Crack Tip Plasticity

While the majority of the error can be removed by completely eliminating the data at K_I values above which the proportional limit is exceeded, there is still localized plasticity-based error in the low K_I regime [27]. The data for all inert SENT testing prior to the proportional limit is shown in Figure 24. Each da/dt vs K_I data set was fit with an exponential equation, displayed in Equation

13, such that the value of the exponential coefficient, z , was the same and the scaling trend could be seen in the coefficients. The z term defines the slope of an exponential equation on a semi-log plot. The C -values are plotted versus the dK/dt in Figure 25, the direct linear relationship between these values confirms the hypothesis made by Gangloff et al. that the resolution limit can be determined for any dK/dt based on a single inert da/dt vs K curve [4]. Specifically, that the plastic zone size is a function of the K value, independent of the dK/dt , thus the local plasticity induced growth rates should directly scale with loading rate. This is captured functionally by the equation listed in Figure 24 thus is available for any future efforts at variable dK/dt .

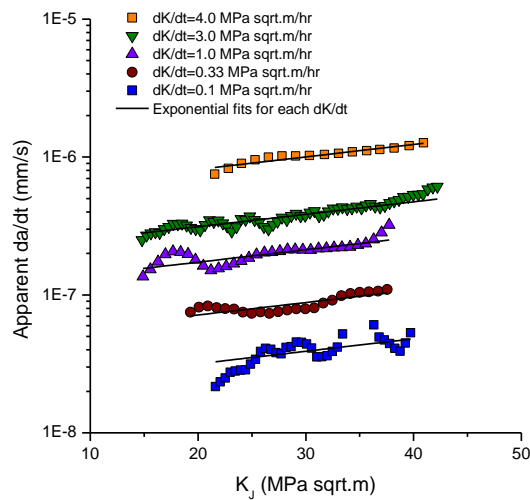


Figure 24: The data for Monel K-500 at fixed dK/dt tested in dry N_2 , cropped at the proportional limit, each with the exponential fit at a fixed z value.

$$\frac{da}{dt_{RL}} = C e^{z \cdot K} \quad \text{Equation 13}$$

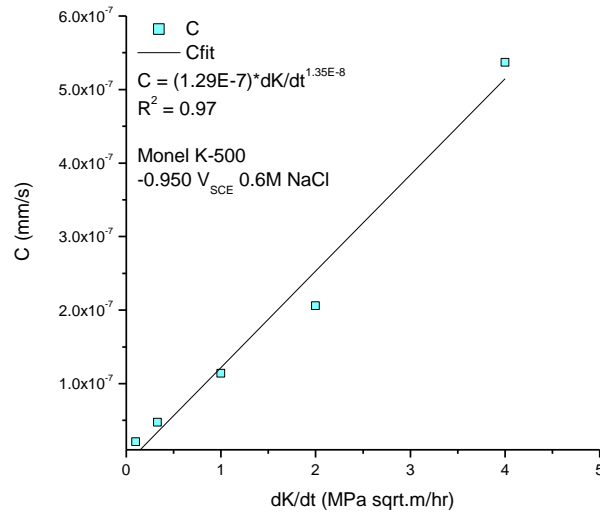


Figure 25: The resolution limit coefficient fit value (C) for each dK/dt in dry N₂. The data has a linear fit.

Crack growth and crack tip plasticity occur concurrently during the environmental cracking process. Therefore their contributions to the electrical resistance must be separate and additive. Prior efforts have simply reported the plasticity induced value as the functional resolution limit below which cracking kinetics cannot be differentiated. However, this approach only partially addresses the issue since the contribution of crack tip plasticity during crack progression remains. As such a more rigorous approach is proposed where the plasticity induced contributions are subtracted from the total da/dt values measured at each K value. This approach is applied in this study; functionally, Equation 14 represents the general equation. A graphical representation of the effect of removing the resolution limit is shown in Figure 26. In Figure 26(a) the environmental data with the shorting and bulk-plasticity correction for dK/dt = 0.15 MPa√m/hr is shown with its corresponding resolution limit. Figure 26(b) shows the environmental data with the resolution limit subtracted out using Equation 4. The largest data shift is at low K_I where the cracking threshold is determined. At high K_I there is almost an order of magnitude separation between the environmental data and the resolution limit thus there is little effect of removing the plasticity contribution.

$$\frac{da}{dt}(K_j)_{\text{crack growth}} = \frac{da}{dt}(K_j)_{\text{experiment}} - \frac{da}{dt}(K_j)_{\text{RL}}$$

Equation 14

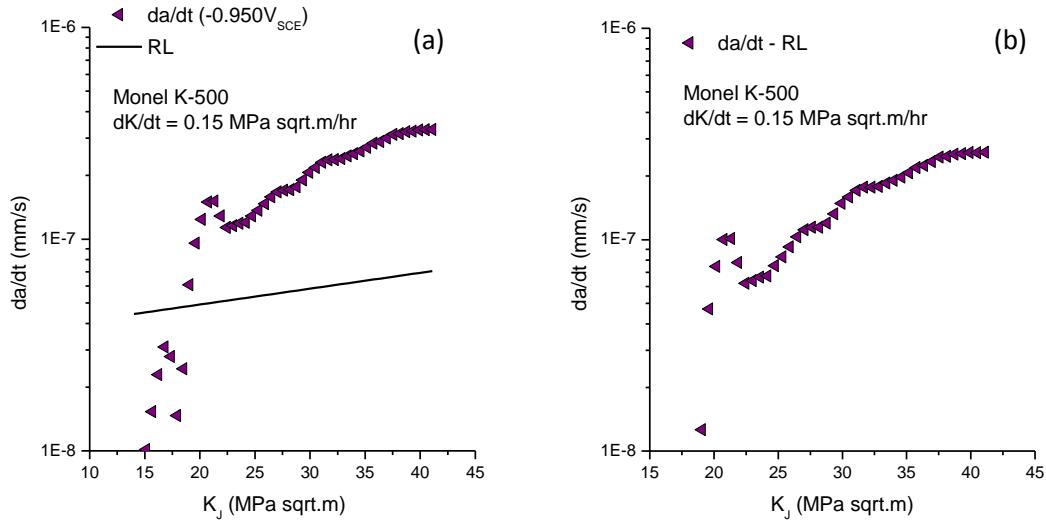


Figure 26: Graphically displaying the effect of removing the resolution limit from the environmental crack growth data for Monel K-500 at $dK/dt = 0.15 \text{ MPa}\sqrt{\text{m/hr}}$, $-0.950V_{\text{SCE}}$

Using the corrective procedures justified above (truncating the data at the proportional limit and subtracting out the resolution limit) effectively decouples the non-environmental cracking, localized and bulk ligament plastic behavior from the environmental crack growth data to produce the curves shown in Figure 27. The data set presented in Figure 27 will be analyzed in Task 2 to quantify the loading rate effects on the environmental crack growth behavior of Monel K-500.

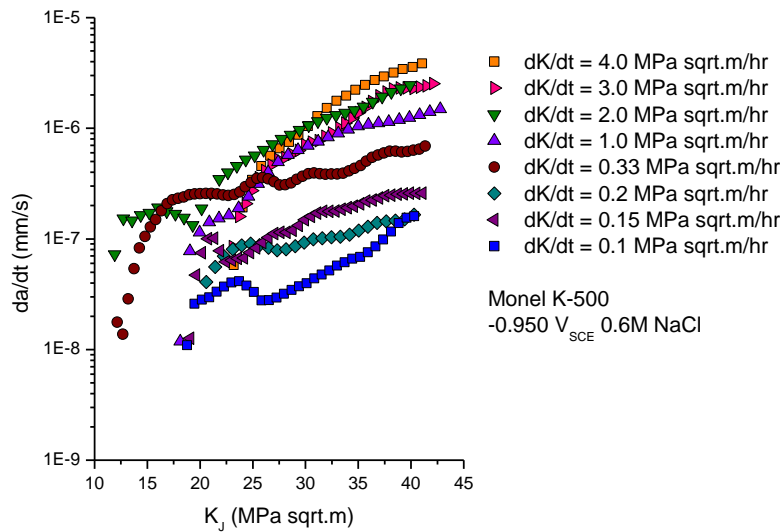


Figure 27: Full environmental data set for Monel K-500 with corrections for shorting, truncation at the proportional limit, and with localized crack tip plasticity removed.

3.2.4 Corrections applied to MP98t environmental data

The testing procedures for MP98t were conducted in the same manner as the Monel K-500 tests with only an adjustment to the environmental conditions. The effect of dK/dt on MP98t was examined in immersed 0.6M NaCl solution polarized to $-1.30 V_{SCE}$ at $dK/dt = 0.2, 0.33, 1.0,$ and 2.0 MPa \sqrt{m}/hr . The resolution limit was determined from a SENT test in dry N_2 at $dK/dt = 1.0$ MPa \sqrt{m}/hr . A compression test in same orientation as the tensile testing direction was conducted to determine the proportional limit and the yield stress, 900 and 1470 MPa, respectively.

The data fidelity procedures developed for Monel K-500 in Task 1 were applied to MP98t due to similarities in the inert material behavior. MP98t displays the same change in slope behavior of da/dt vs K near the proportional limit, $K = 56.2$ MPa \sqrt{m} , as Monel K-500, as shown in Figure 28. This mutual behavior supports the truncation of MP98t data sets at the proportional limit, to prevent the inclusion of bulk scale plastic behavior in the crack growth analysis. The mechanics of linear scaling of the resolution limit hold true for elastic-plastic materials. The linear scaling and subtraction of the resolution limit was utilized to decouple crack tip plasticity from environmental crack growth data. The resolution limit for $dK/dt = 1.0$ MPa \sqrt{m}/hr is labeled in Figure 28.

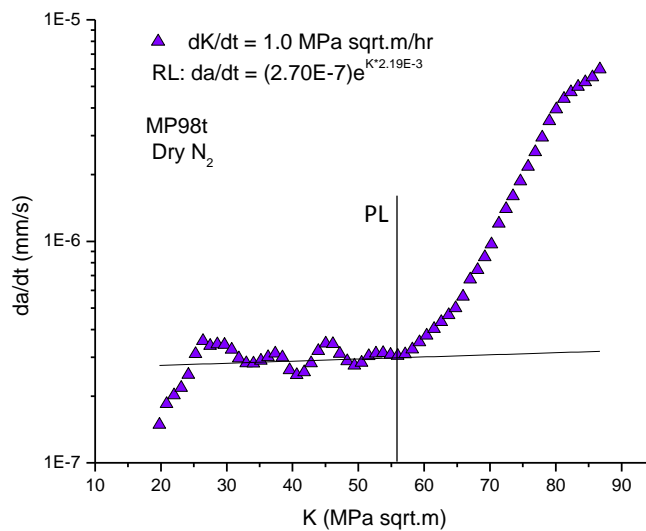


Figure 28: Dry N2 curve for MP98t, $dK/dt = 1.0 \text{ MPa}\sqrt{\text{m/hr}}$, dry N₂. The equation for the resolution limit (RL) is shown in the legend.

Interpreting the fracture behavior of MP98t was nontrivial. Over the course of all environmental tests the fracture surface moves out of the Mode I plane by deflection. The entire Mode I plane for all samples was transgranular, including the precrack region. The fatigue precrack procedure for all samples was designed to end at 1 mm. The Mode I fracture surfaces for all environmental tests are shown in Figure 29. The only predominate feature on the fracture surface is the crack deflection (of note after crack deflection the fracture morphology was intergranular which suggested an important role of property anisotropy and grain directionality). The crack lengths at deflection are listed in Table 9. The crack length of deflection is sufficiently longer than the intended 1 mm to rule out immediate crack deflection. As such, MP98t shows no distinguishable transition between the fatigue precrack and the environmental cracking; specifically there is a transgranular morphology for both. For MP98t data analysis the precrack length is assumed to be 1 mm in all cases. With two invalidating dcPD factors noted, crack deflection and the proportional limit, the lowest K occurring factor is the limiting value for each test. The values for crack length and K for each limitation per dK/dt are displayed in Table 9. At low dK/dt , 0.2 and 0.33 $\text{MPa}\sqrt{\text{m/hr}}$, the deflection is the limiting criteria; for high dK/dt , the proportional limit (PL) is limiting. Each data set was truncated at the limiting K value prior to analysis. Figure 30 displays the complete MP98t data set for testing at $-1.30V_{\text{SCE}}$ with all correction adjustments made.

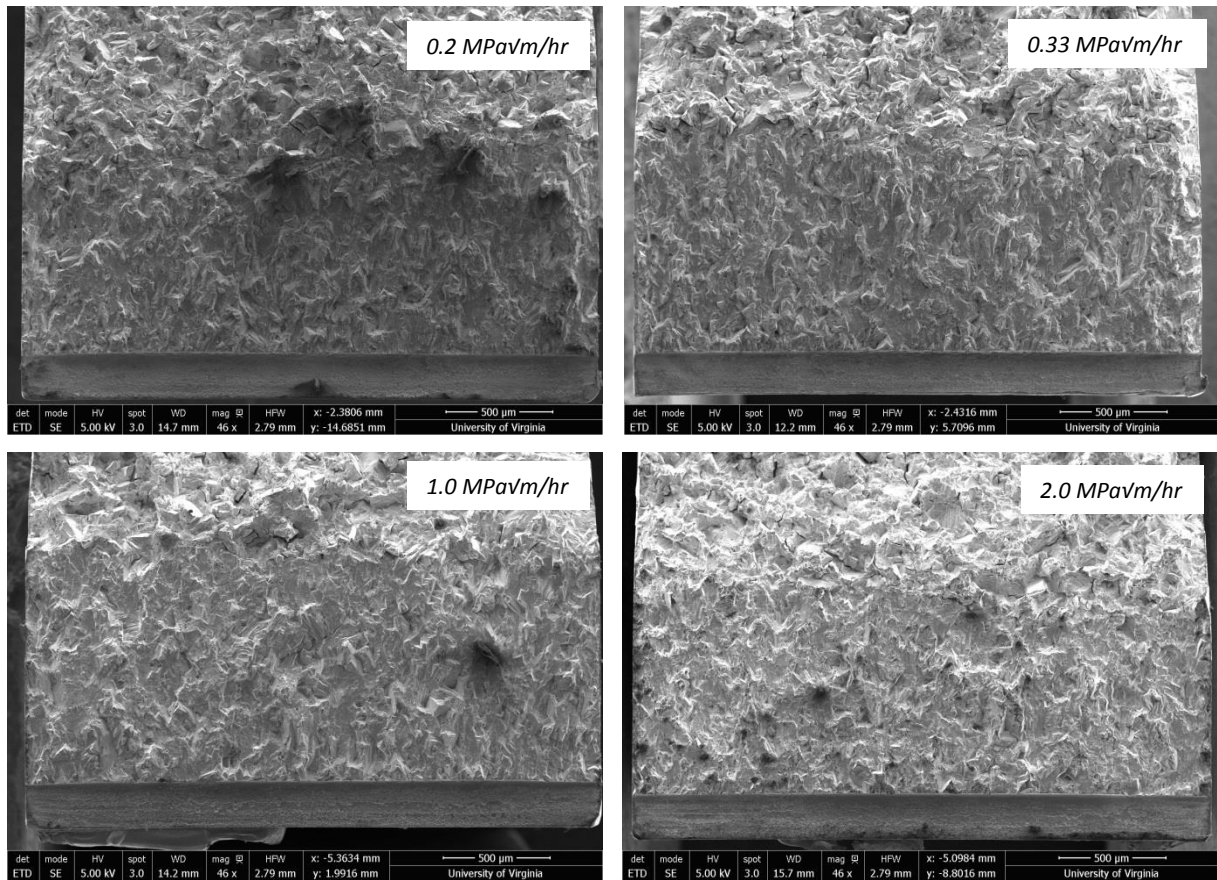


Figure 29: The Mode I environmental fracture surfaces of MP98t. The crack propagated from bottom to top.

Table 9: Proportional limit and crack length deflection information for each environmental dK/dt tested for MP98t

dK/dt (MPavm/hr)	a of deflection (mm)	a of PL (mm)	K of deflection (MPavm)	K PL (MPavm)
0.2	1.26	1.61	55.6	67.9
0.33	1.35	1.56	59.9	66.9
1	1.31	1.140	71.1	57.9
2	1.17	1.135	61.5	57.8

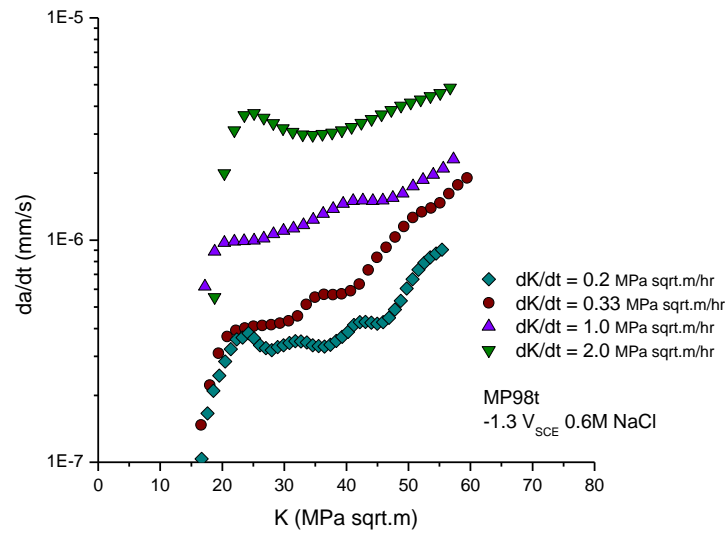


Figure 30: Crack growth rate vs K data for MP98t with corrections made for shorting, localized crack tip plasticity, crack deflection, and truncation at the proportional limit.

3.3 Task 2: Quantify the effect of dK/dt on the standard LEFM metrics K_{TH} and da/dt_{end} for Monel K-500 at relevant electrochemical polarization

3.3.1 IG-SCC Susceptibility Metrics

The loading rate effects on the environmental crack growth behavior were analyzed using historical metrics and fractographic examination. The SCC susceptibility of a material has been quantified by the stress intensity threshold (K_{TH}) and stage II crack growth rate (da/dt_{II}). The determination method of these metrics is shown in Figure 31. The K_{TH} , the K at which crack growth begins, is defined in this work as the first positive data point after the resolution limit has been removed. da/dt_{II} , by its definition, could not be determined because no data set reached a K -independent crack growth rate; instead, da/dt_{end} is used. da/dt_{end} is quantified as the last data point prior to the proportional limit. The data across dK/dt for K_{TH} and da/dt_{end} are shown in Figure 32 and 33, respectively.

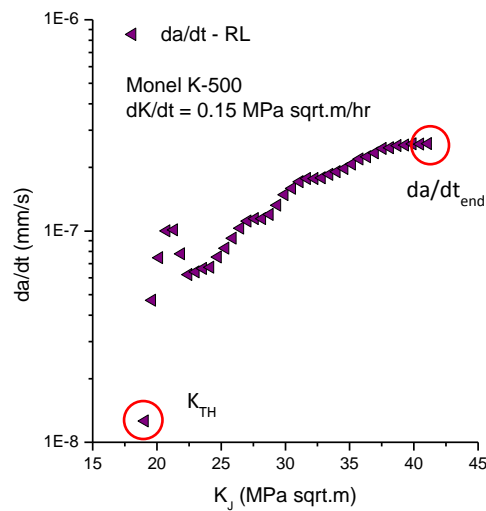


Figure 31: Corrected data set for $dK/dt = 0.15$ MPa \sqrt{m} /hr with the illustrated locations of da/dt_{II} and K_{TH} .

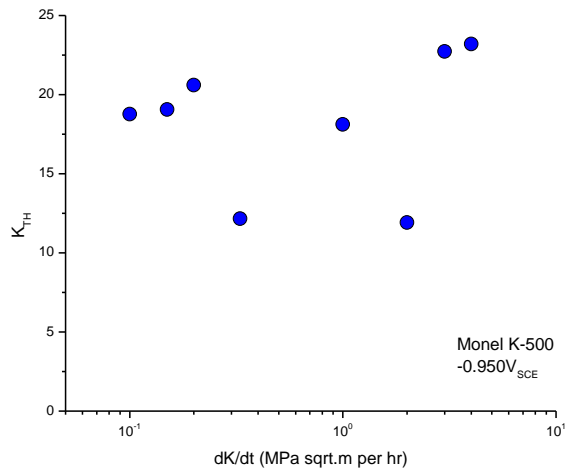


Figure 32: The K_{TH} compared to dK/dt for Monel K-500 at 0.6M NaCl with -0.950V_{SCE}

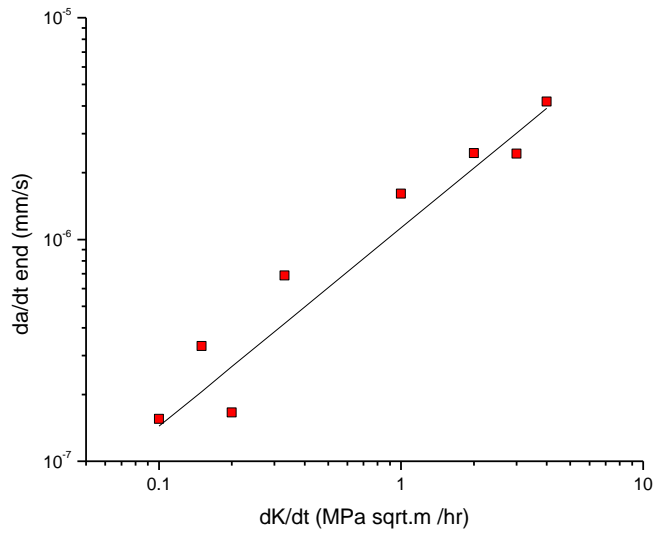


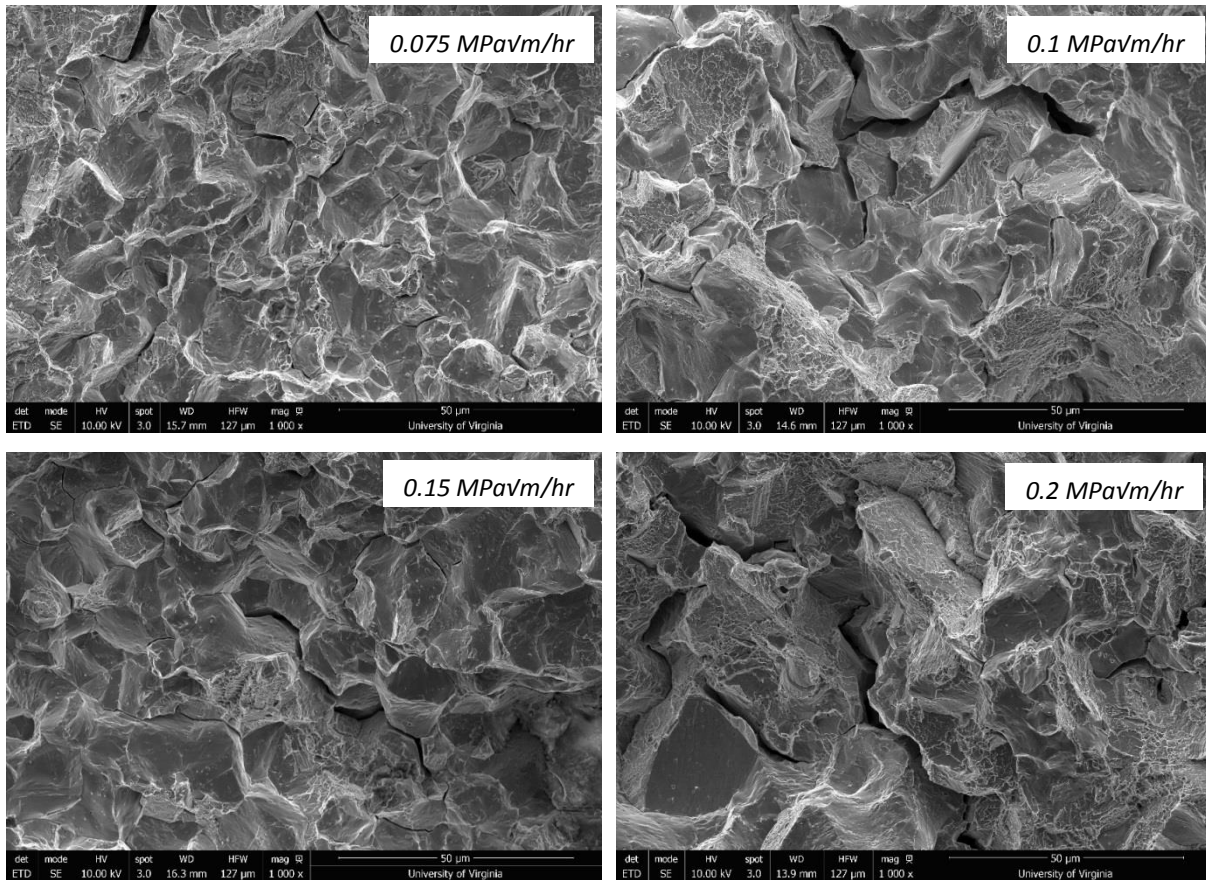
Figure 33: da/dt_{end} compared to dK/dt for Monel K-500 at 0.6M NaCl with -0.950V_{SCE}

K_{TH} ranges from 11.9 to 23.2 MPa√m for Monel K-500 in a low susceptibility environment does not show any systematic trends with loading rate. da/dt_{end}, however, does display a visible trend behavior with dK/dt. da/dt_{end} was fit with the power law trend shown in Equation 15.

$$da/dt_{end} = 1.13E-06(dK/dt)^{0.896} \quad \text{Equation 15}$$

3.3.2 Fractography

High magnification micrographs from the fracture surfaces for all dK/dt in $-0.950V_{SCE}$ are shown in Figure 34. All micrographs were taken near the precrack to avoid the effects of bulk plasticity on the fracture surface. The K_I at which each micrograph is centered around is listed in Table 10.



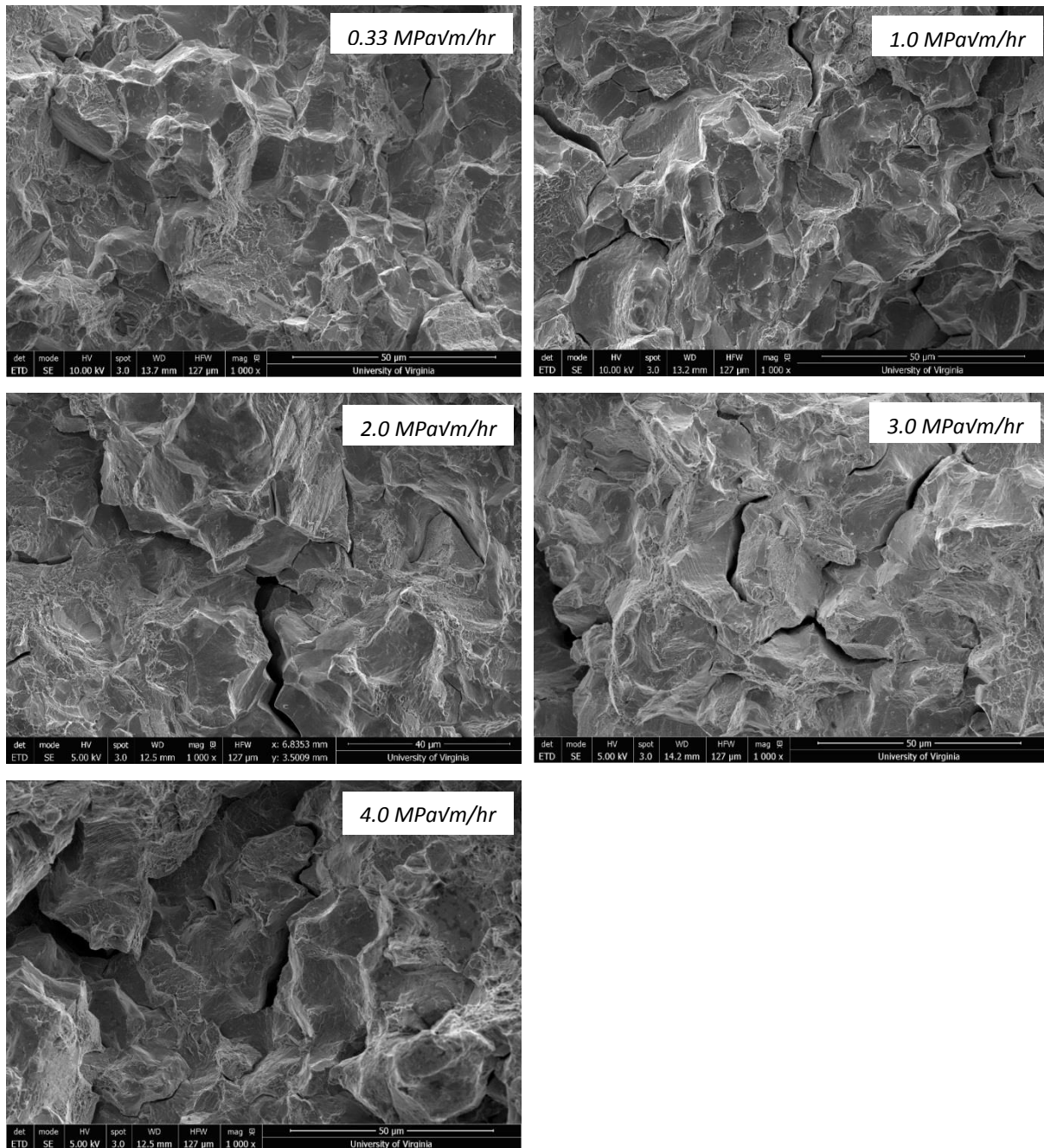


Figure 34: IG-SCC fracture surfaces of Monel K-500 in 0.6 M NaCl with $E_A = -0.950 V_{SCE}$, at 1000x.

Table 10: The K at which the micrographs in Figure 33 are centered around. Monel K-500, $-0.950V_{SCE}$

dK/dt (MPavm/hr)	K view (MPavm)
0.075	up to 27
0.1	45
0.15	37
0.2	43

0.33	44
1.0	43
2.0	42
3.0	44
4.0	45

All fracture surfaces in Figure 34 strongly display intergranular fracture with dimpling. This suggests that the IG failure is augmented by some degree of a ductile process; this is observed for all dK/dt . There is no strong observable change in the fracture morphology across the range of dK/dt examined for Monel K-500. The degree of dimpling is difficult to quantify; but, qualitatively, there is not a distinguishable change across the dK/dt . All dK/dt exhibit secondary cracking, out of plane cracking, but due to the reduction in IG-SCC fracture area associated with increasing dK/dt , there is insufficient area for comparison at high dK/dt . There is no quantitative or qualitative trend across the dK/dt in the fracture morphology.

3.3.3 Analysis of MP98t

3.3.3.1 dK/dt trends in MP98t

The K_{TH} was determined in the same manner as the Monel K-500 samples, but additional consideration was taken with da/dt_{end} . K_{end} spans 5 MPa \sqrt{m} for MP98t. In order to reduce scatter due to the range of K_{end} , a singular K of 55 MPa \sqrt{m} was used instead. K_{TH} and da/dt_{end} with respect to dK/dt are shown in Figures 35 and 36, respectively. The environmental fractography for each sample is displayed in Figure 37. The K_j at which each micrograph is centered around is listed in Table 11.

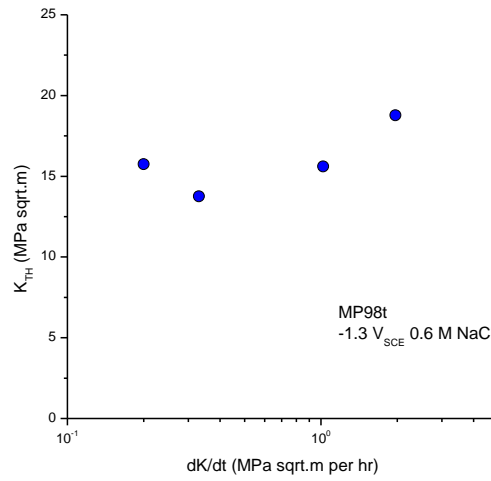


Figure 35: K_{TH} for MP98t for a range of dK/dt tested at -1.3 VSCE, 0.6M NaCl

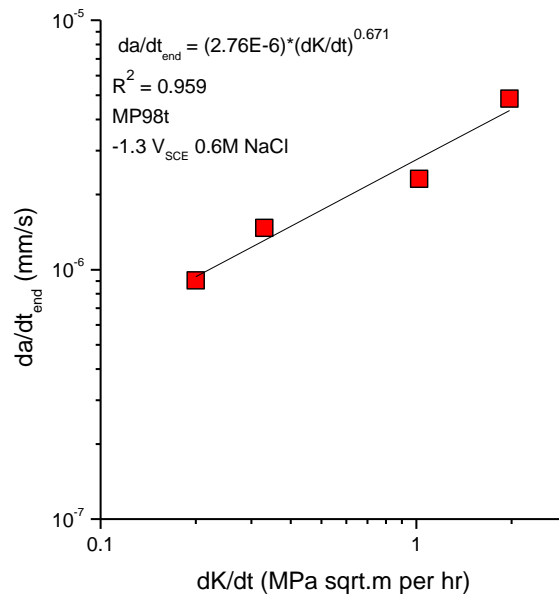


Figure 36: da/dt_{end} for MP98t for a range of dK/dt tested at -1.3 VSCE, 0.6M NaCl

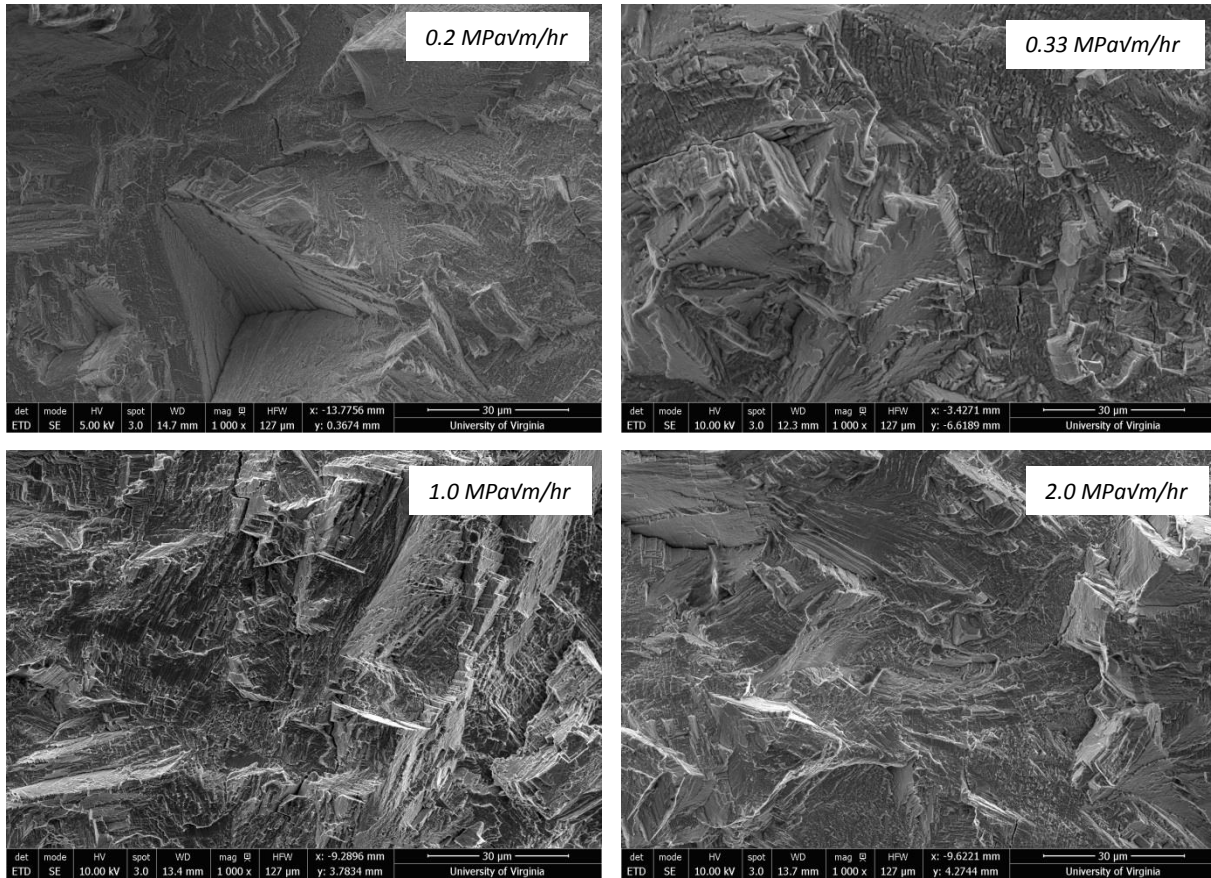


Figure 37: 1000x images of the Mode 1 environmental fracture of MP98t

Table 11: K each micrograph in Figure 36 is centered around, with corresponding dK/dt . MP98t $-1.30V_{SCE}$

dK/dt (MPa√m/hr)	K view (MPa√m)
0.2	30
0.33	34
1	57
2	42

MP98t does not demonstrate a strong dependence of K_{TH} on dK/dt , while the da/dt_{end} displays a power law dependence on dK/dt . MP98t displays only transgranular slip band cracking, the same fracture behavior as the precrack with no dimpling areas. HEDE can manifest as intergranular or transgranular fracture [43]. Aside from the full crack deflection, no secondary cracking is visible. The fracture morphology does not change across the dK/dt span.

3.3.4 Comparison between Monel K-500 and MP98t

MP98t exhibits loading rate dependencies very similar to Monel K-500. The materials display dK/dt independent K_{TH} that range between 10 and 25 MPa \sqrt{m} , as shown in Figure 38. The da/dt_{end} share a power law fit and fall closely within the same range, as shown in Figure 39. The most obvious difference in behavior is the fractography. Monel K-500 prominently displayed intergranular facets while MP98t is solely slip band-like transgranular fracture. Though the metric of these two materials fall closely in value, they were tested at different potentials. MP98t was exposed to a significantly more negative cathodic polarization Monel K-500. A strong trend has already been established between HEAC susceptibility and applied potential [4]. The K_{TH} would decrease and the da/dt_{end} would increase in accordance with the micromechanical decohesion models outlined in Equations 2 and 3. These data strongly suggest that MP98t is significantly less susceptible to HEAC due to cathodic polarization in aqueous chloride environments.

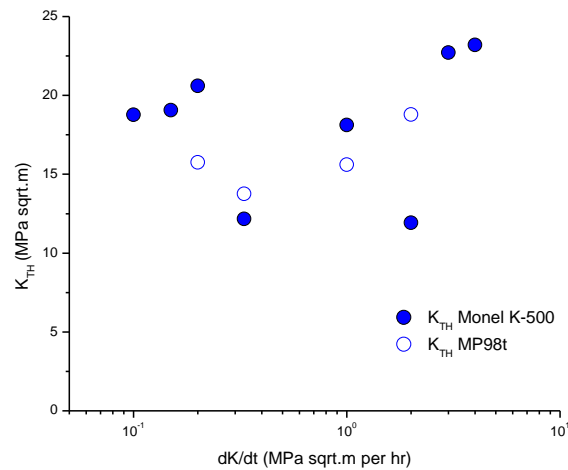


Figure 38: K_{TH} for the environmental data sets of Monel K-500 and MP98t

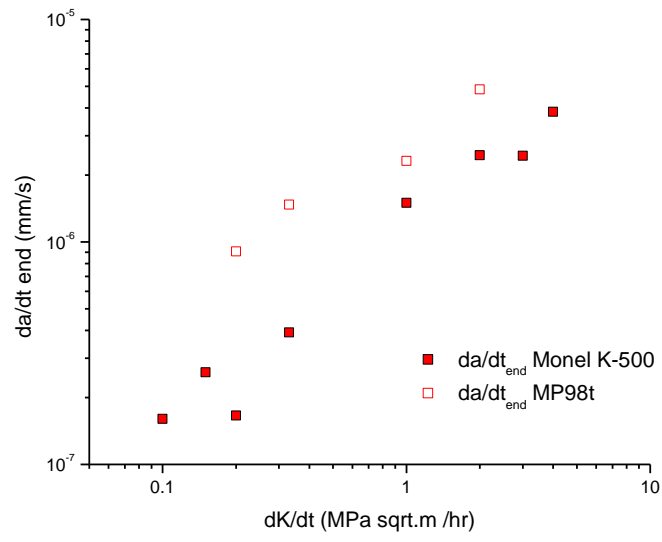


Figure 39: da/dt_{end} for the environmental data sets of Monel K-500 and MP98t

3.4 Task 3: Explore the mechanistic underpinnings that govern the effect of loading rate on the IG-SCC behavior of each alloy

This analysis aims to understand the observed influence of dK/dt on the da/dt and K_{TH} parameters in the context of the prevailing mechanistic interpretations in the H-embrittlement field. The mechanisms of HEAC are controversial, with Hydrogen Enhanced Decohesion (HEDE) and Hydrogen Enhanced Localized Plasticity (HELP) being most widely accepted. Fracture due to HEDE in Ni-based alloys is caused by grain boundary decohesion due to a reduction in the intrinsic grain boundary toughness caused by H; the magnitude of this effect will increase with increasing H-concentration [5]. By contrast, the HELP mechanism proposes that H decreases the dislocation-dislocation interaction energy thus enables a higher dislocation density in the fracture process zone [5], [76]. A consensus is emerging around a combined HELP-HEDE mechanism, where elevated localized strain hardening is enabled at the crack tip via HELP, this process conditions the local grain boundary environment to augment the H-induced reduction in the grain boundary toughness [77]. In this paradigm the final failure mechanism is attributed to decohesion [4], [58].

In the context of these mechanisms, the experimental dK/dt can influence the HEAC susceptibility of a material by affecting the H-uptake process at the crack tip, the kinetics of H diffusion in the process zone, and time-dependent H-dislocation interactions [4]. Such considerations have been applied to understand the loading rate sensitivity HEAC in other alloys (Al 2024, Ti-6Al-4V, and β -Ti [36], [41]), these prior efforts will be leveraged to inform the current analysis. Monel K-500 and MP98t share similar trends for da/dt and K_{TH} with dK/dt . Due to the abundance of accessible prior work on Monel K-500, the analysis will be focused on this material, but the same conclusions are expected to apply for MP98t. The data in Task 2 suggest two critical questions which need to be addressed: (1) What is the mechanistic cause for the observed increase in da/dt with increasing dK/dt ? and (2) Why is a similar systematic loading rate dependence not observed for the K_{TH} data in Figure 32?

3.4.1 Loading Rate dependence of da/dt

3.4.1.1 Diffusion Limitation

Prior work on Monel K-500 has established good agreement between the decohesion based micromechanical models by Gangloff and experimental data [4]. The model developed to describe da/dt_{II} is restated from Equation 3 [55], [57]. The variables are defined in the Introduction.

$$\left(\frac{da}{dt}\right)_{II} = \frac{4D_H}{x_{crit}} \left\{ \text{erf}^{-1} \left(1 - \frac{C_{H\sigma-crit}}{C_{H\sigma}} \right) \right\}^2 \quad \text{Equation 3 (restated)}$$

The da/dt_{end} recorded in this work is not an exact equivalent to diffusion limited da/dt_{II} because K_I independent SCC growth was not achieved. However, da/dt_{end} should still display the same trend behavior as da/dt_{II} because the values for da/dt_{end} were determined within a constant span of K_I for all tests. Critically, the K independent da/dt_{II} in the context of the diffusion limited micro-mechanical modeling paradigm assumes that the maximum rate of crack advance is rate limited rate at which H can diffusion over some critical distance into the crack tip process zone [55], [57], [78]. Specifically, H must be able to diffuse to the fracture process zone to be effective in HEDE, thus da/dt_{II} is a function of H lattice diffusion which has a time constraint. As such, is reasonable that da/dt_{II} would potentially be dependent on dK/dt if the loading rate is sufficiently rapid relative to the diffusion rate such that H cannot fully diffuse to x_{crit} . In other words, if the dK/dt outpaces the H diffusion, the HEDE mechanism will decline and da/dt_{II} will decrease with increasing dK/dt . This diffusion limited mechanism is proposed to be responsible for the retardation of EAC at high dK/dt loading rates [30], [36], [41], [79]. Clearly, the current data show the opposite trend of increasing da/dt_{end} with increasing dK/dt (0.1 to 4 MPa√m) for Monel K-500, which suggests that at these loading rates the diffusion kinetics are sufficiently rapid to not be limiting the EAC. As such there must be an alternative mechanism causing the increased da/dt over the dK/dt range examined.

3.4.1.2 Defecting of a Crack Tip Protective Film

Critically, HEAC requires the generation of H at the crack tip. Protective oxide layers at the crack tip can prevent the absorption of atomic H and prevent the detrimental effects of HEAC [61]. The stability of the crack tip protective film can be either electrochemically or mechanically

compromised; the mechanical rupture of this film would be caused by the crack tip strain rate due to dynamic loading of the crack. Once the film is damaged, H can be adsorbed then absorbed and diffuse into the material process zone. The extent of rupture and the regeneration rate of the film in the crack tip environment influences the concentration of H that is absorbed. The crack tip strain rate, $\dot{\epsilon}_{CT}$, is a function of dK/dt , has been shown to directly affect the HEAC susceptibility by destabilizing the film at high $\dot{\epsilon}_{CT}$. While the exact form of the equation is controversial, the crack tip strain rate is known to be a function of the K-value, dK/dt , da/dt and relevant material properties (yield strength, elastic modulus, and Poisson's ratio) [80], [81]. This protective film rupture mechanism is hypothesized to govern the observed increase in da/dt_{II} with increasing dK/dt in the Ti-6Al-4V alloy loaded in a chloride electrolyte [63]. Materials whose susceptibility is governed by this mechanism will exhibit a strong dK/dt dependence that will begin when the crack tip strain rate is sufficient to first rupture the film. This dK/dt dependence will end when either (1) the crack tip strain rate is sufficiently fast relative to the repassivation kinetics to maintain constant solution contact with the base material or (2) sufficiently high dK/dt such that the HEAC process becomes diffusion limited.

While this mechanism is logical in other alloy system and environment combinations, it requires an electrochemically stable protective film in the anticipated crack tip environment. A simplified Pourbaix diagram illustrates the bulk composition for this lot of Monel K-500 in interaction with a 0.6M NaCl environment in Figure 40. At $-0.950V_{SCE}$ in the bulk pH range is from 5 to 6.5 (but a more basic pH is expected in the crack tip [40]) no stable film occurs. As such, it is clear that the dependence of da/dt_{end} on dK/dt is not controlled by the film destabilization/rupture mechanism.

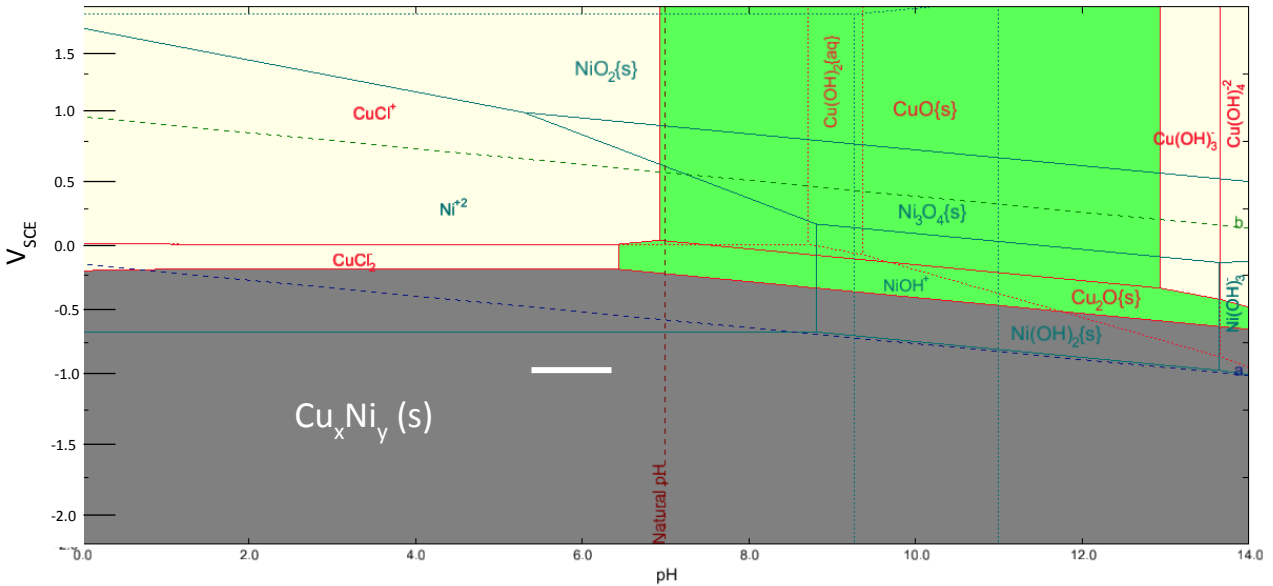


Figure 40: Representative Pourbaix diagram for Monel K-500 based on its two main components, Ni and Cu. OLI generated

3.4.1.3 Concurrent Plasticity and H Uptake

Critical research investigating HE of low alloy pressure vessel steels in H-gas environments offers a mechanistic paradigm in which to analyze the observed dependence of da/dt_{end} on the dK/dt [82]. Specifically, the work by Nibur et al. built on the HELP mechanism that contends that H will lower the dislocation-dislocation interaction energy, thus increasing localized dislocation mobility and enabling an enhancement of the plastic damage evolution for a given applied loading state [82]. Using a variety of experimental set-ups, this work demonstrated that concurrent loading (thus plasticity evolution) and H₂ environmental exposure, caused a drastic increase in the susceptibility to the HE phenomenon. This behavior suggests that when the mechanical loading and H-uptake occur independently the plastic damage state that evolves is not influenced by the effects of H. For example, in a sample that is pre-strained then exposed to an H-producing environment, the plastic damage was already set without the contribution of the HELP mechanism and thus the subsequent introduction of H was not observed to enhance the susceptibility. Critically, such a change in dislocation damage structure could impact the failure process through (1) the coupled HELP-HEDE mechanism where the enhanced dislocation structure results in increased local hardening, thus higher levels of local stress that promotes HEDE, or (2) the plasticity-related hydrogen induced cracking (PRHIC) phenomenon where the

crack advance is governed by the exceedance of a critical value of crack tip plastic strain [82], [83].

The demonstrated importance of the concurrent loading and H-uptake reasonably explains the observed differences between the RSL approach and the constant dK/dt (>0 MPa $\sqrt{m/hr}$) loading. Specifically, in the RSL approach the plasticity is induced during the rapid step increases in the load (thus K) where the loading rate may be too rapid for H contribution. Since the dislocation structure evolved during the step increase it was not enhanced by HELP.

The subsequent environmental exposure during the load-hold does not enable the full detrimental influence of the HELP process, and thus demonstrates a lower susceptibility compared to the concurrent loading of a constant dK/dt test. This is consistent with observed behavior by Dietzel for 7xxx-series Al and ASTM D1141 steels [55].

While the concurrent loading hypothesis reasonably explains the difference between RSL and the constant dK/dt (>0 MPa $\sqrt{m/hr}$) loading, it does not capture why increasing dK/dt should result in faster da/dt . This behavior can be rationalized in the context of the failure criteria associated with either the PRHIC or the coupled HELP-HEDE mechanism. For the PRHIC mechanism crack extension will occur when the equivalent plastic shear strain exceeds some critical value [82]. For a fixed K , the size of the relevant local plastic damage parameters will be constant regardless of dK/dt . From a bulk perspective this parameter could be defined as the plastic zone size. However, in the context of the proposed micro-mechanical strain based fracture criteria, the relevant metric is proposed to be the equivalent plastic shear strain proximate to the tip of a propagating Mode I crack [80], [82], [84]. For each dK/dt it is reasonable to assume that there will be a constant crack tip H concentration since a constant crack tip chemistry is expected, there is no influence of a passive film, and the loading rate is not causing diffusion limitation. As such, in the context of the PRHIC failure criteria, for a given time increment, a larger equivalent plastic strain would be accomplished by faster dK/dt . In other words, the critical crack tip plastic strain criteria would be satisfied faster and a higher da/dt would be expected. Similarly if the HELP-HEDE mechanism is controlling, the faster dK/dt would enable faster development of the work-hardened structure thus faster enhancement of the crack tip stresses that drive decohesion leading to increased da/dt . Both mechanisms, PRHIC and HELP-

HEDE, are reasonable. While definitive determination of the controlling mechanism is outside of the scope of the current study these data strongly suggest that the rate of plastic damage evolution at the crack tip is critical to dK/dt dependence of the HEAC behavior.

3.4.2 Effects on K_{TH}

Contrary to the trends in da/dt , the stress intensity K_{TH} of Monel K-500 in $-0.950 V_{SCE}$ $0.6M$ NaCl does not show a strong dependence on dK/dt ; specifically, the K_{TH} ranges from 11.9 to 23.2 MPa \sqrt{m} with no systematic dependence on dK/dt . As established above no effect of crack tip strain rate on a crack tip film is expected, furthermore for the loading rates examined, the K_{TH} is not expected to be diffusion limited.

The critical distinction between the da/dt dependence and the K_{TH} independence on loading rate can be again traced to the failure criteria for crack extension. Specifically, crack extension will occur over a distance where a critical combination of H concentration and local stress (or strain in the PRHIC paradigm) has been exceeded. For the da/dt behavior, the local stress (or strain) has exceeded this threshold, so incremental subsequent progression of crack extension is reasonably dependent on the rate at which the load is applied (thus the rate at which the plastic damage at the crack tip evolves). However, the K_{TH} value is fundamentally different in that it reflects the point at which the crack tip conditions exceed some critical value of H concentration and stress (or strain), rather than the further progression of a moving crack. It was previously demonstrated that for a constant K value the magnitude of the crack tip stresses and strains are not dependent on the dK/dt . As such, since these critical values have yet to be satisfied, it is logical that there will be no dK/dt dependence on the K_{TH} parameter.

Prior work on Monel K-500 HEAC susceptibility with environmental H concentration at a single dK/dt showed that the experimental K_{TH} is in good agreement with the decohesion based micromechanical model proposed by Gerberich (Equation 2) [4] [52], [55], [56]). This model can be used to further illustrate the hypothesis above.

$$K_{TH} = \frac{1}{\beta'} \exp \frac{(k_{IG} - \alpha C_H \sigma)^2}{\alpha'' \sigma_{YS}} \quad \text{Equation 2, restated}$$

In this model the β' and α'' parameters are from a dislocation shielding based model of crack tip stress, which are proposed to be independent of dK/dt (so long as there is a constant H-concentration). The k_{IG} is the intrinsic toughness of the boundary, and $\alpha_{CH\sigma}$ represents the degree to which this toughness is degraded by the local H concentration. Critically none of these terms would be expected to be dependent on the loading rate; this reinforces proposal that the K_{TH} will only occur once a fixed combination of crack tip stress (or strain in different model) and H-concentration for decohesion is reached.

4. Conclusions

Ni-based superalloys are have a known susceptibility to hydrogen environmentally assisted cracking (HEAC) in cathodically polarized aqueous salt solutions. Understanding the controlling mechanisms of HEAC in addition to developing accurate predictive models are crucial to the structural management of these material systems. Historic testing techniques such as Rising Step Load and Slow Strain Rate Tests do not adequately replicate the service setting and are prone to non-conservative behavior due to comparatively slow predicted crack growth. This work uses Linear Elastic Fracture Mechanics (LEFM) based testing to analyze the stress intensity rate (dK/dt) dependence of HEAC behavior for Monel K-500 and MP98t in cathodically polarized solutions. The following conclusions from each task were established:

Task 1: Consider a range of dK/dt and identify and address the challenges associated with data collection techniques to quantify the stress corrosion cracking (SCC) resistance using LEFM based techniques

- dcPD Characterization Challenges:
 - During slow rising dK/dt fracture mechanics testing, Monel K-500 demonstrated large errors between the dcPD calculated crack length and the IG-SCC crack length on the fracture surface for tests that were ended at high K.
 - Testing of Monel K-500 in inert environments showed changes in the electrical resistance behavior, observed via the dcPD system. These changes were dependent on the bulk ligament plastic behavior. Changes in slope of the apparent da/dt correlated well with the proportional limit and the yield stress, which suggests that they are not due to intrinsic changes in cracking behavior, but due to artifacts associated with changes in resistivity.
 - Inert tests that were ended at $K >$ yield stress showed a region of transgranular ductile tearing, identical to the final failure morphology, that had not been previously documented. This behavior was not observed when testing was halted prior to the yield strength.
 - The dcPD signal observed during the inert tests is created by localized crack tip plasticity, bulk ligament plasticity, and ductile tearing. These phenomena are not

completely distinguishable from true SCC in the calculated crack growth rate with the current experimental procedure. For the ductile tearing to be noticeable on the fracture surface, post-test fatigue with a transgranular fracture morphology is necessary to separate the dK/dt behavior from the final failure.

- Protocol Modifications
 - Truncating the environmental data at the proportional limit prevents eliminates the complicating effects of bulk scale plasticity and ductile tearing in the dcPD signal. This allows a rigorous characterization of crack extensions due to IG-SCC/EAC.
 - Sample geometry can be optimized to increase the K_{max} prior to bulk ligament plasticity.
 - The localized crack tip plasticity (the plastic zone) can be decoupled from the SCC data by subtracting the resolution limit from the experimental data.
 - The magnitude of the resolution limit was proven to scale linearly with dK/dt . Due to this, all resolution limits for a given material can be determined from a single inert test.
 - These protocols for maintaining data integrity were applied successfully to the MP98t data set.

Task 2: Quantify the effect of dK/dt on the standard LEFM metrics K_{TH} and da/dt_{end} for two different marine alloys at relevant electrochemical polarization(s)

- The quantitative metrics of MP98t and Monel K-500 fall closely to each other, but MP98t was exposed to higher levels of cathodic polarization than Monel K-500. These data illustrated that MP98t is far less susceptible to HEAC than Monel K-500 in cathodically polarized aqueous chloride environments.
- Monel K-500 displayed predominately intergranular fracture with small areas of dimpling. The fracture morphology did not noticeably change across the dK/dt span.
- MP98t displayed slip band transgranular fracture as its SCC failure mode. No ductile behavior was detected in the Mode I crack region.

- All MP98t samples tested at $-1.30V_{SCE}$ experienced out of plane cracking after a period of Mode I crack growth. The nature of the crack deflection is not discussed in this work.

Task 3: The mechanistic underpinnings that govern the effect of loading rate on the SCC behavior of each alloy were explored.

- Both Monel K-500 and MP98t displayed dK/dt independent K_{TH} while da/dt_{end} had a power law relationship with dK/dt .
- For the loading rates examined, the metrics were found to not be dependent on the behavior of a protective oxide film or any other diffusion limitation. These mechanisms can impede H uptake when stable, are not supported by Monel K-500 in the tested environment; preventing this from playing a role in Monel K-500's HEAC behavior.
- In these materials, the HEAC susceptibility is increased by concurrent strain and H uptake. The crack growth rate was over an order of magnitude larger for a $dK/dt = 0.33 \text{ MPa}\sqrt{\text{m}}$ test as compared to an RSL test of Monel K-500 in the same environmental conditions. This behavior supports a HELP-based mechanism in which H decreases the dislocation-dislocation interactions, allowing for increased plasticity and therefore hardening.
- For dK/dt that are not diffusion limited, where a sufficient H concentration exists at the fracture process zone, a threshold strain is required for crack advance. In this case, elevated dK/dt would cause elevated da/dt . A HELP-HEDE mechanisms could also achieve this same behavior through accelerated work-hardening and crack tip stress.
- These arguments do not influence K_{TH} because crack growth does not occur below this value. The only time dependence of K_{TH} in the decohesion based models comes through in diffusion limitation of H.

References

- [1] K. D. Efirid, "Failure of Monel Ni-Cu-Al alloy K-500 bolts in seawater," *Mater. Perform.*, vol. 24, no. 4, pp. 37–40, 1985.
- [2] L. H. Wolfe and M. W. Joosten, "Failures of nickel/copper bolts in subsea application," *SPE Prod. Eng.*, vol. 3, no. 3, pp. 382–386, 1988.
- [3] L. H. Wolfe, C. C. Burnette, and M. W. Joosten, "Hydrogen embrittlement of cathodically protected subsea bolting alloys," *Mater. Performance;(United States)*, vol. 32, no. 7, 1993.
- [4] R. P. Gangloff, H. M. Ha, J. T. Burns, and J. R. Scully, "Measurement and modeling of hydrogen environment-assisted cracking in monel K-500," *Metall. Mater. Trans. A Phys. Metall. Mater. Sci.*, vol. 45, no. 9, pp. 3814–3834, 2014.
- [5] S. Lynch, "Hydrogen embrittlement phenomena and mechanisms," in *Gaseous Hydrogen Embrittlement of Materials In Energy Technologies, Vol 1.*, R. Gangloff and B. Somerday, Eds. 2012, pp. 274–346.
- [6] Det Norske Veritas, "Cathodic protection design," 2005.
- [7] "QQ-N-286G. Federal specification for nickel-copper-aluminum alloy, wrought (UNS N05500)," 2000.
- [8] J. R. Davis, *Nickel, cobalt, and their alloys*. ASM international, 2000.
- [9] G. K. Dey and P. Mukhopadhyay, "Precipitation in the Ni-Cu-base alloy monel K-500," *Mater. Sci. Eng.*, vol. 84, pp. 177–189, 1986.
- [10] G. A. Scott, "Studbolting experience in the underwater environment of the North Sea," in *Offshore Technology Conference*, 1985.
- [11] R. E. Butler, "Hydrogen Embrittlement of High-Strength Alloys in Marine Environments," *Inst. Met.*, pp. 79–84, 1988.
- [12] C. A. Clark, S. Driscoll, and P. Guha, "Development of a new fastener alloy resistant to hydrogen embrittlement," *Br. Corros. J.*, vol. 27, no. 2, pp. 157–160, Jan. 1992.
- [13] J. R. Scully and M. G. Vassilaros, "The Hydrogen Embrittlement Susceptibility of Monel Alloy K-500," in *Electrochem. Soc. Fall 1983 Meeting, Washington, DC*, 1983.

- [14] R. D. Bayles, T. Lemieux, F. Martin, D. Lysogorski, T. Newbauer, W. Hyland, B. A. Green, E. Hogan, T. Longazel, and P. Stencel, "Monel K-500 Hydrogen Embrittlement," *Nav. Surf. Treat. Cent. MR2010 Proc. Present.*, 2010.
- [15] R. H. Jones and S. M. Bruemmer, "Environment-Induced Cracking in Metals," *Environ. Crack. Met.*, pp. 287–310, 1990.
- [16] M. H. Kamdar, "Embrittlement of Nickel by Gaseous Hydrogen," in *Hydrogen in Metals, Proceedings of the 2nd International Conference*, 1977.
- [17] D. H. Lassila and H. K. Birnbaum, "Intergranular fracture of nickel: the effect of hydrogen-sulfur co-segregation," *Acta Metall.*, vol. 35, no. 7, pp. 1815–1822, Jul. 1987.
- [18] D. H. Lassila and H. K. Birnbaum, "The effect of diffusive segregation on the fracture of hydrogen charged nickel," *Acta Metall.*, vol. 36, no. 10, pp. 2821–2825, 1988.
- [19] R. Otsuka, T. Maruno, and H. Tsuji, "Correlation Between Hydrogen Embrittlement and Hydride Formation in Ni--Cu and Pd--Ag Alloys," in *International Congress on Metallic Corrosion*, 1984, vol. 2, pp. 270–277.
- [20] N. R. Moody, S. L. Robinson, and W. M. Garrison Jr, "Hydrogen effects on the properties and fracture modes of iron-based alloys," *Res Mech.*, vol. 30, no. 2, pp. 143–206, 1990.
- [21] D. M. Symons, "A comparison of internal hydrogen embrittlement and hydrogen environment embrittlement of X-750," *Eng. Fract. Mech.*, vol. 68, no. 6, pp. 751–771, 2001.
- [22] B. P. Focht, E. M. and L'Heureux, "Development of Modified Alloy MP159 Bar for 150 ksi Marine Grade Fasteners," West Bethesda, MD, 2002.
- [23] E. Focht, B. L'Heureux, and C. Roe, "Development of a Fastener Structural Element Test for Certifying Navy Fastener Materials," in *Structural Integrity of Fasteners Including the Effects of Environment and Stress Corrosion Cracking: 3rd Volume*, ASTM International, 2007.
- [24] "Standard Practice for Preparation and Use of Bent-Beam Stress-Corrosion Test Specimens." ASTM International, 2016.
- [25] "Standard Practice for Making and Using U-Bend Stress-Corrosion Test Specimens." ASTM International, 2016.

- [26] “Standard Practice for Slow Strain Rate Testing to Evaluate the Susceptibility of Metallic Materials to Environmentally Assisted Cracking.” ASTM International, 2013.
- [27] T. L. Anderson, *Fracture mechanics: fundamentals and applications*. CRC press, 2005.
- [28] “Standard Test Method for Determining Threshold Stress Intensity Factor for Environment-Assisted Cracking of Metallic Materials.” ASTM International, 2013.
- [29] “Standard Test Method for Measurement of Hydrogen Embrittlement Threshold in Steel by the Incremental Step Loading Technique.” ASTM International, 2012.
- [30] J. D. Landes and W. Dietzel, “An analysis of creep deformation parameters. Part 2: experimental study,” *Eng. Fract. Mech.*, vol. 71, no. 16, pp. 2463–2474, 2004.
- [31] G. L. Pioszak, “CHARACTERIZATION OF STRESS CORROSION CRACKING (SCC) IN ULTRA-HIGH STRENGTH STAINLESS STEEL.”
- [32] M. McMahon, P. Steiner, A. Lass, and J. Burns, “The Effect of Loading Orientation on the Stress Corrosion Cracking of Al-Mg Alloys,” *CORROSION*, 2017.
- [33] M. McMahon, P. Steiner, A. Lass, and J. Burns, “The Effect of Temper and Composition on the Stress Corrosion Cracking of Al-Mg Alloys,” *CORROSION*, 2016.
- [34] C. B. Crane and R. P. Gangloff, “Stress corrosion cracking of Al-Mg alloy 5083 sensitized at low temperature,” *Corrosion*, vol. 72, no. 2, pp. 221–241, 2015.
- [35] R. P. Gangloff and B. P. Somerday, *Gaseous Hydrogen Embrittlement of Materials in Energy Technologies: Mechanisms, Modelling and Future Developments*. Elsevier, 2012.
- [36] B. P. Somerday, L. M. Young, and R. P. Gangloff, “Crack tip mechanics effects on environment-assisted cracking of beta-titanium alloys in aqueous NaCl,” *Fatigue Fract. Eng. Mater. Struct.*, vol. 23, no. 1, pp. 39–58, 2000.
- [37] J. D. Dolph, “The Effect of Microstructure on the HEAC Behavior of Monel K-500,” University of Virginia, 2015.
- [38] Z. D. Harris, J. D. Dolph, G. L. Pioszak, B. C. Rincon Troconis, J. R. Scully, and J. T. Burns, “The Effect of Microstructural Variation on the Hydrogen Environment-Assisted Cracking of Monel K-500,” *Metall. Mater. Trans. A*, vol. 47, no. 7, pp. 3488–3510, 2016.
- [39] R. P. Gangloff, “Probabilistic Fracture Mechanics Simulation of Stress Corrosion Cracking Using Accelerated Laboratory Testing and Multi-Scale Modeling,” *Corrosion*, vol. 72, no.

- 7, pp. 862–880, 2016.
- [40] J.-H. Ai, H. M. Ha, R. P. Gangloff, and J. R. Scully, “Hydrogen diffusion and trapping in a precipitation-hardened nickel–copper–aluminum alloy Monel K-500 (UNS N05500),” *Acta Mater.*, vol. 61, no. 9, pp. 3186–3199, 2013.
- [41] W. Dietzel, “Fracture mechanics approach to stress corrosion cracking,” in *Anales de Mecánica de la Fractura*, 2001, vol. 18, pp. 1–7.
- [42] D. G. Westlake, “Generalized Model For Hydrogen Embrittlement,” *Trans ASM*, vol. 62, pp. 1000–1006, 1969.
- [43] S. P. Lynch, “Mechanisms of hydrogen assisted cracking—a review,” in *Hydrogen Effects on Material Behaviour and Corrosion Deformation Interactions*, 2003, pp. 449–466.
- [44] S. P. Lynch, “Environmentally assisted cracking: overview of evidence for an adsorption-induced localised-slip process,” *Acta Metall.*, vol. 36, no. 10, pp. 2639–2661, 1988.
- [45] S. P. Lynch, “Metallographic contributions to understanding mechanisms of environmentally assisted cracking,” *Metallography*, vol. 23, no. 2, pp. 147–171, 1989.
- [46] H. K. Birnbaum, “Mechanisms of hydrogen related fracture of metals,” in *Hydrogen effects on Material behavior*, 1989, pp. 639–658.
- [47] H. K. Birnbaum, I. M. Robertson, P. Sofronis, and D. Teter, “Mechanisms of hydrogen related fracture—a review,” in *Second International Conference on Corrosion-Deformation Interactions. CDI’96*, 1996, pp. 172–195.
- [48] C. D. Beachem, “A new model for hydrogen-assisted cracking (hydrogen ‘embrittlement’),” *Metall. Trans.*, vol. 3, no. 2, pp. 441–455, 1972.
- [49] H. K. Birnbaum and P. Sofronis, “Hydrogen-enhanced localized plasticity—a mechanism for hydrogen-related fracture,” *Mater. Sci. Eng. A*, vol. 176, no. 1–2, pp. 191–202, 1994.
- [50] H. K. Birnbaum, I. M. Robertson, and P. Sofronis, “Hydrogen effects on plasticity,” in *Multiscale Phenomena in Plasticity: From Experiments to Phenomenology, Modelling and Materials Engineering*, Springer, 2000, pp. 367–381.
- [51] R. A. Oriani, “A mechanistic theory of hydrogen embrittlement of steels,” *Berichte der Bunsengesellschaft für Phys. Chemie*, vol. 76, no. 8, pp. 848–857, 1972.
- [52] W. W. Gerberich and S. Chen, “Environment-induced cracking of metals, fundamental

- processes: micromechanics," *Environ. Crack. Met. Natl. Assoc. Corros. Eng. Houston, TX*, pp. 167–187, 1990.
- [53] W. W. Gerberich, P. G. Marsh, and J. W. Hoehn, "Hydrogen induced cracking mechanisms—are there critical experiments?," *Hydrog. Eff. Mater.*, pp. 539–554, 1996.
- [54] C. J. McMahon, "Hydrogen-induced intergranular fracture of steels," *Eng. Fract. Mech.*, vol. 68, no. 6, pp. 773–788, 2001.
- [55] Y. Lee and R. P. Gangloff, "Measurement and Modeling of Hydrogen Environment--Assisted Cracking of Ultra-High-Strength Steel," *Metall. Mater. Trans. A*, vol. 38, no. 13, pp. 2174–2190, 2007.
- [56] R. P. Gangloff, "Science-based prognosis to manage structural alloy performance in hydrogen," *Hydrog. Eff. Mater.*, pp. 1–21, 2009.
- [57] M. M. Hall Jr and D. M. Symons, "Hydrogen assisted creep fracture model for low potential stress corrosion cracking of Ni-Cr-Fe Alloys," in *Proc. Staehle Symp. on Chemistry and Electrochemistry of Corrosion and SCC*, ed. RH Jones (Warrendale, PA: The Minerals, Metals, and Materials Society [TMS], 2001), 2001, p. 447.
- [58] M. L. Martin, B. P. Somerday, R. O. Ritchie, P. Sofronis, and I. M. Robertson, "Hydrogen-induced intergranular failure in nickel revisited," *Acta Mater.*, vol. 60, no. 6, pp. 2739–2745, 2012.
- [59] R. P. Gangloff, "Comprehensive Structural Integrity, Vol. I. Milne, RO Ritchie, and B. Karihaloo." Pergamon, San Diego, 2003.
- [60] J. R. Scully and P. J. Moran, "Influence of strain on the environmental hydrogen-assisted cracking of a high-strength steel in sodium chloride solution," *Corrosion*, vol. 44, no. 3, pp. 176–185, 1988.
- [61] D. G. Kolman and J. R. Scully, "Continuum mechanics characterization of plastic deformation-induced oxide film rupture," *Philos. Mag. A*, vol. 79, no. 10, pp. 2313–2338, 1999.
- [62] J. Toribio, "The role of crack tip strain rate in hydrogen assisted cracking," *Corros. Sci.*, vol. 39, no. 9, pp. 1687–1697, 1997.
- [63] E. Richey and R. P. Gangloff, "Strain Rate Dependent Environment Assisted Cracking of

- α/β -Ti Alloys in Chloride Solution,” in *Environmentally Assisted Cracking: Predictive Methods for Risk Assessment and Evaluation of Materials, Equipment, and Structures*, ASTM International, 2000.
- [64] “Standard Test Methods for Determining Average Grain Size.” ASTM International, 2013.
- [65] H. Tada, P. C. Paris, and G. R. Irwin, “The Stress Analysis of Cracks Handbook. The American Society of Mechanical Engineers,” *New York*, 2000.
- [66] H. H. Johnson, “Calibrating the electric potential method for studying slow crack growth (Calibration of electric potential technique to study slow or steady crack growth in high strength materials),” *Mater. Res. Stand.*, vol. 5, pp. 442–445, 1965.
- [67] D. Hellmann and K. H. Schwalbe, “Application of the electrical potential method to crack length measurements using Johnson’s formula,” *J. Test. Eval.*, vol. 9, no. 3, pp. 218–220, 1981.
- [68] R. P. Gangloff, D. C. Slavik, R. S. Piascik, and R. H. Van Stone, “Direct current electrical potential measurement of the growth of small cracks,” in *Small-Crack Test Methods*, ASTM International, 1992.
- [69] C. Ragazzo, R. Hertzberg, and R. Jaccard, “A Method for Generating Fatigue Marker Bands Using a Constant K_{max} Test Procedure BT - A Method for Generating Fatigue Marker Bands Using a Constant K_{max} Test Procedure,” 1995.
- [70] V. Kumar, M. D. German, and C. F. Shih, “Engineering approach for elastic-plastic fracture analysis,” General Electric Co., Schenectady, NY (USA). Corporate Research and Development Dept., 1981.
- [71] “Standard Test Method for Measurement of Fatigue Crack Growth Rates.” ASTM International, 2013.
- [72] M. Zehetbauer and V. Seumer, “Cold work hardening in stages IV and V of F.C.C. metals— I. Experiments and interpretation,” *Acta Metall. Mater.*, vol. 41, no. 2, pp. 577–588, 1993.
- [73] T. Broom, “Lattice defects and the electrical resistivity of metals,” *Adv. Phys.*, vol. 3, no. 9, pp. 26–83, Jan. 1954.
- [74] N. E. Dowling, *Mechanical behavior of materials*. Pearson, 2012.

- [75] G. C. Kuczynski, "Effect of Elastic Strain on the Electrical Resistance of Metals," *Phys. Rev.*, vol. 94, no. 1, pp. 61–64, Apr. 1954.
- [76] I. M. Robertson, P. Sofronis, A. Nagao, M. L. Martin, S. Wang, D. W. Gross, and K. E. Nygren, "Hydrogen embrittlement understood," *Metall. Mater. Trans. B*, vol. 46, no. 3, pp. 1085–1103, 2015.
- [77] Y. Ro, S. R. Agnew, and R. P. Gangloff, "Effect of Environment on Fatigue Crack Wake Dislocation Structure in Al-Cu-Mg," *Metall. Mater. Trans. A*, vol. 43, no. 7, pp. 2275–2292, 2012.
- [78] R. P. Gangloff, *Hydrogen Effects on Material Behavior and Corrosion Deformation Interactions*. 2003.
- [79] B. P. Somerday and R. P. Gangloff, "Effect of strength on environment-assisted cracking of Ti-8V-6Cr-4Mo-4Zr-3Al in aqueous NaCl: Part II: Crack tip strain rate," *Mater. Sci. Eng. A*, vol. 254, no. 1, pp. 179–188, 1998.
- [80] J. R. Rice, W. J. Drugan, and T.-L. Sham, "Elastic-plastic analysis of growing cracks," in *Fracture Mechanics*, ASTM International, 1980.
- [81] J. R. Rice and E. P. Sorensen, "Continuing crack-tip deformation and fracture for plane-strain crack growth in elastic-plastic solids," *J. Mech. Phys. Solids*, vol. 26, no. 3, pp. 163–186, 1978.
- [82] K. A. Nibur, B. P. Somerday, C. S. Marchi, J. W. Foulk, M. Dadfarnia, and P. Sofronis, "The Relationship Between Crack-Tip Strain and Subcritical Cracking Thresholds for Steels in High-Pressure Hydrogen Gas," *Metall. Mater. Trans. A*, vol. 44, no. 1, pp. 248–269, 2013.
- [83] Y. Takeda and C. J. McMahon, "Strain controlled vs stress controlled hydrogen induced fracture in a quenched and tempered steel," *Metall. Mater. Trans. A*, vol. 12, no. 7, pp. 1255–1266, 1981.
- [84] W. J. Drugan, J. R. Rice, and T. L. Sham, "Asymptotic analysis of growing plane strain tensile cracks in elastic-ideally plastic solids," *J. Mech. Phys. Solids*, vol. 30, no. 6, pp. 447–473, 1982.